Title

Development of a Modular Positron Beamline for High Instantaneous Current Density Bursts

Author

Cecchini, Gabriel George

Publication Date

2021

UNIVERSITY OF CALIFORNIA
RIVERSIDE

Development of a Modular Positron Beamline for High Instantaneous Current Density Bursts

A Dissertation submitted in partial satisfaction
of the requirements for the degree of

Doctor of Philosophy

in

Physics

by

Gabriel George Cecchini

September 2021

Dissertation Committee:

Dr. Allen P. Mills Jr., Chairperson
Dr. Jory Yarmoff
Dr. Boerge Hemmerling

The Dissertation of Gabriel George Cecchini is approved:

Committee Chairperson

University of California, Riverside

Acknowledgments

Throughout my graduate school experience, I have received a great deal of support and assistance from the NSF, and from UCR.

I am grateful to my advisor for macro managing me and trusting me to do my best. I would like to acknowledge Dr. Rod Greaves for many years of collaboration.

In addition, I would like thank my good friends Adric Jones, Ethan Roeder, and Thomas Dugger for stimulating discussions as well as happy distractions outside of my research.

I dedicate this to my late grandmother for her constant faith and support

And to my parents and friends for all the support.

ABSTRACT OF THE DISSERTATION

Development of a Modular Positron Beamline for High Instantaneous Current Density Bursts

by

Gabriel George Cecchini

Doctor of Philosophy, Graduate Program in Physics
University of California, Riverside, September 2021
Dr. Allen P. Mills Jr., Chairperson

A brief history of positron sciences in atomic, molecular, and optical, and condensed matter physics is presented. A short description of a pulsed positron beam-line using a 50 mCi ^{22}Na source as the positron supply follows. Three different positron/positronium (Ps) beam manipulation devices are described in detail: a magnetic swtich-yard that effectively guides positron pulses to one of three experiments on demand; a high voltage buncher-accelerator that extracts positrons from a magnetic field with reduced effects from non-adiabatic impulses upon the low field transition; and the world's first achromatic electrostatic mirror for reflecting and focusing Rydberg atoms. A detector for positronium temperature measurements by two-photon angular correlation annihilation radiation, and a resistive-anode based position sensitive Rydberg atom detector, are discussed at length with experimental data and results shown. A high performance positron high vacuum accumulator is described along with a procedure necessary to retain "strong-drive" coupling of the positron plasma with a rotating electric dipole above 100 MHz, $\sim$ 12.5% of the Brillouin limit. The final chapter describes our achievement of a new record magnetic field free peak areal positron density of $\sim 1.5\times10^{11}$ cm^{-2} and an instantaneous current density of ~ 6.25 A cm^{-2}, satisfactory conditions for probing Ps-Ps interactions and the production of a highly spin-polarized positron beam useful for creating a Ps Bose-Einstein Condensate.

Contents

List of Figures

List of Tables

Chapter 1

Introduction and Background

1.1 History of Positron Physics

1.1.1 Genesis

The study of anti-matter, namely the positron, started nearly 100 years ago when in 1928 Dirac formulated a quantum theory incorporating Einstein's special relativity to explain the motion of electrons. The quantum theory of the electron was received by the journal Proceedings of the Royal Society A on 2 January 1928 and it won Dirac the Nobel prize in physics in 1933. Dirac's equation led to a $E^2 = m^2c^4 + p^2c^2$ solution, meaning that an electron-like particle could have negative energy, but the correct interpretation is that for every particle there exists a corresponding anti-particle, identical to its regular matter counterpart, but with opposite charge.

It would be four more years until Carl Anderson published evidence of the observation of a positron [4] displaying a photograph of a particle's trail through a cloud chamber in a magnetic field with a 6 mm lead plate separating the chamber into two parts. The change in the curvature of the trail after passing through the lead plate indicated the direction of the particle's motion, thus showing that the particle was equivalent to a positively charged electron, the positron. The production of positron emitting sources by Curie and Joliot by alpha bombardment of Boron to yield Nitrogen-13, a positron emitter [97], and the discovery that Nitrogen-13 could also be produced by the bombardment of Carbon with heavy hydrogen [182] led to a boom in the study positron physics. The prediction of the existence of the hydrogen-like atom positronium was made in 1934 by Stjepan Mohorovičić [145] and calculations by J. A. Wheeler in 1946 proved that exotic polyelectrons consisting of one positron and one or two electrons were stable against dissociation [180]. The positronium atom was first observed by Martin Deutsch in 1951 [60].

1.1.2 Basis of positron science

Semi-relativistic beta-decay positrons with end-point energies of about half an MeV very rapidly ($\sim$ 10 ps) slow to near thermal energies in solid materials due to the large Coulomb scattering rate with the atomic electrons. On the other hand the positron decay rate into two 511 keV photons via annihilation with the atomic electrons is much slower ($\gtrsim$100 ps) due to the far off-shell intermediate state in the annihilation process [65] This fact means that positrons will mostly stop before annihilating in a sample of ordinary matter. The principle mode of annihilation conserves angular momentum, with a deviation from co-linearity within 15 minutes of angle [13]. Using a gamma ray crystal diffractometer Dumond *et.al.* [67] discovered that the 511 keV line was broadened beyond what could be attributed to the instrumentation, thus laying the foundation for "Doppler Broadening Spectroscopy"

(DBS) as a way to measure the momentum distribution of electrons in condensed matter samples. A related measurement of the deviation from co-linearity of annihilation photon pairs [58] showed that this could also be used as a probe of electron momentum distributions. This was the beginning of the modern method for measuring the Angular Correlation of Annihilation Radiation (ACAR).

1.2 Development of Positron Science

1.2.1 Positron atomic physics

The proof of the existence of positronium (Ps) was obtained by Martin Deutsch in an experiment [60] in which low energy gamma rays expected from triplet Ps annihilating in pure N_2 gas were diminished or "quenched" when 5 percent NO gas was added. The interpretation was that during a collision of Ps with an NO molecule the unpaired electron on the NO can sometimes exchange spins with the electron on the Ps atom, causing the Ps to change from the long-lived triplet state to the short lived singlet state. The existence of Ps was confirmed by the observation of its characteristic three-quantum annihilation [61]. Triplet Ps (ortho-positronium, o-Ps) can also be quenched by a magnetic field aligned with the quantization axis. This mixes m=0 $^3S_1$ atoms with m=0 $^1S_0$ atoms owing to the quadratic Zeeman effect shown by Deutsch [63]. This effect is similar to that of the 2S state of Hydrogen in an electric field, as discovered by Lamb and Retherford in 1950 [115]. Deutsch finished his annus mirabilis [131] with the measurement of the Ps hyperfine interval [62]. Other exotic matter-antimatter compounds have since been created such as the positronium negative ion and the di-positronium molecule, observed by Mills [143], and Cassidy and Mills [40] respectively.

Owing to its purely leptonic nature, positronium is an ideal test of quantum electrodynamics (QED), including: (1) QED theoretical corrections calculated up to $\mathcal{O}(m\alpha^6)$ [148, 54, 53, 2, 183], and in the measurement of: (2) the hyperfine splitting of Ps in 1952 [62]; (3) the g-factor of the positron in 1966 [154]; (4) positronium Lyman-α radiation in 1974 [25]; (5) the $1^3S_1 - 2^3S_1$ positronium interval in 1984 [49]; (6) the o-Ps lifetime puzzle in 2003 [172]; and (7) the fine structure of n=2 Ps in 1975 [128] and 2020 [86].

1.2.2 Positrons condensed matter physics

The rapid positron thermalization rates in condensed matter, mediated at low energies by positron-phonon interactions, means that positron-electron annihilation gammas carry information that is dominated by the state of the annihilated electron. This fact allowed Stewart to make precision ACAR measurements of nearly all of the pure metals [163]. Compared to other experimental methods, such as x-ray scattering, neutron scattering, Compton scattering, de Haas-van Alphen measurements, spin-polarized photoemission, each of which has some advantages and some disadvantages, ACAR has its own niche, particularly in the measurement of spin-polarized electron Fermi surfaces in crystalline metals and in alloys [15].

Positron lifetime distribution measurements [12], have shown that positrons interact readily with lattice vacancies in metals, where they have lifetimes ~ 200 ps [94, 178]. Vacancy volumes and uniformity in a wide variety of porous and uniform materials can be measured using positron annihilation lifetime spectroscopy (PALS), and various scanning positron probes, with countless variations, such as Single-Shot Positron Annihilation Lifetime Spectroscopy (SSPALS) [29]. The positron microscope or scanning microprobe is still a possibility that has not lived up to its theoretical potential due to the lack of sufficiently strong and convenient positron beams.

Observation of positronium like states at the surface of crystals [133] was shown to also be sensitive to vacancies with some surface trapping [122]. Anisotropy of Angle-Resolved Positronium Emission Spectroscopy data of Chen *et. al.* [47] supports the conclusion that the recorded Ps emission spectra reflects that of the electron density of states at or very near the surface of cyrstals. The spin polarization of slow positron beams might be useful for spin and angle resolved spectroscopy of positronium emission of the electronic structure of surfaces such as TaAs.

Chapter 2

Pulsed Positron Beam-Line

2.1 Source Stage

The positron beam in the UCR laboratory is powered by a nominally 50 mCi sealed radioactive ^{22}Na source installed within a vacuum system on Nov. 14, 2019. With a half-life of 2.6 years, ^{22}Na is suitable for long term experiments. To reduce the radiation field near the source, the ^{22}Na and its vacuum system (see Fig. 2.1) are shielded inside a 40 cm diameter Al cylinder filled with Lead shot. In addition, the vacuum system incorporates several Elkonite ($W_{0.9}$ $Cu_{0.1}$ alloy) apertured cylindrical plugs to reduce the radiation that would otherwise leak out in critical locations. (see Fig. 2.2).

2.1.1 Magnetic transport of slow positrons

Positrons are emitted from the ^{22}Na source ($f(\beta^{+}) \sim 90\%$) centered between 2 electromagnets in a Helmholtz configuration. This configuration of positioning of two iden-

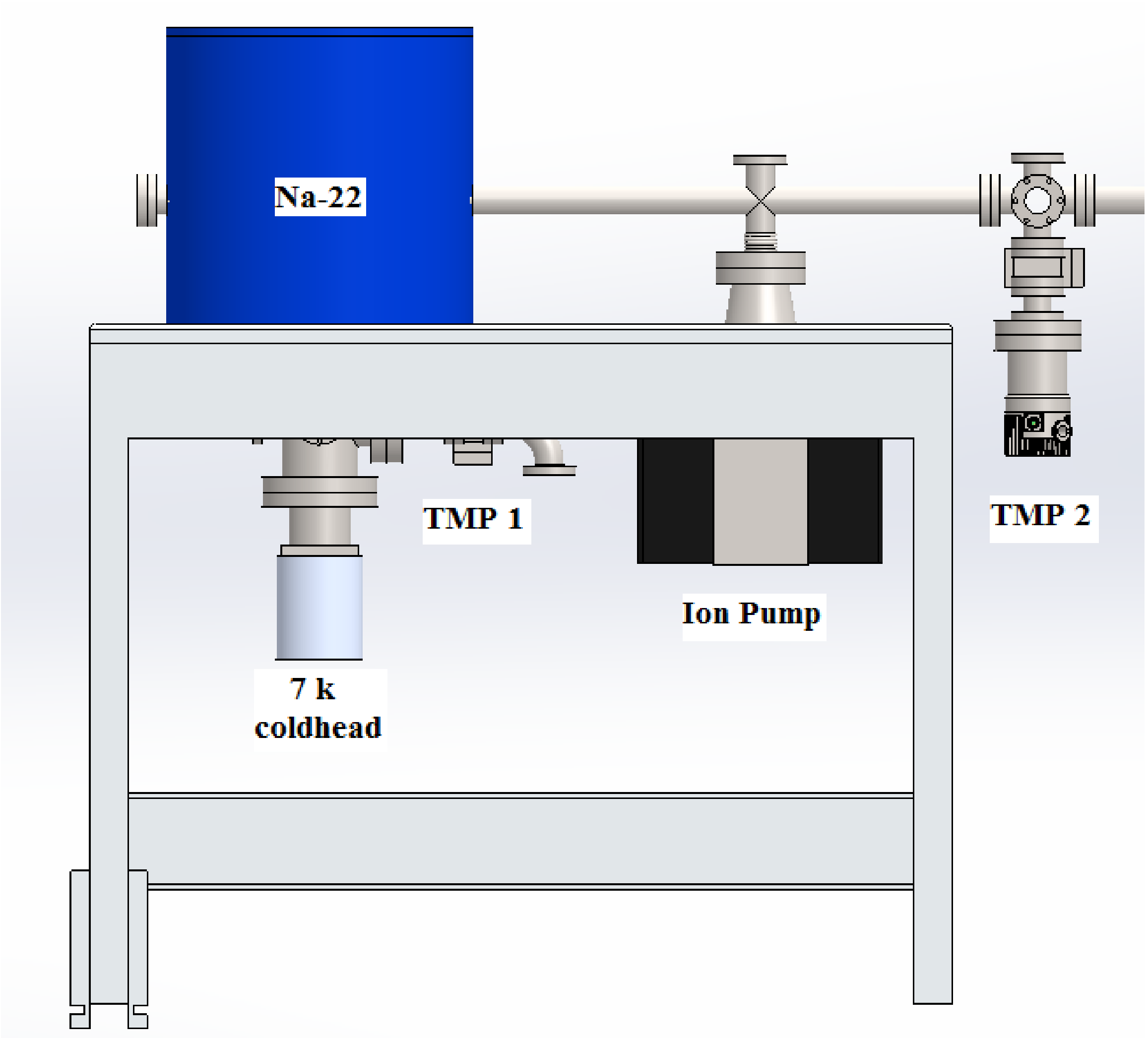

Figure 2.1: Source stage vacuum assembly.

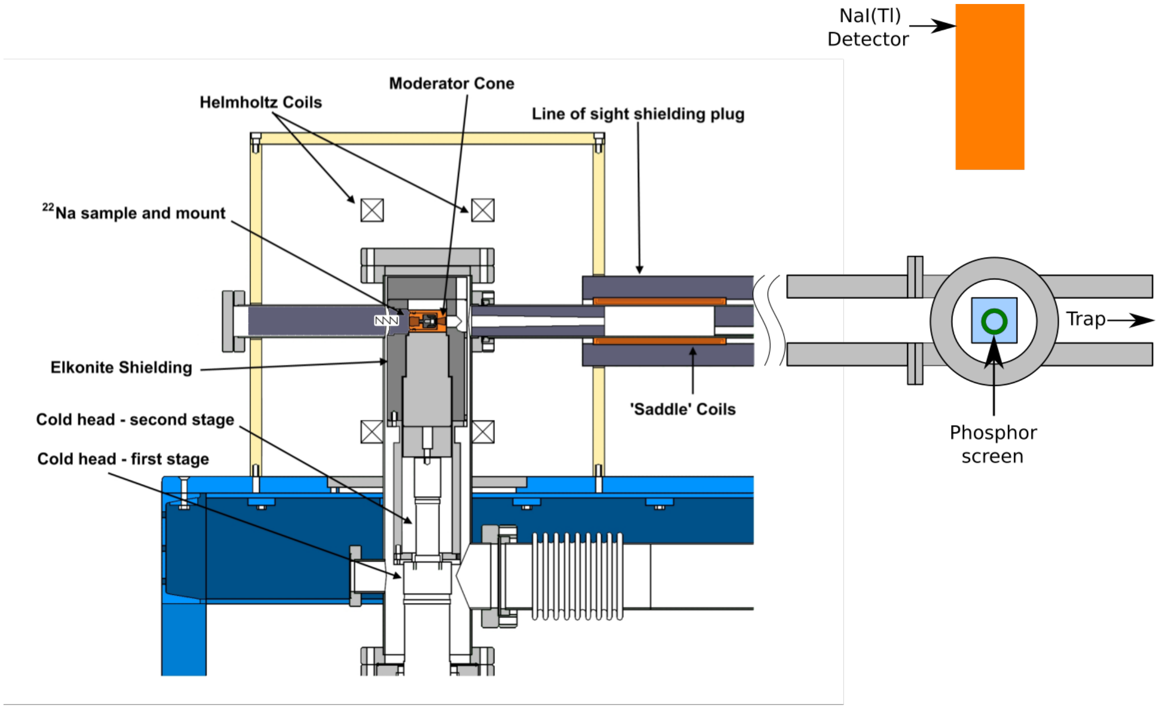

Figure 2.2: Source stage schematic with moderator count rate diagnostic.

tical concentric ring-like electromagnets powered with the same current 1 radius apart is widely used as the produced magnetic along the axis of the magnets varies by about 7% between the planes of the electromagnets and the second-derivative of the magnetic field at the center is zero. The slow positrons are field-locked as supported by the following. Starting from the Lorentz force, $\vec{F} = q(\vec{E} + \vec{v} \times \vec{B})$, and proceeding in the fluid limit, $\vec{j} = \sigma(\vec{E} + \vec{v} \times \vec{B})$ (Ohm's Law), one can make use of classical Gallilean transformation, $\vec{E'} = \vec{E} + \vec{v} \times \vec{B}$, as we will be using slow positrons. Using Ampere's Law, $\oint \vec{B} \cdot d\vec{l} = \mu_0 \int \int \vec{J} \cdot d\vec{S} = \mu_0 I_{\text{enclosed}} \implies \nabla \times \vec{B} = \mu_0 \vec{j}$, our fluid limit Ohm's law becomes $\nabla \times \vec{B} = \mu_0 \sigma(\vec{E} + \vec{v} \times \vec{B})$ and, upon taking the curl and applying the Maxwell-Faraday relation ($\vec{\nabla} \times \vec{E} = -\frac{\partial B}{\partial t}$), simplifies to $\partial_t \vec{B} = \nabla \times (\vec{v} \times \vec{B}) + \frac{\nabla^2 B}{\mu_0 \sigma}$. Assuming the current density (the positrons) moves through the vacuum unimpeded, or $\sigma \rightarrow \inf$, we arrive at Alfvén's frozen-in theorem, $\frac{d\Phi_B}{dt} = \int_S dA[\partial_t B - \nabla \times (\vec{v} \times \vec{B})] = 0$. Therefore, the magnetic flux through a surface moving along with a plasma (fluid) is conserved, or rather the plasma moves along the local field lines.

Magnetic fields are used to guide slow positrons, but in doing so, a spin polarized slow positron beam is realized. The helicity, or projection of a particle's spin onto the direction of momentum, is proportional to the velocity of said particle (h = ±v/c [95]). Radioactive decay is mediated by the weak interaction, the only known Parity violating interaction, and this asymmetry results in the spin-polarization of positrons emitted from ^{22}Na in a magnetic field. The spin-polarization is approximated by the difference in forward emitted and back reflected positrons upon the total positron number.

2.1.2 Source Stage Equipment

The ^{22}Na source and the solid Ne positron moderator are cooled to a temperature of ~ 8 K using a cryostat depicted in Fig. 2.1 (ARS DE204SB) temperature controlled with a CryoCon 34 unit. The chamber housing the ^{22}Na is pumped down to $\sim 1 \times 10^{-8}$ Torr by a turbo molecular pump (TMP 1) backed by a scroll style roughing pump. Differential pumping by an Ion pump and a second turbo molecular pump (TMP 2) is necessary to reduce the flow of gases leaked into the trap stage about 6' from the source. The deposition of solid Ne is computer controlled by a series of pneumatic valves and regulated with a mass flow controller. For diagnostic purposes, a linear translator may moves a phosphor screen in place to terminate the positron beam. A 2-D image of the projection of the moderated positron beam may then be captured on a CCD camera. At the same time the count rate from a NaI(Tl) gamma-ray detector precisely located above the phosphor screen is used to measure the total positron beam strength with a precision of 1 percent and with a constant systematic uncertainty of about ±10 percent uncertainty.

2.1.3 Growing a solid Neon positron moderator

Below is given the standard procedure used to grow a solid Ne moderator. The operator must be thoroughly familiar with all the terminology, the names and locations of the various components, and the computer programs that are controlling the valves, currents and voltages. The gas bottles for Ne, Ar, SF_6, N_2 must be operating properly. Vacuum system and all its components must have been properly baked out, and must have reached a stable operating pressure before beginning the procedure.

1. Take appropriate safety precautions (interlocks, gate valves (GV), *etc.*)
2. Bake off old moderator by turning off cold head motor (T$\gtrapprox$13 K)
3. Increase temperature to 35 K to remove other frozen gases from vacuum system.
4. Vent mass flow controller (MFC) GV (leave both GVs open and set MFC to 0)
5. Reduce cold head temperature to a growing setting 9.2 K
6. Let temperature stabilize and then close turbo GVs
7. Set MFC to 3 SCCM (Pressure should rise to $\sim 2 \times 10^{-4}$ Torr)
8. Grow until count rate saturated ($\sim$ 5min, $\sim$ 3 kcounts/s)
9. Set MFC to 0, close MFC GVs
10. Anneal moderator (T = 9.5 K 5 min)
11. Open turbo GVs
12. Turn on ion pump
13. Store at a lower temperature of 8 K

Notes:

- Moderator count rate increases by about a factor of 2 over the next 15 minutes
- Moderator count rate continues to slowly improve over next 8 hours
- Moderator count rate decrease $\sim$ 4% per day

- Introducing trap gases via source-trap GV increases count rate, but also increases degradation rate

2.2 Buffer Gas Trap

Positrons from the source stage are moderated with an effective efficiency of 0.4% (3.6×10^6 slow positrons per second for a 30 mCi source), and are subsequently trapped in a buffer gas trap based on that described in reference [82] with 20% nominal efficiency thus yielding $\sim$ 10 ns bursts of $\sim 3.6 \times 10^5$ positrons at a rep rate of 2 Hz. During the fill phase, the positron trap electrostatics are set to that shown in Fig. 2.3 (middle) and slow moderated positrons are collected for $\sim$ 500 ms. Thereafter, the trap switched to the store phase, and the electrostatic profile changes to that represented by the dashed line for $\sim$ 5 ms. Lastly, a MOSFET drives the gate electrode to ground, releasing positrons from the trap. The procedure for tuning trap electrode voltages is achieved by changing the voltage drop between adjacent stages keeping all other voltage drops fixed. Positrons are dumped with $\sim$ 20 eV of kinetic energy, an adjustable parameter. The main magnet of the trap is 36" long, made with rectangular 1/8" x 1/16" wound 1" thick on a 6.625" water cooled form, and with 3.14" wide trim coils wound 0.5" thick placed on both ends. It produces a central field of 1000 gauss with a current of 16 A. The two-stage electrode Surko style trap[168] is schematically shown in Fig. 2.3 (left) and installation within the main electromagnet shown Fig. 2.3 (bottom).

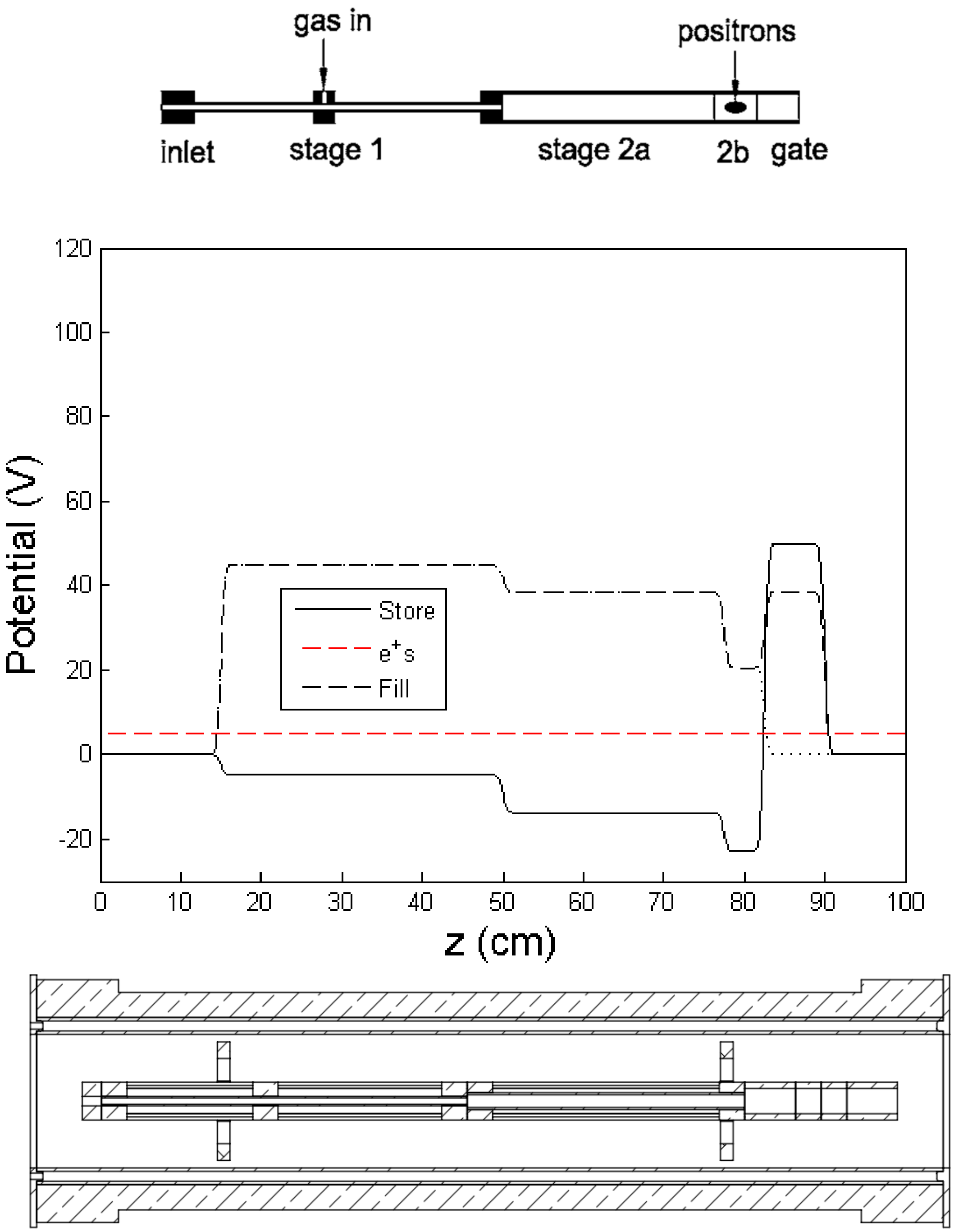

Figure 2.3: Surko style buffer gas trap electrode schematic (top), electrode potentials (middle), and trap cutaway (bottom)

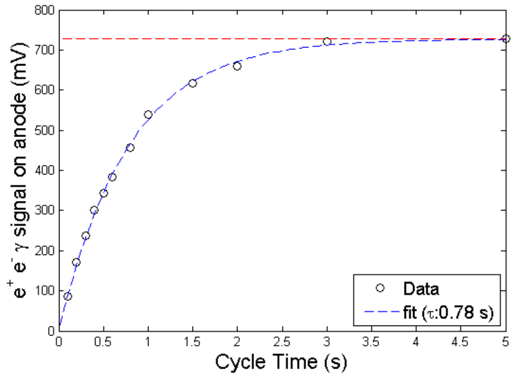

Figure 2.4: Trap positron output as a function of fill time.

Throughput is maximized by tuning the leak rates of N_2 and SF_6. The N_2 is directly injected into stage 1 as shown in Fig. 2.3 (left) resulting in a high trap efficiency in stage 1 and a longer positron lifetime in stage 2. The SF_6 is leaked into the entirety of the trap vacuum chamber from one end at a low pressure of $\sim 1 \times 10^{-6}$ Torr. Afterwards, the positron mean lifetime within the trap is measured by storing for ever increasing storage times until the total number of positrons trapped is asymptotically reached (see Fig. 2.4).

Chapter 3

Magnetic Switch-Yard for Pulsed Positron Transport

3.1 Introduction

The positron beam-line begins with a single, solid Neon moderated [142], ^{22}Na positron source that loads positrons, 28 percent polarized along the magnetic field axis, into a buffer gas trap [83]. Operating at a 2 Hz repetition rate, the buffer gas trap dumps $\sim 10^5$ 14.5 eV positrons [135] time-bunched to 25 ns full-width half-max (FWHM) and with an energy resolution and beam diameter of $\sim$ 0.25 eV and 1 mm FWHM. The positron pulses are directed to one of three independent experimental stages by a magnetic switch-yard that preserves the positron spin polarization. The first experiment is designed for high-precision measurements of the Ps 1^3S-2^3S interval. The second experiment makes high density collections of positronium using a positron accumulator [168] detailed in Chapter 8.

The accumulator is supplied with positrons by a 12 m transfer beam-line with a number of 90° bends. The third output of the switch-yard could be used for various other experiments, the most likely of which would be the measurement of spin polarized Ps emission velocity spectra from single crystal Weyl metals [98]. It could also be used for a variety of other less urgent projects, like measuring depth profiles of defects in materials [80], Ps emission velocity spectra from single crystal metals [98], metal-oxide framework crystals (MOF's) [68], and other materials in which Ps exists as de-localized Bloch states [21, 85]. The magnetic transport of charged particles in general is discussed in Section 2.1.1. In the next section we present the design our magnetic switch-yard and show how the phase space of the transported positron bursts is preserved using adjustable magnetic correction coils.

3.2 Magnetic Switch-Yard Design

All transport lines are constructed from 304 stainless steel 2.75" con-flat flanges and 1.5 inch OD vacuum pipes wrapped with two layers of rectangular magnet wire (0.064" × 0.125") resulting in a nominal transport field of ~ 230 Gauss for 32 A. The magnetic switch-yard has 3 co-planar outputs separated by 45° with the inlet opposite the central output beam line. Incoming and outgoing trajectories are symmetric about the plane perpendicular to the positron trajectories and the center of the apparatus (see Fig. 3.2).

A pump-out port is installed off-centered on the bottom side of the switch-yard to allow for 3 rectangular steering coils. Each of these guiding magnets is: centered at the shared intersection of the incoming and outgoing beam lines, and tilted so that its normal

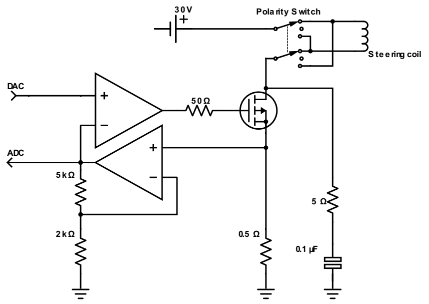

Figure 3.1: Constant current pulsing circuit for correction coil adjustments.

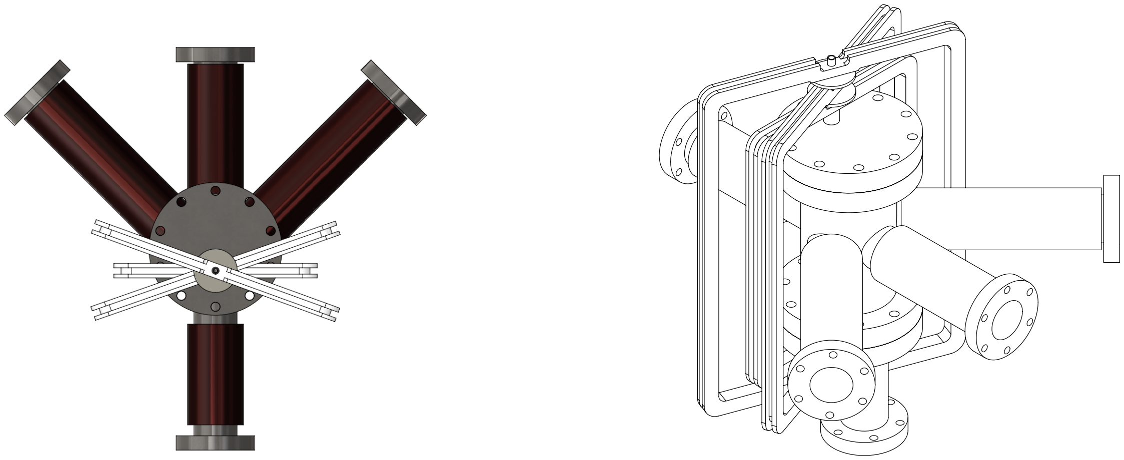

Figure 3.2: Magnetic switch-yard top-down (left) and isometric (right) schematics

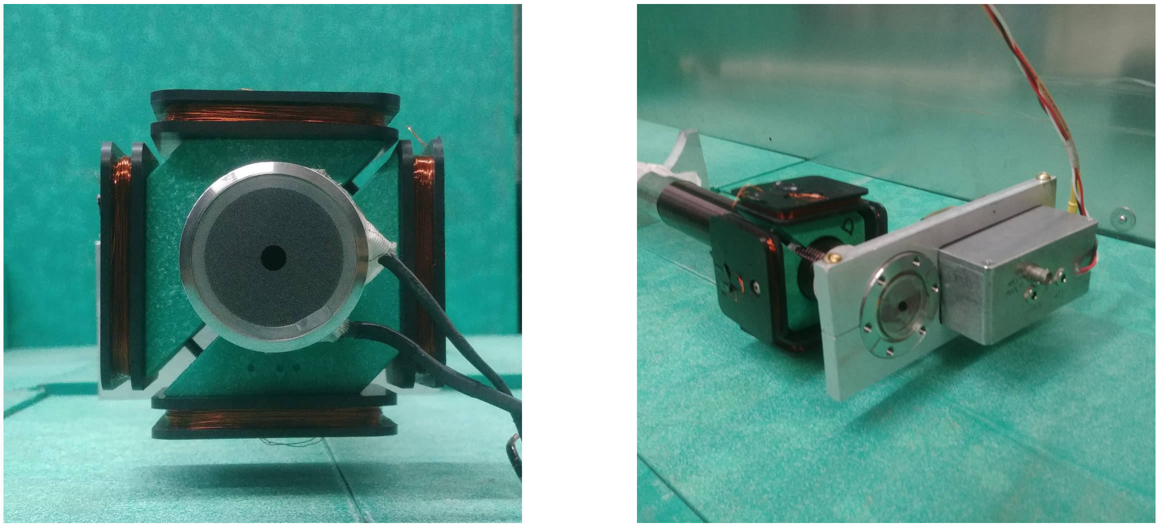

Figure 3.3: Magnetic transport alignment meshes and correction coils (left), and gamma-ray detector (right)

bisects the angle subtended by one of the outputs. However it was later discovered that efficient transport did not require use of the bucking coils and is discussed in Section 3.4.

The solenoidal guiding fields of the incoming and outgoing ports are provided with gaps so that the ends are equidistant to the center-point. The switch-yard is capable of switching the transport lines at the same repetition rate as the positron trap without loss of positrons if solid state relays are used.

To achieve efficient transport of positrons through the long flight path of our 10 m positron beam line with its many 90° bends requires the use of many pairs of steering coils that are controlled by gamma ray detectors that give a minimum reading when the beam is passing through the center of the flight tube. Without this control, the beam could be reduced or completely cut off, the pulse time-width could be much longer, and the spread in the positron energies could be broadened. To resolve these problems, the pulse was centered throughout transport line by (1) installing a 70% transmitting mesh with a

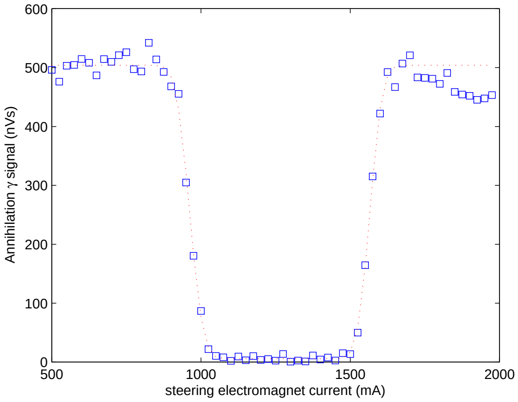

Figure 3.4: Horizontal deflection scan across Ni mesh aperture.

0.25 in hole punched through the center at each flange where coil sections were mated; (2) mounting trim coils at each flange mating tuned to make the magnetic field more uniform; (3) installing XY steering coil pairs before each mesh; and (4) centering the positron pulses at each mesh by systematically adjusting the coil currents from the beginning of the flight tube to its end by a computer-controlled variable constant current circuit detailed in Fig. 3.1.

The transport solenoids originally operated at a constant 10 A leading to a transport field of 73 Gauss, but this lead to zero throughput. When the current supply was changed to a pulsed supply, with currents from 16 A to 32 A at a duty cycle of 10 ms on and 500 ms between pulses, the transport efficacy increased greatly at 16 A due to the higher magnetic field. A further increase in transport current to 32 A (230 Gauss) diminished effects caused by stray fields and reduced the diameter of the transmitted pulse to 0.033 in (measured using Figure 3.4), which made it possible to guide the beam through the 0.25 in hole within each mesh without any loses.

It was found that the transport efficacy was greatly improved by moving the magnetic switch-yard apparatus from 1' to 2' away from the buffer gas trap (discussed in 2.2), thereby reducing the residual field from 125 Gauss to 25 Gauss along the nominal 230 Gauss transport field. The added length permitted the installation of an electrically floating 0.1×12 in^2 pumping restriction with a voltage feed-through. The pressure of $\sim 2 \times 10^{-5}$ Torr typically required for the buffer gas trap would compromise positron transport, but the pumping restriction, along with differential pumping from the switch-yard center, reduces this pressure by a factor $\gtrsim 100$. A centering algorithm discussed later uses correction magnets, gamma-ray detectors, and 50% transmission Ni meshes (pictures in Fig. 3.3) installed at flanges and can result in perfect transmission of positrons.

3.3 Magnetic Transport Calibration

The 3 rectangular magnets mounted near the center of the switching-yard were originally tuned as follows: the tilt was set to bisect the angle subtended by the inlet and respective outlet; and the current was set as to minimize the gradient of the magnitude of the magnetic field through the axis of transport calculated from a model of the switching-yard. Following transfer through the switch-yard, XY Correction coils are installed in pairs to increase the correction magnet field homogeneity, and are mounted just before a 70% Ni mesh. Meshes are installed to detect annihilation gammas due to positron trajectories far from the center of the chamber without compromising pumping speed through the 12 m transport much. Correction coils are adjusted using a pulsed variable constant current supplies to deflect field lines such that positron trajectories intercept Ni meshes or even

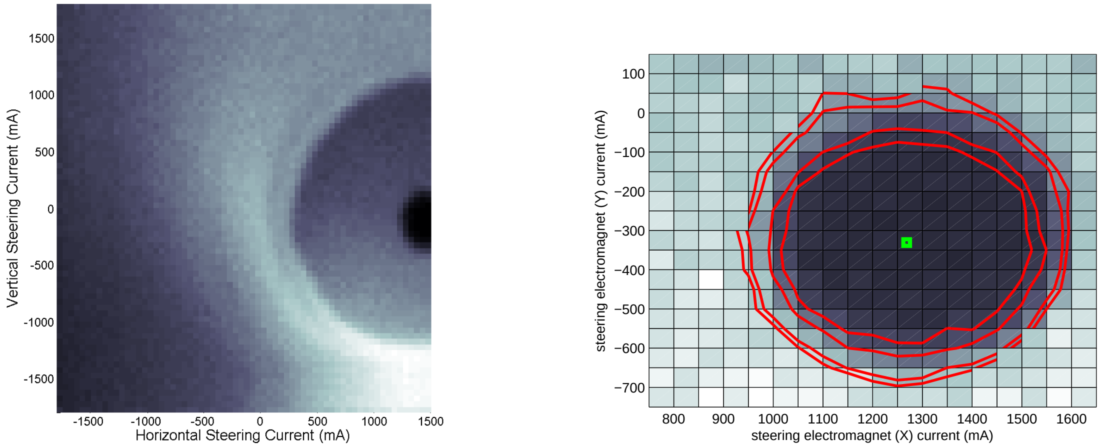

Figure 3.5: Annihilation gamma signal as positron trajectories are deflected near a Ni mesh installed flange mating.

the stainless steel vacuum tube illustrated in Fig. 3.5 which shows the annihilation gamma signal (high count rate corresponding to lighter color) as positron trajectories are rastered. The dark center visible on the right is a lack of signal and thus positrons are going through the center of the flange mating. The count rate increases as positrons intercept the Ni mesh and increases again by a factor of ~ 2 as positrons annihilate on the stainless steel chamber with the greatest count rate measured below the aperture in the mesh as pictured in Fig. 3.5. This is due to the placement of the gamma-ray detector in this direction and this placement also explains the variation in count rate from the bottom to top of the mesh shown in Fig. 3.5.

It was found that transportation of positrons through areas with high magnetic field gradients (*i.e.*, far from chamber centers at flange matings) led to deleterious effects resulting in increased energy dispersion. To ensure positron trajectories went through the center of flange matings, an annihilation gamma spectrum was recorded as shown in Fig. 3.5

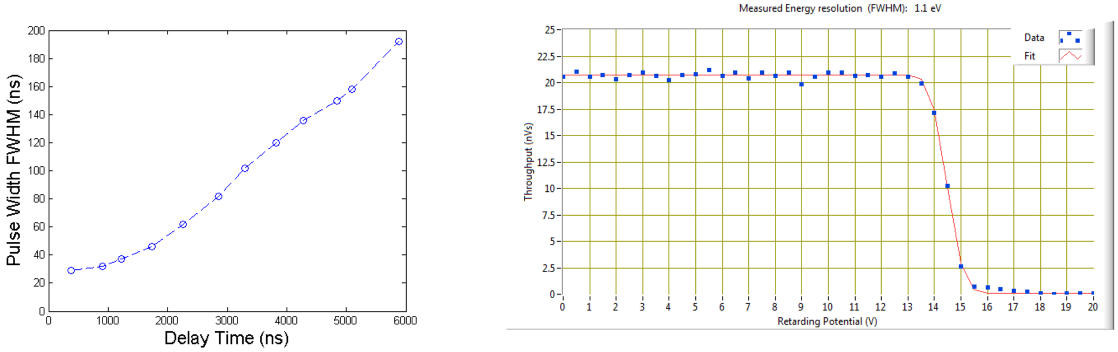

Figure 3.6: Positron Pulse width measured along 12 m transport (left) and measured energy dispersion after transport (right)

(left), but focused around the mesh aperture. After correctly matching correction coil pairs, these scans resulted in contours at the 50% annihilation rate that were only slightly elliptical and a quick elliptical fitting routine calculated the centroid as shown in Fig. 3.5 (right). Improvements could be made to this algorithm that take into account the variation in relative annihilation gamma-ray signal before contours are calculated, but as will be shown later, this method leads to nearly perfect transmission.

Transport efficiency was measured using a long flight path to improve sensitivity. Pulse width and throughput measurements were made using a $PbWO_4$ scintillator coupled to a Planicon MCP-PMT, and energy dispersion measurements employed a stack of electrodes contained within the accumulator (discussed in Section 8). Figure 3.6 (left) shows the evolution of the positron pulse width as positron bursts travel down the transport. Pulse widths are measured at flange matings and plotted vs the delay time detected relative to the dumping of positrons from the trap and range from $\sim$ 25 ns to almost 200 ns near the end of the transport. The energy dispersion (right) after positrons have been transported 12 m and through a positron accumulator was measured to be $\sim$ 1.1 eV.

3.4 Perfecting Magnetic Transport

Preliminary tests incorporated a single $0.5 \times 0.5 \times 1$ in^3 LYSO crystal coupled to a Hamamatsu PIN photodiode, but have been expanded to include ~ 20 detectors, permitting an automated recalibration, comprising a $0.5 \times 0.5 \times 2$ in^3 BGO crystal mounted to a Hamamatsu pin diode. The signal from all detectors is coupled together and distinguishable as the typical spacing between neighboring meshes is ~ 1 m corresponding to 443 μs for 14.5 eV positrons. The use of small scintillating crystals greatly reduces long distance annihilation gamma detection coming from other nearby meshes, however, since this requires that the detector be placed very close to the survey location of annihilation gammas, there is a measurable change in gain due to a change in solid angle coverage and detection efficiency as the beam is steered from one side to the other as was shown in Fig. 3.4.

Correction coil current sensitivity was explored as shown in Fig. 3.7 for the coil about the center of the switch-yard. De-tuning of one parameter (bucking coil current or angle relative to the incident positron burst) was correctable by changing the incoming positron trajectory with xy correction coils positioned just before the switch-yard. The result implies that the bucking coils are not critical if incoming positron trajectories are appropriately set. With the bucking coils removed, the throughput, energy dispersion, and time broadening of the transported positron beam are measured at the end of the 12 m transport using the aforementioned correction coils. The results, plotted in Fig. 3.8, shows that critical parameters such as the energy dispersion of the transported positron burst is insensitive to small deviations away from the working calibration.

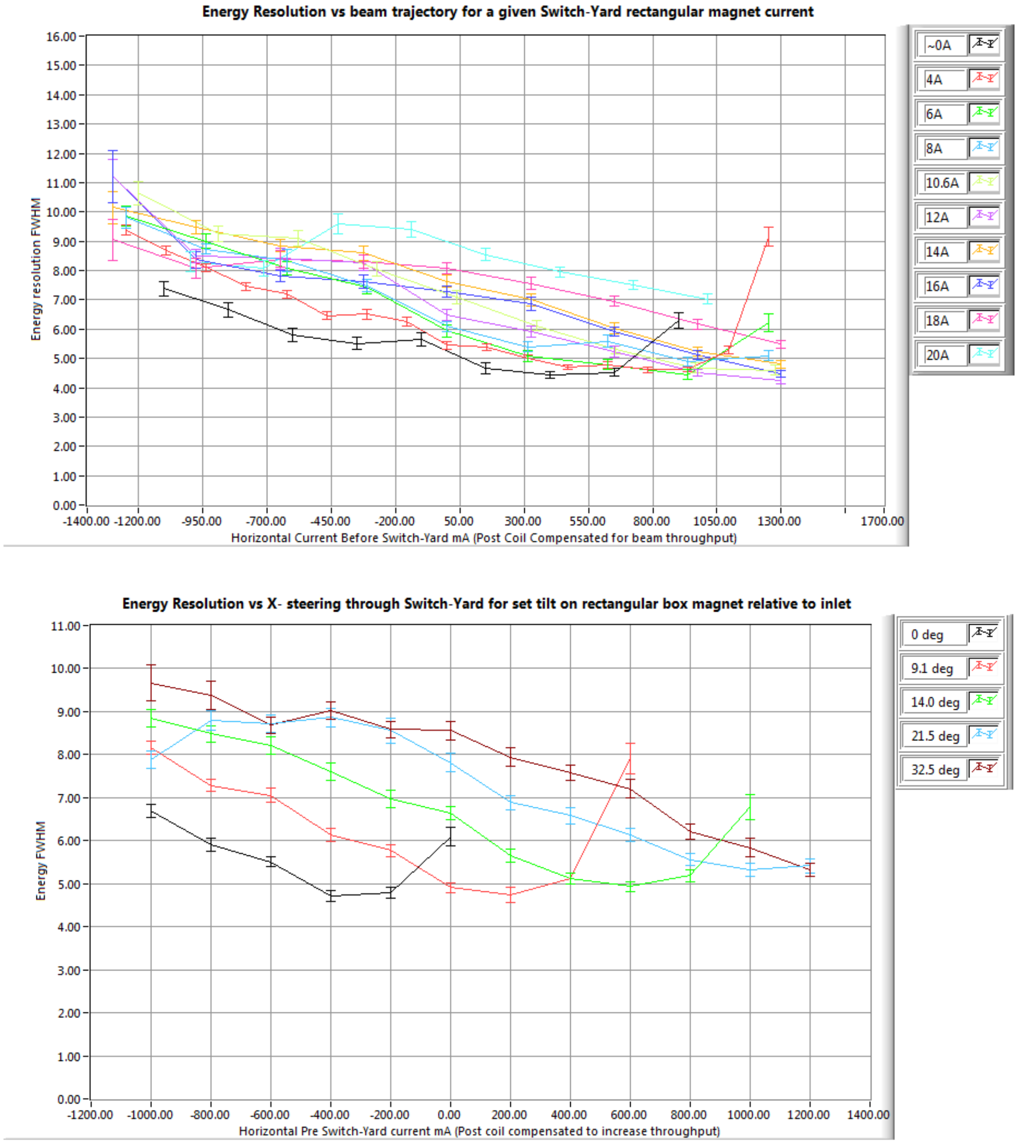

Figure 3.7: Switch-yard bucking coil calibration and parameter sensitivity.

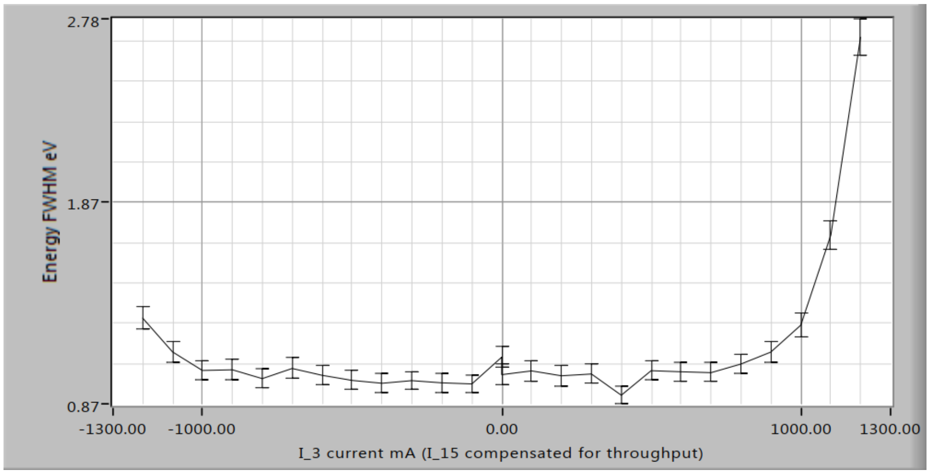

Figure 3.8: Correction coil calibration before switch-yard showing bucking coils not needed. 200 mA of correction current corresponds to a 1/4" of deflection.

Perfect transport is realized upon transporting and re-capturing all positrons 12 m in a high vacuum positron accumulator. A narrow positron energy dispersion, shown in Fig. 3.6 (right), increases trapping efficiency. Since trapping occurs over many positron bounces within the accumulator, the accumulator inlet must be gated to capture positron bursts. The consequence of these two facts means incoming positron bursts must be spatio-temporally short as to entirely fit in the electrostatic trap. The pulse width of ∼ 200 ns shown in Fig. 3.6 (left) means the incoming ∼ 20 eV positron burst has expanded to a little over 0.5 m, and therefore, does not fit in the accumulator trap. Installation of a computer controlled floating electrode ∼ 8 m along the transport corrects the pulse broadening. Tuning of the potential via an arbitrary waveform generator results in a perfectly transmitted positron burst re-captured by the accumulator, verified by the absence of annihilation gamma-rays detected outside of the accumulator and along the transport.

Chapter 4

Positron HV Buncher Accelerator and Magnetic Field Extraction

Often in positron science it is desirable to perform measurements in a field free environment so that calculations need not include perturbations such as in spectroscopy or brightness enhancement [134], however there is often a serious compromise made limiting the count rate and uncertainties in measurements. Using the positron beam line detailed in Chapter 2, 10 ns bursts of positrons at a repetition rate of 2 Hz have been used to test a high voltage positron buncher-accelerator.

4.1 Accelerator Design

The buncher-accelerator, schematically represented in Fig. 4.1, consists of a stack of 42 electrically coupled Cu electrodes with each electrode measuring $\sim$ 23 mm in major diameter, 10 mm long, and with an inner diameter of 12.7 mm. The stack is assembled

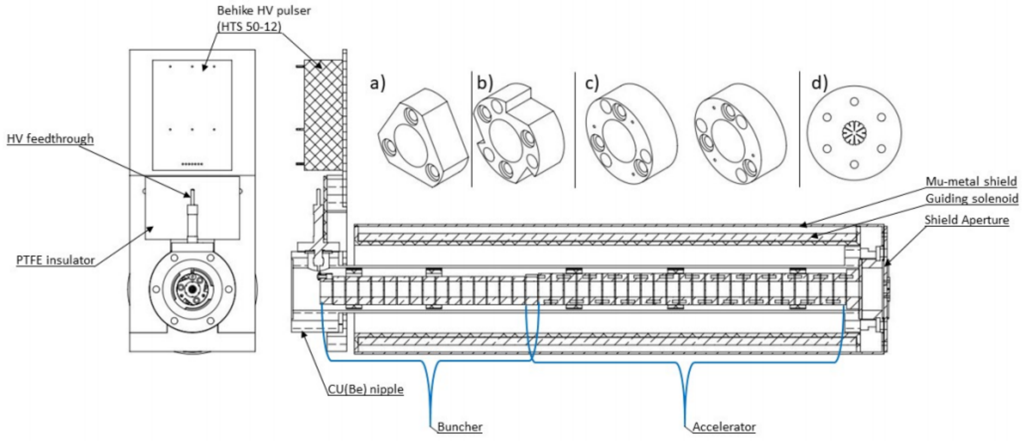

Figure 4.1: Schematic for buncher-accelerator used for extraction of energetic positrons from a magnetic field.

on three threaded polyetheretherketone (PEEK) rods, with alumina spacers inset between each pair of electrodes. The rods are screwed directly into the exit electrode and plate, with stainless nuts securing the stack on the entrance electrode. In initial tests, the PEEK rods were found to maintain a static charge, causing beam deflection at the entrance, and so the ends are trimmed short, and tantalum tabs are spot welded across the opening of the nuts to shield the beam from the rods. Due to the differences in electrical connection, the accelerator and buncher are comprised of electrodes with differing geometries.

4.1.1 Bunching section

The 17 triangular electrodes (see Fig. 4.1 (a)) composing the bunching section are electrically coupled in a three-fold symmetry using 1-3 strands of resistive wire (30Ω/ft) such that (1) magnetic fields produced near the axis by the resisitive wires are greatly reduced; and (2) the resulting electric potential on the center axis approximates a parabolic curve seen in the inset of Fig. 4.2. A parabolic potential was chosen to minimize a positron pulse

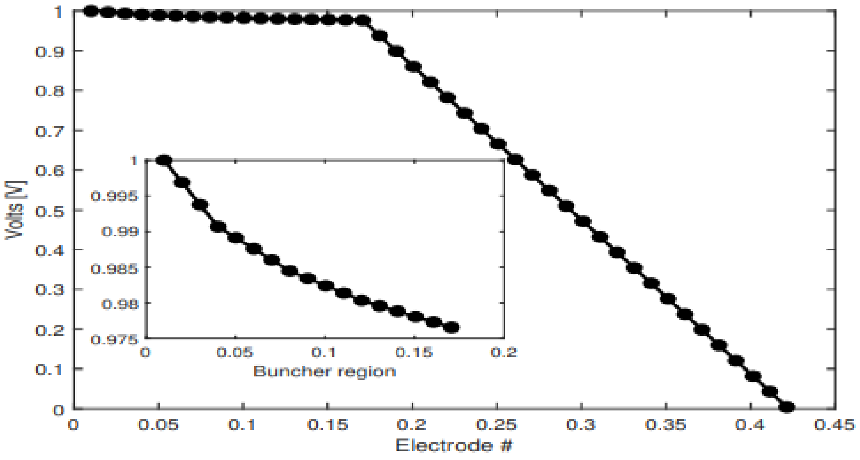

Figure 4.2: Electrostatic potential along center axis of buncher-accelerator normalized to unity.

length with zero kinetic energy. It was found that other arrangements such as a linear ramp led to better temporal bunching. A constant value bunching section was used elsewhere where minimal positron energy dispersion is desired.

4.1.2 Accelerating section

The accelerator section is comprised of 25 electrodes, with each electrode electrically coupled by three parallel 12 Ω resistors in an alternating fashion to accommodate alumina spacers while reducing the total length of the accelerator. The resistors were sandblasted and treated for increased high vacuum compatibility. The final electrode is directly coupled to ground via a custom Cu gasket with a 1/2" inner diameter for use in a standard 2.75" CF flange.

The completed electrode assembly measures $\gtrsim 100\Omega$ in resistance, translating to a 100 ns 5 kV potential rise creating a 50 A current draw. The current loop is closed

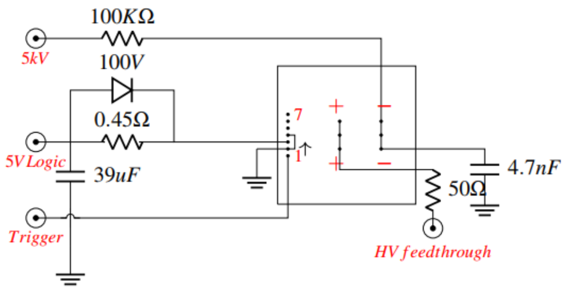

Figure 4.3: Accelerator high voltage connections for Behlke HTS-2012.

through the vacuum nipple housing the accelerator, which is a custom design 2.75” CF nipple. The nipple is constructed from a Cu tube braised to BeCu flange ends, which ensures that the sealing knife-edges are harder than the Cu gaskets used. Cu is chosen for its exceptional electrical conductivity, thus minimizing additional resistance. HV is delivered through a miniCF SHV feedthrough attached to the top of the entrance flange. A Behlke HTS-2012 high voltage transistor switch is mounted directly above the flange on a brass assembly which clamps directly to the flange. A brass box houses the switch and associated electronics, with circuit diagram shown in Fig. 4.3, protecting the nearby electronics from high-frequency noise.

Outside of the vacuum canister of the buncher-accelerator a confining solenoid, supported by aluminum spacers, provides a guiding a magnetic field. Rectangular correction coils are added to the solenoids exterior to maintain positron transport along the central axis. Encasing the electromagnetic buncher accelerator is a 2 mm thick half-closed mu-metal cylindrical shield. A mu-metal terminating plate with a mu-metal “spider” [93] (see Fig. 4.1) installed over a 1/4” aperture provides an exit hole for the positrons as well as

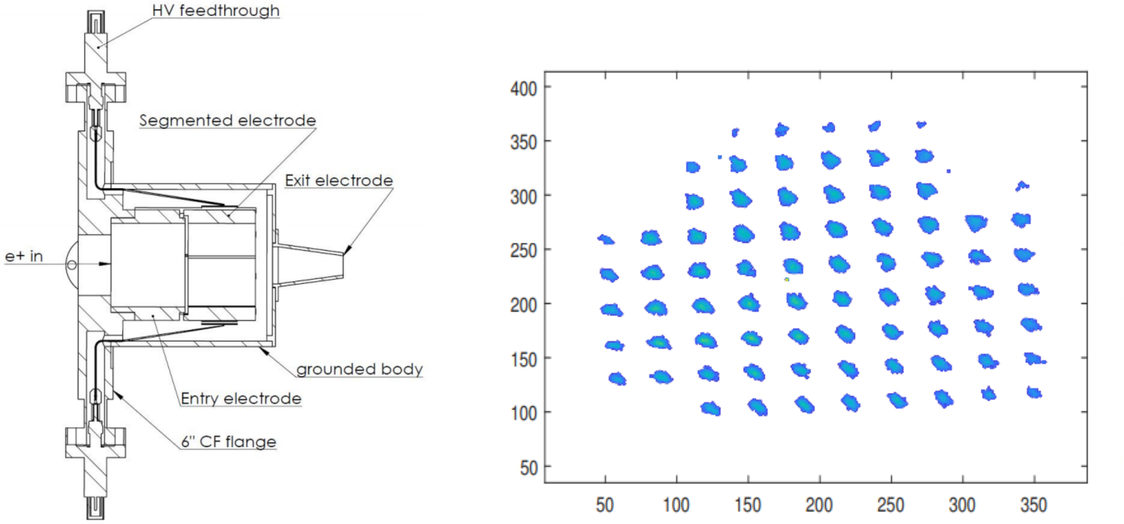

Figure 4.4: Schematic for electrostatic optics (left) for focusing of positrons to a nearly field free space and patterned accumulated positrons from varying deflector voltages (right).

a means of quickly terminating the guiding magnetic field. The spider, results detailed in Section 9.1, has the effect of breaking the scale of the magnetic field into smaller domains, resulting in a more rapid decay of the field following the aperture, and thus a decrease in the expansion rate of the beam following extraction from the confining magnetic field.

4.2 Electrostatic Optics

Following extraction of the aforementioned positron beam (see Section 4.3) from the magnetic field, an electrostatic lens shown schematically in Fig. 4.4 focuses positrons onto a target located in a nearly field free region. The design is based on a decelerating Einzel lens [105], and is composed of three cylindrically symmetric electrodes made of 304-SS, but with the tertiary electrode tapered as to quickly eliminate stray electric fields outside of the lens assembly, an unwanted perturbation on spectroscopic measurements. The electrodes are mounted directly on a CF flange, which features four radial mini-CF SHV feedthroughs coupled to four symmetrically cut segments of the central electrode via SS wire in Teflon tubing. The best focus would be achieved with a steep focusing angle, however the position of the target far from the lens assembly demands a convergence angle of at best $\sim 7^\circ$ and thus limits the achievable focus.

4.3 Accelerator results

The resulting positron beam following magnetic field extraction and subsequent electrostatic focusing is recorded using: (1) a fast gamma-ray detector composed of $PbWO_4$ scintillator coupled to a Hamamatsu R1924A photo-multiplier tube; and (2) and image of energetic positrons impinging a high vacuum Kimball Physics Phosphor screen recorded by an ATIK-420 CCD. After optimizing the focus of the electrostatic optics, focused positron bursts were patterned on a phosphor screen, results presented in Fig. 4.4 (right), by changing the relative potential of the deflecting electrodes discussed in section 4.2 in steps of 50 V. The resulting calibration of ~ 300 μm per 1 V of relative deflection maintains linearity above ± 150 V, however, the minimum FWHM positron spot size ranges from ~ 250 μm to ~ 1300 μm. A similar spot size was measured in-situ by recording the fraction of produced Ortho-Positronium production as the positron beam is scanned across a target of known size.

Chapter 5

Ellipsoidal Electrostatic Focusing Mirror for Rydberg Positronium

The information in the following is taken from the following previously published materials [102, 103].

5.1 Introduction

Production of long lived Rydberg Ps can lead to more precise spectroscopy as slower atoms can be used. Ground state Ps has a mean vacuum lifetime of 124 ps and 142 ns for the singlet and triplet state respectively and so measurements are typically made over the first few cm of the Ps producing targets with Ps velocities of about 100 km/s. Rydberg Ps atoms are Ps atoms excited to a high principle quantum number ($n \gg 1$), and have a long mean vacuum lifetime on the order of n^3 leading to slower atoms, longer time of flights available, and thus lower uncertainties in measurements. For example, in the performance study of a Rydberg electrostatic mirror, time of flights up to 60 μs were detected 6 m away corresponding to Ps velocities as slow as 1×10^5 m/s.

Like other polar molecules, large Stark shifts of Rydberg Ps permit the manipulation of Ps trajectories using inhomogeneous electric fields [181, 22]. For instance, Rydberg H atoms reflect from quadropole electric field gradients [176]. The mirror described here is nearly achromatic as the short range repulsive potential results in a specularly reflecting surface. This mirror has great utility in the manipulation of slow Rydberg beams including but not limited to tuning Ps atom energies, as well as steering, collecting, and focusing of Rydberg beams down to diffraction limited spots. Other uses include precise Ps trajectory measurements in a precision measurement of the $1S_1$-$2S_1$ interval and antimatter free fall acceleration as well as increased Ps collection efficiency for many spectroscopic techniques using Ps emission from solids.

The basis for the manipulation of Rydberg atoms is the fact that an externally applied electric field $\vec{F}$ causes the states of an atom to exhibit Stark shifts with energies given in the case of Ps by [90]:

$$E_{Stark}(F,n,k,m) = \frac{3}{2} nkea_{0_{Ps}}|\vec{F}| + ... \approx 1.6 \times 10^{-10} eV \times nk|\vec{Fa}| \tag{5.1}$$

which to first order is independent of the magnetic quantum number m. Here, $|\vec{F}|$ is in V/m, n is the principal quantum number, $a_{0_{Ps}}$ is the Ps Bohr radius, and k is the difference between the parabolic quantum numbers n1 and n2 defined in a coordinate system with the electric field along the axis of quantization. The permitted values of k span the range from $-(n-|m|-1)$ to $+(n-|m|-1)$ in steps of 2.

The potential energy of a slowly moving atom, for which the axis of quantization will follow the direction of an external electric field adiabatically, will be $U(\vec{x}) = E_{Stark}(\vec{x})$. Suppose an infinitely long cylinder of radius R and with its axis along $\hat{z}$, on which is imposed a periodic electrostatic potential$V(R, \theta, z) = V_0 sin(j\theta)$, where θ is the azimuthal angle and j is an integer $j > 0$. The potential within the cylinder at radius r is $V(r, \theta, z) = V_0(\frac{r}{R})^j sin(j\theta)$and the magnitude of the electric field is $|\vec{F}(r, \theta, z)| = |\vec{\nabla} V(r, \theta, z)| = jV_0(\frac{r^{j-1}}{R^j})$ with no θ dependence. For $j \gg 1$, a slow Rydberg atom approaching the inner surface of the cylinder experiences a short-range potential that is approximately exponential,

$$U(\rho) \approxeq 1.6 \times 10^{-10} eV \times nk \frac{V_0}{\rho_0} exp \frac{-\rho}{\rho_0} \tag{5.2}$$

where $\rho = R - r$, $\rho_0 = \frac{R}{j-1}$ and V_0 and ρ_0 are in units of volts and meters. This potential is only dependent on the distance ρ from the surface. States with positive k will see a sharply rising repulsive potential that may be used as a smooth mirror surface for Rydberg atoms. The discussion above for Rydberg Ps atoms is valid, with a change of energy scale, for any Rydberg atom. While avoided level crossings will limit the maximum kinetic energy of the atoms that can be reflected from a periodic potential mirror, this will not be a significant limitation for atoms with a sufficiently small radial component of velocity.

5.2 Rydberg Mirror Description

A concave cylindrical surface with an azimuthally periodic electrostatic potential was made to radially reflect Rydberg Ps atoms. The Rydberg mirror is a truncated oblate ellipsoid of revolution, with a 1.50±0.01 m focal length and 96 mm radius. We now describe

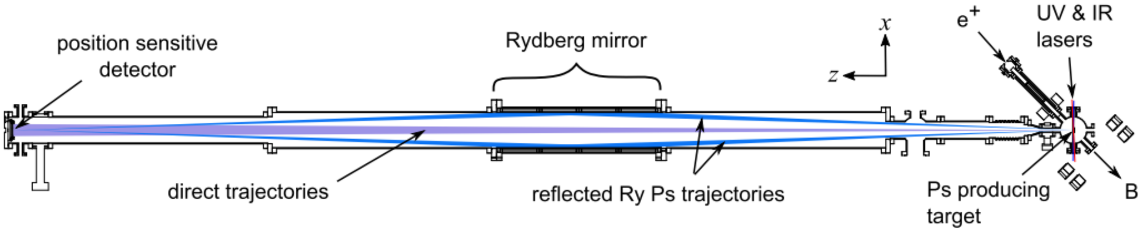

Figure 5.1: Schematic of Rydberg flight path with mirror centered between Ps producing target (right) and Ps atom detector (left)

our experiment using a 6 m flight path, as illustrated in Fig. 5.1, and a Rydberg mirror, shown in Fig. 5.2 (a) and (c), to measure Ps times of flight (TOF) with mirror on and off as plotted in Fig. 5.3, and the quality of the Rydberg Ps focal spot illustrated in Fig. 5.4 and Fig. 5.5. We have constructed a periodic potential electrostatic mirror in the form of a wire structure of length 0.9 m and 96 mm mean inside radius in the shape of a truncated oblate ellipsoid of revolution, as shown in Fig. 5.2 (a) and (c). The mirror is composed of a cylindrical array of 360 stainless steel wires 914 mm long and 1 mm in diameter, with alternating positive and negative potentials. Each wire is supported at the inner edges of one of two sets of 5 electrically isolated stainless steel disks of varying inside radii chosen to give the desired curved inner surface for the array. This structure is mounted coaxially near the center of the 6 m long vacuum pipe illustrated in Fig. 5.1 with a 1.8 mm FWHM Ps emitting spot at one end and a position-sensitive microchannel plate (MCP) Rydberg atom detector at the other. MCP details discussed in 7.

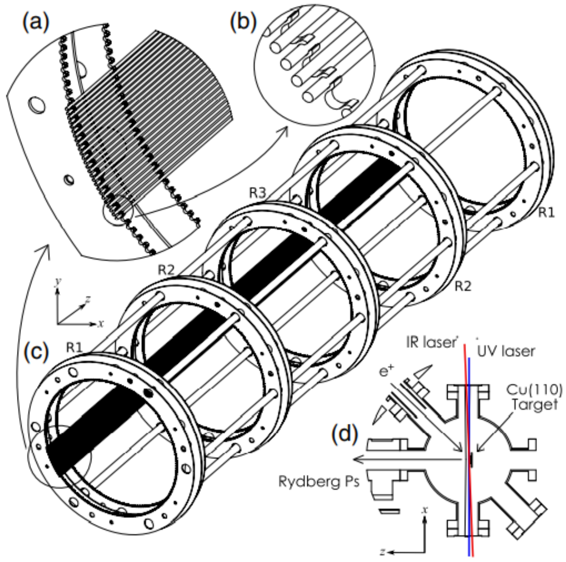

Figure 5.2: Schematic of Rydberg mirror with subset of 360 wires illustrated (c). Insets: (a) and (b) interleaved wires detailed; (d) target chamber with Cu (110) Ps producing target.

5.3 Rydberg Mirror Optical Tests

The mirror was tested in air by measuring the image of a 3 mm square white light LED source positioned on the mirror axis at $z = -3.00 \pm 0.01$ m from the center of the mirror (at $z = 0$). The light reflected on a paper screen on the other side of the mirror ($z > 0$) was recorded with a CCD camera. The position for obtaining the maximum intensity at the center of the image was $z = 2.95 \pm 0.05$ m, in agreement with the mirror's design parameters. The image had an intensity distribution in the image plane (see fig5.4(c)) that is consistent with a 1/r distribution, expected from the superposition of the light reflected from the circular cross section wires composing the mirror, folded with a 2D Gaussian of 21±3 mm FWHM. The larger than expected optical focal spot diameter (which for a perfect lens would be comparable to the ~ 3 mm diameter of the LED used), is explained by a slight bowing of the 1.0 mm diameter mirror wires with a ~ 25 μm peak-to-peak amplitude and a period of ~ 15 cm in addition to a bowing of comparable magnitude due to the gravitational sagging of the wires between the supports. A simulation shows that for a point source of Rydberg Ps, the higher harmonics of the potential due to its not being exactly equal to $V_0 sin(j\theta)$ on the mirror surface will result in an intrinsic Rydberg Ps image ~ 0.5 mm in FWHM for 10 V mirror potentials.

The position sensitive detector comprises a pair of 75 mm diameter Photonis channel plates (MCPs) in front of a $\sim 25\ \Omega$ per square, 90×90 mm^2 indium-tin oxide coated glass resistive anode readout plate. Rydberg atoms are ionized by a 3 mm wide region of electric field $\sim 10^6$ V/m between the entrance to the MCP and an 80 mm diameter grounded grid [100] made of parallel 25 μm diameter tungsten wires with 1 mm spacing. Signals from the corners of the anode are amplified and recorded using a LeCroy HDO4054 oscilloscope. The detector was calibrated using UV light and a patterned mask. Pin cushion distortion [8, 116] is corrected to first order using the transformation $(x, y) \rightarrow (\frac{x}{1+\alpha y^2}, \frac{y}{1+\alpha x^2})$ with $\alpha = 8$ chosen to give an optimally circular image of the active area of the MCP disk (see Fig. 5.4 (a)). The resolution near the center of the detector is 4.3 ± 1.0 mm FWHM. The mean amplitude of the signals from the UV light shining on the MCP surface are known to be about 20% of the mean amplitude of the signals from Rydberg Ps atoms which are field ionized, with the freed positrons subsequently accelerated into the MCP with ~ 2.5 keV of kinetic energy [100]. Because of this the positional resolution for Rydberg Ps is probably about 2 mm FWHM, although we have not verified this directly.

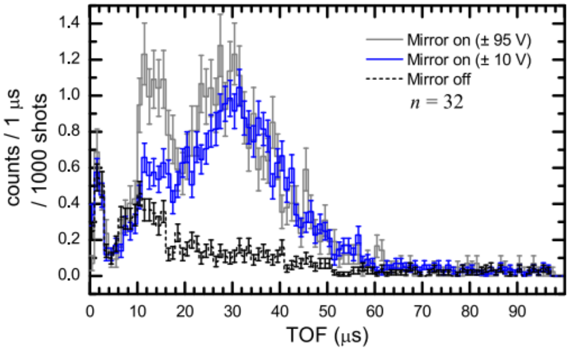

Figure 5.3: Ps time of flight data for mirror on/off, and ± 10 and ± 95 V potentials applied.

5.4 Rydberg Mirror Ps tests

Positronium for our experiment is formed when 10 ns bursts of 10^5 positrons, accumulated for 1.5 s intervals in a buffer gas trap [147, 30] fed by a solid-neon moderated [142] beam of positrons from a $\sim$ 10 mCi ^{22}Na source, are implanted at 1.5 keV into a single-crystal Cu(110) target [see Fig. 5.2 (d)], held at a temperature of 950 K [129]. Ps emitted from the target is excited to n = 32 Rydberg states, as in Ref. [98]. The UV and IR laser beams are directed approximately parallel to the sample surface and near perpendicular to the detected Ps flight trajectories [98] to minimize first-order Doppler shifts as illlustrated in Fig. 5.2.

The time of flight (TOF) spectra for n = 32 Ps traveling from the Cu(110) target to the MCP detector are plotted in Fig. 5.3 for mirror potentials of 95 and 10 V ("mirror on") and 0 V ("mirror off"). These data illustrate the signal enhancement resulting from turning on the mirror potentials. A large excess of counts due to the mirror is evident for Ps flight times t in the range of 10 to 60 μs. For t<20 μs the Ps emission is primarily due to spontaneous emission [101, 130], while the remaining portion is due to thermal emission

[129, 122]. The Ps atoms produced through spontaneous emission, which have kinetic energies up to ~ 1.8 eV, are only efficiently reflected by the mirror with absolute potentials in excess of ~ 20 V, as seen in the contrast of the two mirror on data sets at flight times t<20 μs. The peak in the signal at ~ 15 μs also has a large contribution from UV induced background [100]. At long flight times the apparent mirror on-off ratio diminishes, which may result from a combination of effects. Interaction with background thermal radiation [127, 71] may excite transitions that randomize the k state [170], thus approximately halving the probability of reflecting. Similarly, spontaneous radiative decay may affect the k state, or simply reduce the observed signal [59]. For flight times greater than 80 μs, the observed signal rate of 2×10^{-5} counts per shot per μs, appears to be a uniform background signal.

5.5 Performance of Rydberg Mirror

A fit to the data over the Lyman-α resonance (Fig. 5.6) indicates that the mirror increases the count rate by a factor of 6.96±1.17. To maximize the signal rate, the IR wavelength is set to slightly above the Stark fan center, ensuring that the Ps is excited to states of k>0 with maximum possible efficiency.

A direct illustration of the focusing effect of the mirror is shown in Fig. 5.4 (a) and (b), which give the two-dimensional distributions of events detected by the MCP with the mirror potentials off (a) and on (b) for n = 32 Ps. Although not shown, similar results have also been obtained for n = 38 Ps. The data for these measurements are averaged over UV wavelengths between 242.995 and 243.065 nm and TOFs between 20 and 100 μs. We note that this range is not centered precisely about the 1S-2P resonance. A 0.01 nm shift

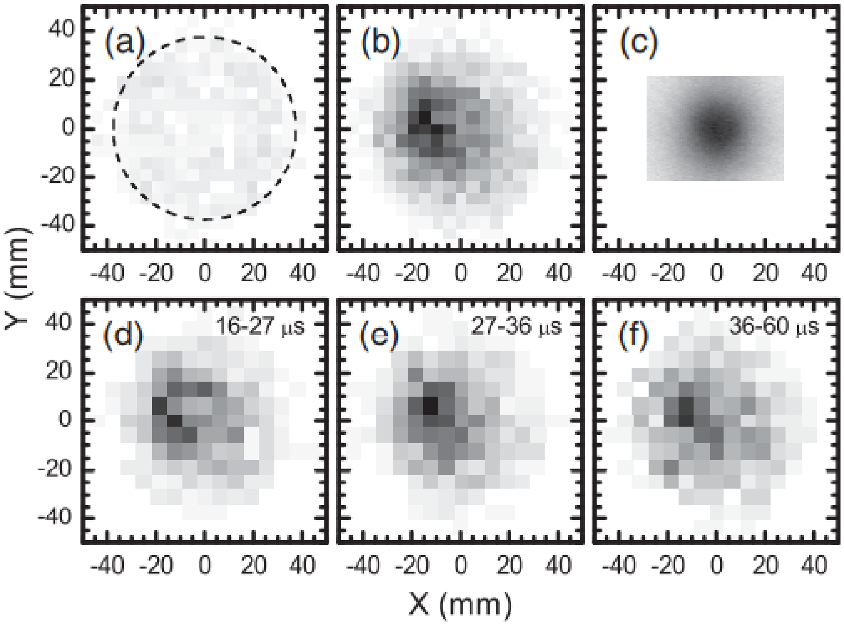

Figure 5.4: Rydberg (n=32) position data with (a) 0 V and (b) ±10 V applied. Best focus showm in (c). (d)-(f) are velocity (time of flight) subsets taken from be (b) with (d) 16-27 μs (e) 27-36 μs and (f) 36-80 μs

is observed, which is likely due to a misalignment of the laser with respect to the mean of the Ps trajectories of 1.6° from perpendicular. To determine the focal width of the spot, the data of Fig. 5.4 (b) and (c) and the image of the white light LED source have been binned as a function of radial distance r from the focus center divided by r, to produce the averaged radial distributions plotted in 5.5 The Gaussian fit to the Ps data indicates that the spot has a width of 32.2±0.9 mm FWHM. For comparison, the best optical focus, shown in Fig. 5.4 (c) and Fig. 5.5 (a) has a Gaussian component with a FWHM of 21±3 mm. The additional broadening observed with Ps is primarily attributed to the small offsets of the mirror (-11 cm) and detector (+14 cm) from their ideal relative axial positions, which simulation suggests should produce a $\sim$ 10 mm diameter ring image at the detector.

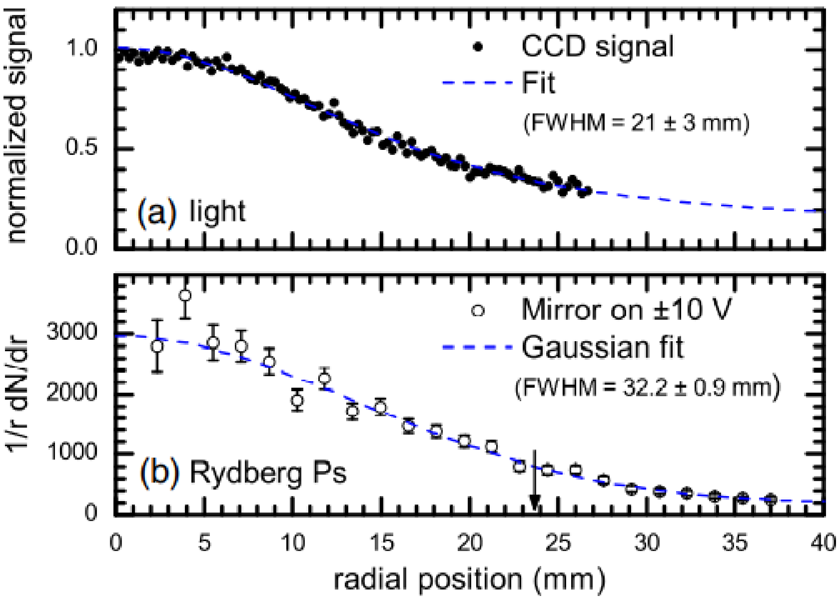

Figure 5.5: Rydberg mirror radial distribution of focal spots by (a) light, and (b) Ps data from Fig. 5.4 (b) (20-80 μs)

The maximum possible ratio of count rates for mirror on versus off would be one plus the ratio of solid angles of the mirror and the MCP detector (18.7:1), yielding an upper limit of $\sim$ 19.7 here. The observed effect is smaller than this principally due to the inefficiency of the production of focusable Rydberg states in our experiment, owing to the relatively broad bandwidth of the IR laser ($\sim$ 55 GHz) and the motionally induced Stark shift of Ps in the target chamber. Simulation suggests that the peak production efficiency is $\sim$ 35%, yielding a predicted signal ratio of 7.5:1, in good agreement with the observed effect of $(7.0 \pm 1.2) : 1$.

5.5.1 Effects due to preparation of Rydberg positronium

The signal enhancement is defined here as the ratio of the signals observed with the mirror potentials on and off. The maximum ratio is achieved when the focal spot is

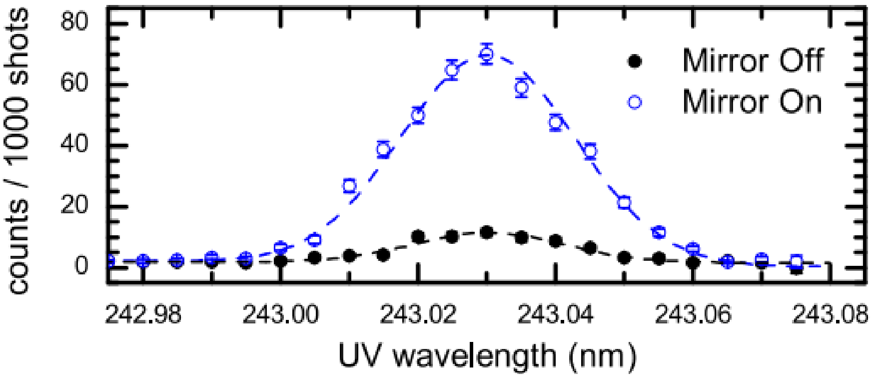

Figure 5.6: Observed Ps signal scanned over 1^3S-2^3P transition with and without mirror

encompassed within the active area of the detector, and all atoms incident on the mirror are reflected. The maximum enhancement can thus be calculated from the ratio of the solid angles of the mirror and of the detector with respect to the Ps source, yielding an upper limit of 19.7:1.

5.5.2 Doppler narrowing of the spatial distribution of Rydberg Ps

As a result of the first-order Doppler shift, the bandwidths of the two lasers used to produce Rydberg Ps have corresponding Ps angular distributions in terms of the excitation probability. For a transition to an isolated state, a narrow bandwidth would allow excitation to occur only for a small angular range θ, where θ is defined as the angle between the trajectory of the laser and the target normal vector. Neglecting the second-order Doppler effect, there is no dependence on the azimuthal angle ϕ. In our experiment, the lasers are aligned, to a good approximation, in the horizontal plane. This implies that the trajectories of the Rydberg Ps atoms produced would correspond to a vertically oriented wedge.

As the bandwidth of the IR laser is substantially broader than that of the UV, and given the breadth of the Stark-split manifold of Rydberg levels, which increases the angular range accessible to the IR laser, we consider here only the limiting case provided by the UV laser. In our experiment, the wavelength of the UV laser was scanned across a range centered about the 1^3S-2^3P transition. In Fig. 5.6 results are plotted illustrating the signal enhancement resulting from operation of the mirror with potentials of ± 10 V, where the best focus was observed. Gaussian fits to the two data sets indicate a mean UV bandwidth of 137 ± 4 GHz, far greater than the ~ 35 GHz measured with a SPEX 1700 II spectrometer. The most significant contribution to the observed width of the transition resonance is a result of the uncertainty in the shot-to-shot wavelength measurements, made with a Bristol 820 WM wavemeter. The precision of the wavemeter for measuring the line center of a laser with a bandwidth exceeding 15 GHz is ± 0.01 nm, corresponding to a 100 GHz broadening and accounting for the majority of the observed width. It is important to note that this is purely a result of the imprecision in determining the mean wavelength, meaning that the spectrum presented in Fig. 5.6 is artificially broadened.

We model here the anticipated behavior via a Monte Carlo simulation. Assuming reflection of every atom incident upon the mirror, we determine the effective signal enhancement factor as a function of the UV laser bandwidth. Consider a typical Ps atom, with a thermal velocity of 1.5×10^5 m/s. The mean angular range of Ps trajectories incident on the mirror is $\sim 1.9^\circ$, which yields a Doppler shift of one part in 1.7×10^{-5} of the excitation wavelength, or a shift of ± 21 GHz (*i.e.*, 42 GHz FWHM). The bandwidth of the UV laser is ~ 35 GHz, though the effective bandwidth is additionally broadened by the 10 GHz split-

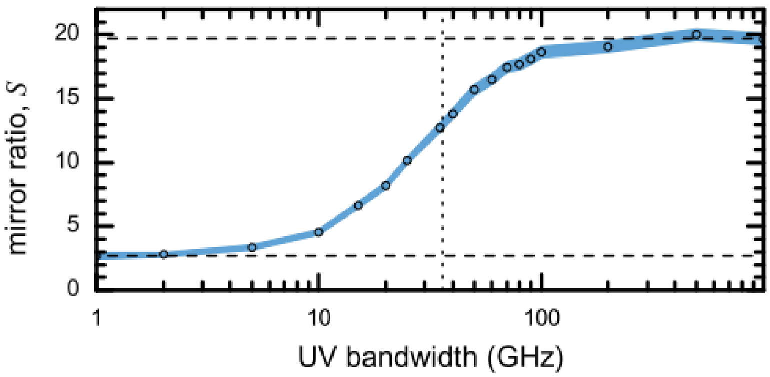

Figure 5.7: Dependence of the signal enhancement due to reflection from the focusing mirror as a function of the UV laser bandwidth

ting of the 2^3P states [73], to give a total width of ∼ 36 GHz. As the mean angular range of the mirror corresponds to a similar frequency bandwidth as the UV laser, it is important to consider the problem in greater detail. In the simulation we have assumed that the peak laser intensity corresponds to an excitation probability of one. In the experiment, the pulsed UV laser energy was between 100 and 500 μJ, in a beam spot of ∼ 2 mm diameter with pulses lasting 3 ns, at or above that necessary to begin saturating the transition [33], which will further broaden the apparent bandwidth [50], though quantifying the magnitude of this effect is presently not possible.

Simulated results are plotted in Fig. 5.7 indicating the expected ratio of signal in measurements made with the mirror on and off. The minimum signal ratio can be calculated from a ratio of the angles of trajectories reaching the edge of the detector (θ_1), and trajectories intersecting the near and far edges of the mirror (θ_2 and θ_3, respectively) such that $S_{min} = 1 + \frac{\theta_3 - \theta_2}{\theta_1} = 2.72$, while the maximum is defined by the ratio of the cross sectional coverage of the detector and mirror given by the ratio of the radii of the circles defined by atom trajectories through a planar x, y cut that intersects the mirror

($r_3 \leq r \leq r_2$) and detector ($0 \leq r \leq r_1$), where $S_{max} \approx 1 + \frac{r_3^2 - r_2^2}{r_1^2} = 19.71$. The simulation suggests that in our experiments a UV bandwidth of 36 GHz will yield a ratio S = 13:1.

5.5.3 Production of positronium atoms in focusable states

The bandwidth of the IR laser and the overlapping of neighboring resonances at modest electric fields presently make it difficult to produce Ps atoms in a small range of preferred states. Our mirror can only reflect Rydberg atoms if they are in a state with a sufficiently high ionization threshold and have a Stark shift of appropriate magnitude to fully retard the energy component of the incident atom normal to the mirror surface. Due to the short range nature of the electric field, the Rydberg atoms spend only a short period of time in the region of highest field during reflection. We work here on the assumption of a threshold rate $\Gamma = 10^8$ s^{-1}, assuming a characteristic reflection time of $\sim$ 10 ns. However, even assuming a longer duration reflection, due to the exponential dependence of a state's ionization rate with respect to electric field magnitude, the maximum kinetic energy that can be reflected is not substantially changed.

As previously noted, Rydberg Ps in our experiment is produced by two single-photon excitations. Preparation of Rydberg states occurs $\sim$ 1–2 mm in front of the target surface, in a magnetic field of 7.5 mT. Trajectories of detected atoms are oriented at $45 \pm 2.5^\circ$ of the magnetic field. Given a thermal spread of Ps velocities, this yields a mean motionally induced electric field of 800 ± 700 V/m as shown in Fig. 5.8 (a). The selection of Rydberg states accessible depends on the overlap of the Stark-split manifolds in the electric field experienced by each atom, and the bandwidth of the IR laser, illustrated in Fig. 5.8 (b).

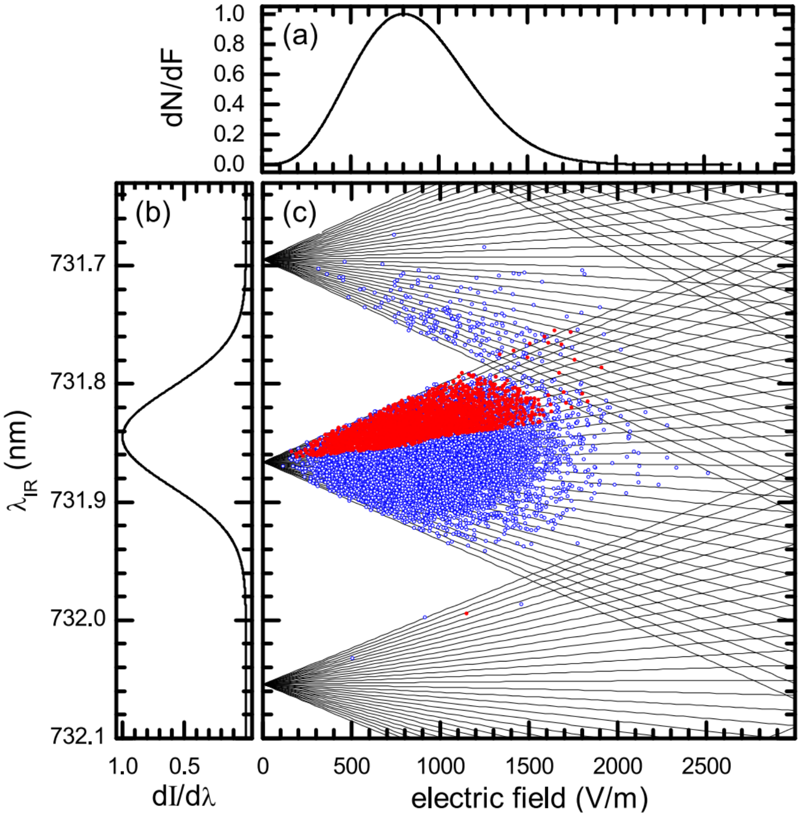

Figure 5.8: Simulated production of excited Rydberg Ps and reflect-ability

In Fig. 5.8 (c) the Stark fans of Rydberg Ps levels of $|m| = 1$ and n = 31, 32, and 33 are shown. The results of a simulation are shown for the relative populations of the available k states. The excitation probability for transitions from 23P to Rydberg levels is treated as proportional to the laser power with the probability normalized to the portion of the intensity that can excite atoms to a nearby state, *i.e.*, a state within ±1/2 of the level splitting. Atoms can only be reflected from the mirror if their angle has them incident with the mirror surface, the component of their kinetic energy radial to the mirror is less than that set by an ionization rate of $\leq 10^8$ s^{-1} (unique to the Rydberg state excited), and the electric field required for reflection is ≤25 kV/m, the maximum field generated with potentials of ±10 V applied. The simulation predicts a maximum in the signal ratio of ∼ 9.2:1. Taking this result in combination with that of the preceding simulation, we predict a mirror ratio S = 6.1:1, in close agreement with the measured ratio S = 7 ± 1:1.

5.6 Effects of Geometry of the Apparatus

5.6.1 Focusing expected with an ideal mirror

The focal length of the mirror was found by placing a small (∼ 3 mm diameter) LED light source at a distance of 3.00 ± 0.01 m from the center of the mirror and adjusting the position of the objective lens of a digital camera to find the optimal focal spot. This test yielded a measure of both the optimal resolution and focal distance. As the focal image produced with light results from the reflection of light from each of the cylindrical wires, the observed focal image is composed of a sum of overlapping circular arcs, which yields a distribution with an intensity that varies approximately as 1/r, broadened by a

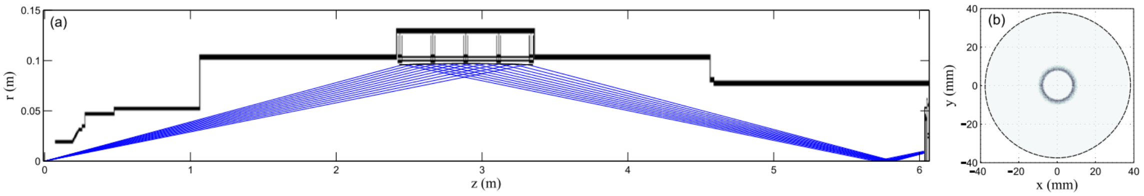

Figure 5.9: Simulated results of the expected focusing behavior of the mirror apparatus as constructed

Gaussian with a width of 21±3 mm FWHM. The optimal focus was obtained with the camera positioned at a distance of 2.95±0.05 m from the mirror center.

In the apparatus of Fig. 5.9 the net length of the Ps flight path, 6.03 ± 0.01 m, was close to the optimal 6.0 m desired, but the available hardware did not allow for the positioning of the mirror in the center of the Ps trajectory. For the experiments reported, the center of the mirror lay 2.89 ± 0.01 m from the source and 3.14 ± 0.01 m from the ionizing grid of the detector (where the image is effectively formed). To estimate the expected focal image we expect to observe from a point source, a simple Monte Carlo simulation was employed treating the mirror as a hard ellipsoidal surface and assuming the specular reflection of incident Ps atoms, *i.e.*, no wires were included in this simulation. In Fig. 5.9 (a), example trajectories are shown for uniform angular increments. In Fig. 5.9 (b) a histogram of counts for many such trajectories illustrates the resulting image, as seen at the position of the detector. As the mirror is positioned too close to the Ps emitting source, the focus occurs ∼ 26 cm in front of the detector. The image at the detector is a two-dimensional projection of the mirror surface, an annulus of 17.0 ± 0.1 mm radius, with a FWHM width of ∼ 1.5 mm, comparable to the 1 mm diameter assumed for the source in the simulation. In practice, the observed image with Rydberg Ps in reference [102] is a Gaussian spot of

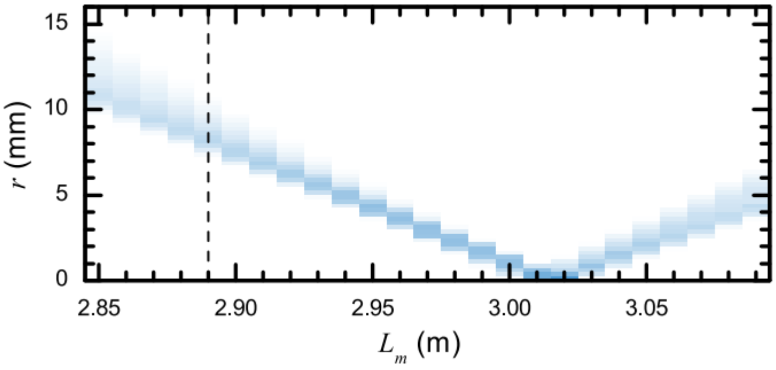

Figure 5.10: Ideal simulated radial distributions are illustrated as a function of the source to mirror center distance

32 ± 1 mm FWHM, which is consistent with the predicted feature, after accounting for Gaussian broadening expected due to the imperfection of the mirror wires (and thus, the electric field produced) and the finite resolution of the position sensitive detector ($\sim$ 2 mm FWHM for charged particle detection).

The best focus that could be achieved in the simulations with the ideal mirror of Fig. 5.9 while maintaining a fixed distance of 6.03 m between the source and detector is found with the mirror center 3.015 m from the source, yielding a FWHM diameter of $\sim$ 1.1 mm, comparable to the 1 mm diameter source size, as illustrated in Fig. 5.10.

5.6.2 Dependence of the focal length on applied mirroring potentials

The mirror has been described as nearly achromatic, owing to the short range of the electric field produced. However, we know that Ps atoms with different radial velocities will be reflected at different depths; more energetic atoms will penetrate closer to the wires, to regions of higher electric field, before reflection. To estimate this contribution to the resolution of the observed focal spot we apply a simple model for Rydberg Ps reflection in a Monte Carlo simulation, allowing Ps atoms to reflect from an ellipsoidal surface that mimics the physical structure and location of the mirror in our apparatus. To adjust the reflection radius, this surface is moved uniformly closer to the axis in small steps. Reducing the radius of the mirror in 1 mm increments is found to correspond to 0.120 ± 0.004 mm changes in the diameter of the focal spot. Assuming a thermal distribution of Ps from a 1000 K target, the mean radial energies of Ps atoms incident on the mirror are $\sim 0.2 \pm 0.15$ meV. Using an electric field calculated from a flat infinite series of wires with ±10 V applied potentials (the settings that produced the best focus in our experiments), reflection of atoms occurs at radial separation from the mirror of $\sim 2.1 \pm 0.6$ mm, and this range of reflection depths results in a 0.24 mm FWHM attributed to the thermal spread of Ps velocities.

5.7 Effects caused by the-ideality of the electric field

The principle behind the electrostatic mirror is that a surface with a potential that varies sinusoidally along one axis produces an electric field, the magnitude of which decays exponentially in the direction of the surface normal vector. In our experiment, the sinusoidally varying potential is approximated by a series of equally spaced wires with alternating equal and opposite potentials applied. To explore what impact this approximation has on the performance of the mirror we calculate the electric field and study the trajectories of reflected Rydberg Ps atoms via Monte Carlo simulations.

The deviation of the applied potential from sinusoidal results in higher order terms in the electric field that are expected to decay more rapidly than the primary term. How-

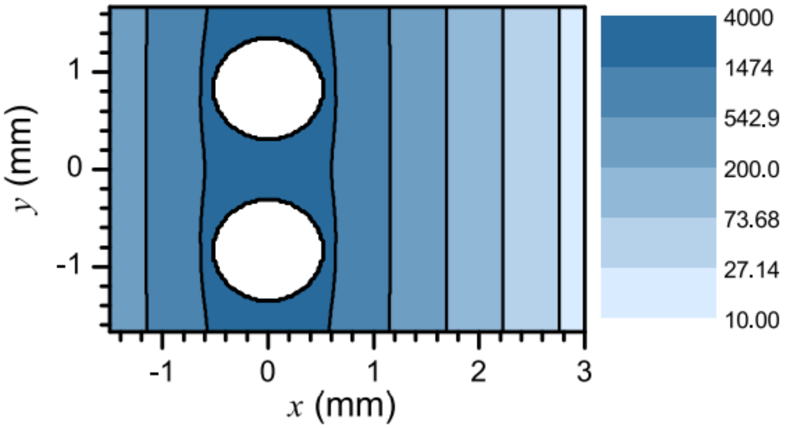

Figure 5.11: Contour plot of the electric field for an infinite array of wires, defined with comparable size and spacing to those of the physical mirror constructed.

ever, at short distances these terms can contribute significantly to the reflecting field, and more importantly can result in a non-zero field gradient along θ (in the case of cylindrical symmetry).

The electric field for the particle simulation is found by the iterative relaxation method and is plotted in Fig. 5.11. A flat mirror surface is approximated in two dimensions as an infinite linear array of wires, with size and spacing chosen to closely approximate the actual geometry of the apparatus. Having calculated the electric field due to the wires in the x, y plane, we calculate the potential energy U of a Rydberg atom from 5.2.

The force f on an atom at some position x, y in the electric field is found from the gradient of the potential energy, that is $f(x, y) = -\nabla U(x, y) = m\vec{a}$ and is used to calculate the acceleration a on atoms in a simulation Using the calculated electric field (shown in Fig. 5.12), we model the trajectories of Rydberg Ps atoms in the state n = 32, $|m| = 0$ and k = 31, the most readily deflected state produced in our experiments. In Fig. 5.13 the

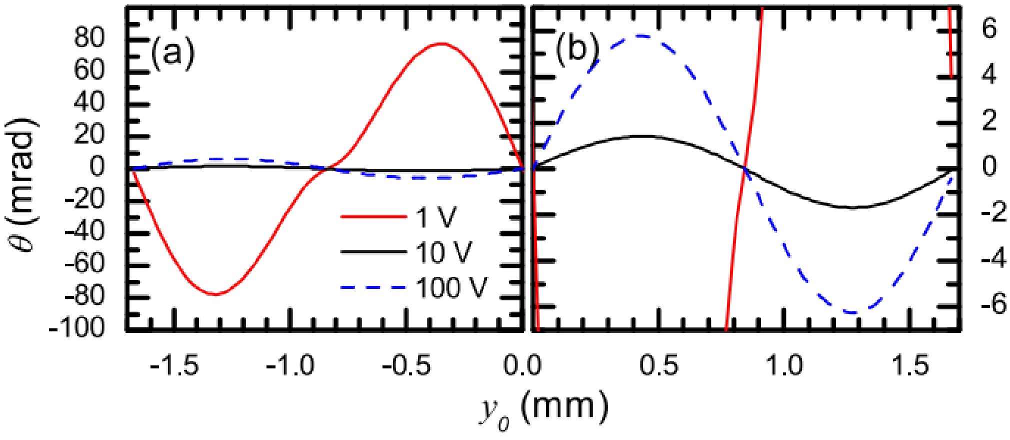

Figure 5.12: Reflection angle θ for Ps atoms in state n = 32, k = 31 from the electric field of an alternating potential wire array as function of the incident position y_0 ($y_0 = 0 is center shown in 5.11$) relative to the wire array, for applied potentials of ±1, ±10 and ±100 V

angular deflection is plotted as a function of the y-intercept of incident atoms. It is clear from the observed distributions that the angular deflection is most severe at low voltages, where the Ps atoms are stopped close to the wires and the deviation from an ideal field is most significant. At 100 V the effect is suppressed by a factor of two compared to result for ±10 V. In our experiment however the improvements expected due to an increased mirror voltage are not evident due to the additional defocusing resulting from the non-ideal location of the mirror.

In Fig. 5.13 the spectrum of angular deflection for a T = 950 K thermal distribution of Ps resulting from reflection of atoms of all states k > 0 is plotted, along with the cumulative distribution function of the angular distribution. The relative population of k states and corresponding velocity distributions, which gradually shift as a function of k from the initial thermal distribution due to the motionally induced Stark splitting where the excitation takes place, is taken from the simulation presented in 5.8 and discussed pre-

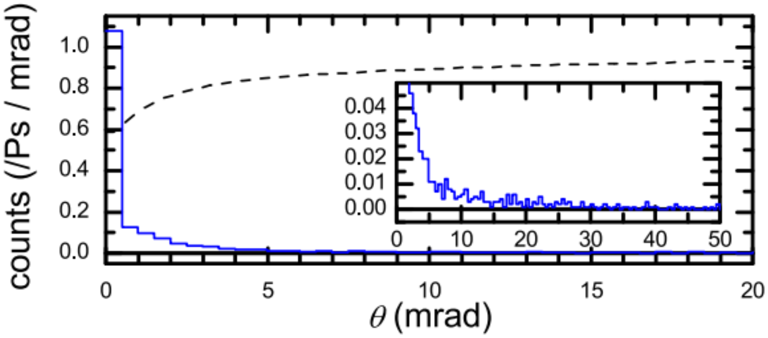

Figure 5.13: Reflection angle θ from the electric field of an alternating potential wire array calculated for a thermal distribution of positronium, with individually calculated k state populations and corresponding velocities to best match the conditions of the experiment.

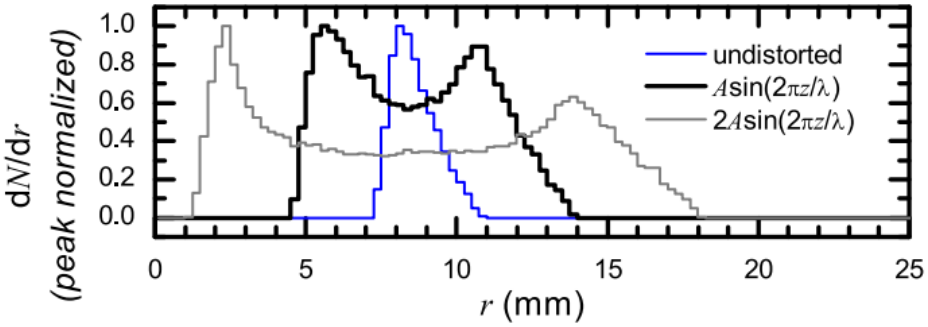

Figure 5.14: Simulated radial distributions of focused Ps at the detector for perfect wires, and wires with a superimposed sinusoidal variance (A = 12.5 μm) in the radius.

viously. As the mirror constructed has wires set at one degree increments, the few mrad deflections of the linear wire array simulation provide a reasonable approximation and can be used to estimate the angular broadening expected in the experiment as a result of the deviation of the electric field from ideal. The results of simulations with a realistic Ps velocity distribution and k-state distribution predict that more than half of the atoms are reflected at angles of <1 mrad, which over a 10.9 cm trajectory, the radial distance traveled by reflected Ps atoms before reaching the detector results in a deflection of up to ±0.11 mm, contributing no more than $\sim$ 0.22 mm FWHM to the focal spot.

5.8 Effects due to imperfections of wires used

The mirror wires have a quoted diameter of 1 ±0.025 mm. The wires are not perfectly straight and there is a helical distortion, with peak-to-peak variations on the order of $\sim$ 10–20 μm and longitudinal period of about 0.15 m. In Fig. 5.14 simulated radial distributions are shown for the projected focal image at the detector, using the model discussed in Section 5.6, and then superimposing a sinusoidal variation with amplitude A = 12.5 μm and 2A = 25 μm, both with a periodicity λ of 0.15 m. In both cases, the radial distribution is substantially broadened, with the peak of the distribution seemingly split about the mean of the undistorted wires simulated distribution. Assuming the lesser amplitude variation, the FWHM broadening resulting from this effect is on the order of 10 mm.

A similar effect is expected due to the gravitational sagging of the wires between the support rings, leading to a bowing of comparable magnitude. This effect does not share the same symmetry however, primarily distorting the lens shape along the y-axis. This should lead to a similar distortion in the observed focal image. Both of these effects taken together, using conservative estimates of the magnitude of the distortions, can readily account for the observed width of the focal spot in the optical measurements.

5.9 Rydberg Mirror Conclusion

We have explored in detail the use and limits of an electrostatic mirror developed to image a point source of Rydberg atoms. We have identified effects in our experiment that limited both the observed ratio of signal enhancement S, and the resolution of the focal spot, which we summarize as follows:

The reduction of S relative to the geometrically defined maximum was explained by a detailed analysis of effects related to the production of Rydberg Ps. On one hand, the UV laser bandwidth limits the Doppler spread accessible and results in only partial illumination of the mirror. On the other hand, the relatively broad bandwidth of the IR laser, relative to the spacing of the Stark-split levels in the motionally-induced electric field in the target chamber, means that production of focusable states of Ps is not 100% efficient. Simulations of these two effects predict $S = 0.66{\times}S_{max}$ and $S = 0.47{\times}S_{max}$, taken together we thus expect a signal enhancement of $S \approx 6.1{:}1$, in good agreement with the observed ratio of $(7 \pm 1){:}1$. The observed focal resolution is a result of many contributing factors: One large contribution arises due to the non-ideal placement of the mirror, relative to the source and detector, resulting in an image of a 17 mm diameter ring at the detector. This is further broadened by the 21 mm Gaussian FWHM of the best focus achieved with the mirror focusing light. This limit is a product of two effects of comparable magnitude. The first is a roughly periodic variation in the wire radius of ~ 25 μm with a period of ~ 15 cm that appears to be a result from the wire manufacturing process. This variation results in a contribution to the resolution of the mirror on the order of 10 mm FWHM. A second contribution of comparable magnitude results from the sagging of the wires under gravity. Due to the spacing of the wire supports, this has a similar periodicity and magnitude of displacement, and is anticipated to produce a similar broadening, though being an asymmetric distortion, is likely to contribute more substantially to the broadening of the focus along the y-axis. These two deviations of the wires from their intended radial positions taken together are sufficient to explain the observed optical focus. Finally, there are lesser contributions from the spatial resolution of the detector ($\leq$4 mm FWHM), the deviation of the electric field from ideal (about 1-2 mm FWHM), and the finite spot size of the Ps source ($\sim$ 1 mm FWHM). There are also many other effects that contribute to the focal resolution, *e.g.*, the influence of stray electric fields [28] and interactions of Rydberg atoms with blackbody radiation [71] in flight. These effects have not been studied in detail since simple estimates indicate they are orders of magnitude less significant under the experimental conditions discussed here.

Finally, to improve the practical efficiency of the mirror, it would be ideal to selectively prepare the Rydberg Ps in states of maximal k. This could be achieved by applying an electric field close to the Inglis-Teller limit ($\sim$ 1 kV/m for n = 32) at the target [177] to maximally split the states and utilize a narrow bandwidth IR laser for the final excitation. Under these circumstances, the IR laser bandwidth would likely limit the angular distribution of excited Ps, although a colder source of Ps, desirable for a measurement of the gravitational deflection of Ps [140], could mitigate this drawback. A more ideal mirror for very slow Rydberg Ps atoms in a back-reflection geometry could be achieved by modifying a large ($\sim$ 1 m) telescope mirror, which is optically far superior to the mirror described here, by cutting linear grooves into and metallizing the surface to create isolated vertically aligned electrode elements. Starting with a telescope quality optical mirror and reducing the focus of the positron beam at the target, the limiting factors to the focal resolution would likely be the non-ideal electric field (although, having vertically aligned electrodes will ensure that the angular scatter upon reflection due to the non-ideal electric field will primarily broaden the horizontal focus). For a gravity measurement involving flight times in the range of 1-10 ms, factors such as the interaction of Rydberg atoms with blackbody radiation or stray electric fields while in flight may become important. Blackbody radiation interactions can be greatly suppressed by cooling the apparatus to <50 K. The influence of stray electric fields can be reduced by applying a small DC bias field [137], which can be regularly inverted. Taking the difference between the two sets of measurements would effectively cancel out the influence of stray fields, provided they remain suitably static.

Chapter 6

Detector for Positronium Temperature Measurements by Two-Photon Angular Correlation

The information in the following is taken from previous published materials [43].

6.1 Introduction

To realize the goal of producing, identifying, and studying a positronium (Ps) Bose-Einstein condensate (BEC) [152] we will need to produce a dense, cold, spin polarized source of Ps. For a 2D BEC of Ps at areal density $n_{2D} = 10^{12}$ cm^{-2}, or a 3D BEC at density $n_{3D} = 10^{18}$ cm^{-3}, the critical temperature for condensation is $T_c \sim 15$ K [111, 10].

To accomplish this, pulses of $\sim 10^8$ positrons from an accumulator [168], compressed by a rotating electric field [3, 84] at $\sim$ 50 MHz (to a plasma $\lesssim 1$ mm in diameter) will be accelerated and temporally bunched [135] to $\sim$ 10 ns FWHM, and then extracted from the accumulator through a small aperture in a μ-metal shield [79, 166]. The beam will then be electrostatically focused to a radius of < 0.1 mm onto a transmission re-moderator [158]. After about 15% of the positrons emerge from the re-moderator foil with low energy, they will be accelerated and electrostatically focused again, a process known as brightness enhancement [134], to a $\sim$ 10 μm diameter spot at the target where they become trapped within a cavity $\sim$ 10 μm in diameter and 10 $\sim$ 100 nm deep. The final areal density at the target will be 2×10^{13} cm^{-2}, about 100 times greater than previously achieved [39].

Once implanted in the target, up to 50% of the positrons may be expected to form Ps at cryogenic temperatures [72, 141]. Roughly one-quarter of the Ps atoms formed are in the $1^1\mathrm{S}_0$ state and are rapidly ($\tau = 125$ ps) lost to annihilation. The remaining three-quarters form 1^3S_1 with a vacuum lifetime of 142 ns. The high-density of Ps expected in the cavity will lead to spin-exchange quenching [29] and di-positronium formation [40], reducing the amount of triplet Ps until these processes are exhausted, leaving pure m=1 triplet Ps [39]. The combination of processes leading to rapid annihilation means that the delayed signal that we hope to observe will come in addition to a substantial prompt background of 511 keV γs, however, the prompt signal will rapidly decay so that after $\sim$ 40 ns, we will be able to unambiguously detect coincident annihilation γs from long lived triplet Ps quenched [179] by a delayed 10 ns 1 Tesla pulsed magnetic field transverse to the polarization direction of the triplet Ps.

As the Ps will be confined within a cavity, probing the temperature of the atoms cannot be trivially achieved via spectroscopic techniques (*e.g.*, measuring the Doppler width of the $1S-2P$ transition of Ps emitted from the target into vacuum [32]), and Doppler spectroscopy of Ps within a cavity is further complicated by saturation and line-narrowing [64]. Rather, the Ps temperature will be measured using the Angular Correlation of Annihilation Radiation (ACAR) [164, 14] method to measure the momentum of Ps atoms at the instant of annihilation. Accounting for the non-zero momentum of a Ps atom at the time of annihilation, the annihilation photons with momenta $\vec{p}_1$ and $\vec{p}_2$ deviate from collinearity by the angle $\theta \approx \frac{p_{Ps\perp}}{m_e c}$ where $p_{Ps\perp}$ is the magnitude of the Ps momentum component perpendicular to the line joining the difference of the momenta of the nearly collinear photons.

For Ps cooled to 10 K, the FWHM of the angular distribution is ~ 0.14 mrad so the angular resolution of the apparatus needs to be about 0.1 mrad. In this paper, we describe the construction and testing of a modular detector assembly, which will form the basis of the detector arrays necessary for the planned experiment. In Section 6.2 we present the design and construction of the assembled detector and characterize the cross-talk between neighboring channels. In Section 6.6 we present details of a data analysis routine and the optimization and characterization of its performance. Preliminary data collected with a one-quarter scale version of the final experimental arrangement is presented in Section 6.7.

6.2 Design and characterization of the detector assembly

The planned experiment will involve two detector arrays separated by 20 m, positioned diametrically opposite and equidistant from the target chamber. Each array contains 192 $30 \times 22 \times 2$ mm^3 lutetium-yttrium oxyorthosilicate doped with 0.05% Cerium ($Lu_{1.8}Y_{0.2}SiO_5$:Ce (LYSO:Ce, hereafter "LYSO" for short)) scintillator channels. We anticipate one delayed detected 2γ annihilation event per 7.4×10^4 singlet Ps atoms annihilating immediately at the target. For pulses of $\sim 10^7$ positrons, this would result in a prompt signal of $\sim$1 single γ per shot per channel. In developing the detector, we reviewed several possible candidate scintillators: lead tungstate ($PbWO_4$), LYSO purchased from Shanghai Project Electronic Technology Company, and thallium-doped sodium iodide (NaI(Tl)), as well as a plastic scintillator (EJ-230) purchased from Eljen Technology. In the following discussion we describe the characteristics of several different scintillators in various configurations, and describe the final assembly produced.

6.3 Testing of Scintillators and Mounting Arrangements

To test and characterize a modular detector, it is first positioned ~ 5 cm away from a 13 μCi ^{22}Na positron source. Pulse waveforms from the test assembly are recorded when detected in coincidence ($\Delta t \leq$20 ns) with the unambiguous observation of a 1.27 MeV γ in a NaI(Tl) based detector oriented perpendicular to the test assembly. The combination of a weak source and detection coincident with the birth of a positron, greatly reduces the observed background resulting from cosmic radiation and scintillator self-signal (as seen in LYSO). We average over $\sim 10^3$ waveform records to generate composite pulses with high signal-to-noise ratios, allowing a precise comparison of the performance of each test system. An example illustrating three such measurements comparing a variety of LYSO arrangements is plotted in Fig. 6.1.

Each scintillator tested was approximately three absorption lengths long, yielding a $\sim 95\%$ chance of interaction for 511 keV γs entering the scintillator along its longest axis.

Table 6.1: Rise and Decay times measured from data contributing to the photopeak presented in Fig. 6.2. Data given without error estimates is from Ref. [156]. Rise-times indicate the average time elapsed for a pulse to rise from 12% to 88% of the maximum amplitude. The NaI(Tl) scintillator was mounted to a Hamamatsu R1924A PMT, while the other scintillators were coupled to a Hamamatsu H12700B PMT. We list here fundamental properties of the scintillators pertinent to the optimization of the detector: Light output in photons per keV, attenuation length (λ), and relative refractive index (n_r) [156, 7, 70]. n_r is the ratio of the scintillator's index of refraction relative to that of the borosilicate window of the PMT ($n_b \sim 1.53$).

scintillator	rise time (ns)	decay time (ns)	photons per keV	λ (cm)	$n_r = \frac{n}{n_b}$
LYSO:Ce	2.90 ± 0.01	46.3 ± 0.11	32	1.1	1.2
$PbWO_4$	1.10 ± 0.03	6.35 ± 0.03	0.5	1.4	1.46
EJ-230	0.94 ± 0.02	3.49 ± 0.12	2	10	0.66
NaI(Tl)	5.91 ± 0.21	250	38	2.5	1.23

For the inorganic scintillators LYSO and $PbWO_4$, which have 511 keV attenuation lengths of ~ 1 cm, the scintillators measured $30 \times 22 \times 2$ mm^3. The plastic scintillators, with an attenuation length of ~ 10 cm, measured $300 \times 22 \times 2$ mm^3. Scintillators were coupled to a Hamamatsu H12700B 64 anode photomultiplier tube (PMT) for testing.

The energy deposited from a γ-ray can be inferred from the resulting pulse area, calibrated from the measured pulse area spectrum as indicated in Fig. 6.2. To make a fast and accurate estimate of the energy of a given γ detection, pulses are fit with a simple function with characteristic rise and decay times which are derived from the composite pulses, as illustrated in Fig. 6.1. Fig. 6.1 lists a summary of the fitted rise and decay times of the different scintillators materials tested. LYSO was selected for its large light output and moderate rise time, two important qualities for multi-peak detection.

When testing LYSO, it was found that the observed lifetime (~ 46 ns) was longer than the 40 ns reported in the literature [173]. This led us to investigate LYSO response times and energy resolutions for various scintillator geometries. Annihilation energy spectra were generated using two similar Hamamatsu R1924A single channel PMTs each coupled to one of two different sizes of LYSO: a block measuring $30 \times 15 \times 15$ mm^3, and a thin rectangle measuring $30 \times 22 \times 2$ mm^3 coupled to the PMT at the 2×22 mm^2 face. Typical 511 keV pulse areas are averaged and analyzed for signal pulse rise and decay times. Both LYSO samples exhibited similar rise-times, decay times, and energy resolutions, but it was noted that the thin LYSO produces smaller pulses. There are several possible explanations for this. UV light bounces fewer times on average within the block sample leading to higher efficiency as compared to the thin scintillator sample. Also, the block sample covers a greater portion of the center of the PMT's face ensuring that virtually all light incident on the glass face is detected. Energy spectra were recorded with a bare scintillator surrounded by flat black painted isolators, or wrapped in a reflective film. The reflective film, Vikuiti Enhanced Specular Reflector (ESR) [1] purchased from 3M Optical Systems, is a 65μm thick, non-metallic, 100% polymer that has a minimum 98% reflectance across the visible spectrum. The results of these tests are summarized in Table 6.2. Bare thin scintillators exhibited the narrowest rise-time (2.9 ns), but longer decay time (46 ns). Using black surfaces rather than ESR lead to a comparable rise time (3.1 ns) and a shorter decay time (43 ns).

In Fig. 6.2, a typical energy spectrum is plotted with data taken from a $30 \times 20 \times 2$ mm^3 LYSO scintillator. The LYSO is wrapped in ESR film, with no adhesive or coupling (*i.e.*, with an air gap), and then the LYSO crystal is coupled on its 20×2 mm^2 face to a Hamamatsu H12700B 64 anode PMT with Polydimethylsiloxane (PDMS) "glue" [66]. Individual channels are separated by 4 mm thick tungsten isolators. The PMT was biased

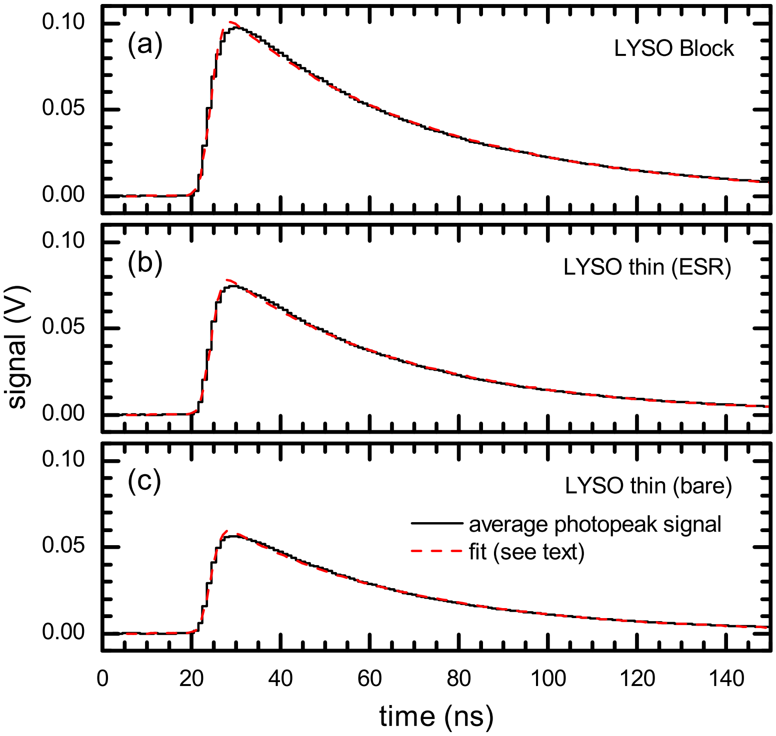

Figure 6.1: Mean photopeak signals (dark circles) along with a fit (red dashed line) from various LYSO:Ce scintillator arrangements coupled to a Hamamatsu R1924A PMT. Fits are a product of an exponential decay and an error function. Pulses presented include: (a) a block of LYSO:Ce ($15 \times 15 \times 30$ mm^3), (b) a sliver of LYSO:Ce wrapped in 99% reflective enhanced spectroscopic reflective tape ($2 \times 22 \times 30$ mm^3), and (c) another similarly sized sliver of LYSO:Ce left bare.

Table 6.2: Tabulated LYSO:Ce characteristics for various geometries and surface coatings. LYSO:Ce blocks and thin rectangles measure $15 \times 15 \times 30$ and $2 \times 22 \times 30$ mm^3 respectively. Data are collected with scintillators mounted on a Hamamatsu R1924A PMT. Data presented here are collected from isolated photopeak signals.

scintillator	rise time (ns)	decay time (ns)	energy resolution
Block			
-bare	3.23 ± 0.02	46.48 ± 0.38	$10.4 \pm 0.1\%$
Thin			
-bare	2.90 ± 0.01	46.30 ± 0.11	$10.0 \pm 0.2\%$
-black cover	3.10 ± 0.02	43.09 ± 0.40	$13.0 \pm 0.3\%$
-ESR film	3.08 ± 0.02	43.36 ± 0.39	$12.1 \pm 0.4\%$

at -900 V for these tests. A peak in the plotted pulse area spectrum at 8 nVs is attributed to full absorption of 511 keV γs, and is known as the photopeak (E_p) or full energy peak. A Gaussian fit to the peak indicates a mean photopeak pulse area of 8.08 ± 0.01 nVs, with a full width at half maximum (FWHM) energy resolution of $\sim 16\%$ ($\Delta E/E_p$). The photopeak area accounts for $\sim 45\%$ of the total counts after correcting for cross-talk. Cross-talk causes the large peak located at $\sim 10\%$ of the photopeak centroid. A typical photo-peak event resulting from a 511 keV γ produces a pulse with a 345 mV amplitude. Assuming the pulse area scales linearly with γ-energy deposited, the Compton edge, which occurs at $E_c = 340$ keV, is found at ~ 5.39 nVs and corresponds to a ~ 230 mV amplitude. There is a nonlinearity in the energy scale relating the observed pulse area and the energy deposited by an incident γ-ray described in Ref. [150]. However, in the energy range from 340 keV to 511 keV, the correction is only $\sim 3\%$ and is neglected here. The plateau below this cutoff is due to Compton scattering of γs within the scintillator while the peak near zero pulse area is attributed to scattered light from neighboring scintillators.

6.4 Detector Assembly

Each of the final detector assemblies comprises an array of 16 LYSO scintillators ($30 \times 22 \times 2$ mm^3), arranged in 2 rows of 8. Scintillators are coupled to the PMT [18] window along one 22×2 mm^2 face with a thin layer of PDMS (poly-dimethyl siloxane) "glue"; all of the remaining scintillator faces are covered in ESR film, a 3M$^{\text{TM}}$ Enhanced Specular Reflector non-metallic mirror film, to maximize the scintillation light reaching the PMT. The layout of one such detector is illustrated in Fig. 6.3. Neighboring rows of 8 scintillators

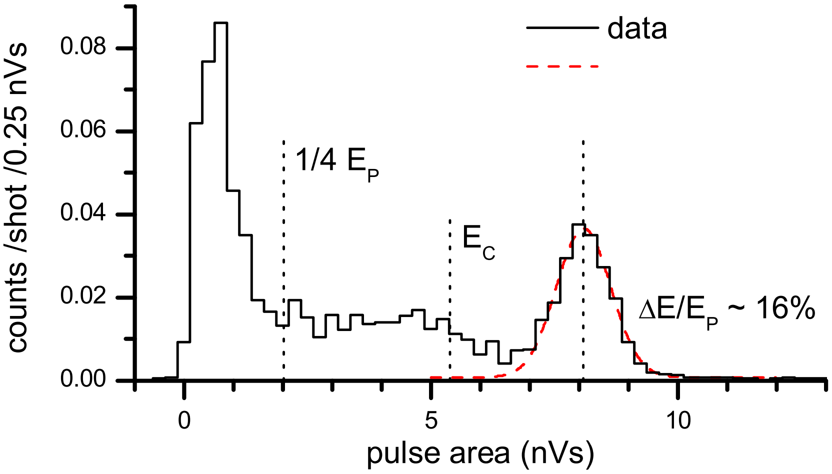

Figure 6.2: Distribution of pulse areas from a $30 \times 20 \times 2$ mm^3 LYSO:Ce scintillator. The LYSO:Ce sample is covered in ESR film on its sides and coupled on its 20×2 mm^2 face to a Hamamatsu H12700B PMT biased at -900 V. The largest peak, seen at low pulse area, is a consequence of cross-talk between neighboring channels. We set a discriminating limit for genuine data equivalent to 1/4 $\mathrm{E_p}$. The plateau between the two peaks is attributed to Compton scattering within a scintillator with the Compton edge $\mathrm{E}_c = (2/3)\ \mathrm{E_p}$. The peak at 8 nVs results from full absorption of 511 keV γs and has a resolution $\Delta\mathrm{E}/\mathrm{E_p}$ of $\sim$ 16% FWHM.

are separated by gamma-ray absorbing pure tungsten plates measuring $30 \times 48 \times 2$ mm^3, and the assembly is encased within two $2 \times 52 \times 30$ mm^3 tungsten plates and held firmly within a $53 \times 53 \times 12.5$ mm^3 cavity in a $50 \times 100 \times 100$ mm^3 block of Lucite. After the 2 components of the PDMS are thoroughly mixed, it is set aside for $\sim$ 1 hour to allow air bubbles formed during mixing to escape. The PDMS is spread on top of the scintillator assembly, the glass face of the H12700B PMT is placed on top, with the interface taped to prevent the PDMS from leaking out. The unit is then inverted, and left to cure for 24 hours with a $\sim$ 4 kg weight placed atop the Lucite block. As illustrated in Fig. 6.3, each of the completed detector assemblies is then housed in a black, light-tight, ABS plastic casing, held together with tongue and groove joints and black nylon screws, minimizing light leakage. The detector anode outputs are connected to sixteen RG174/U BNC cables which pass through small holes at the rear of the assembly and made light-tight with black silicone caulk. The face of the ABS casing nearest the scintillators has 3 mm wide blind pockets cut into it above each channel, reducing the 5% attenuation of γs incident normal to the detector, and providing a visual indicator of the position of each channel. In the final design, a 2" thick lead collimator (not shown) with 1 mm wide slits centered over each scintillator channel is carefully aligned in front of each detector. Using a pair of "long slit" detector which measure one momentum component of a positron annihilation angular distribution was first used by Beringer and Montgomery in 1942 [The Angular Distribution of Positron Annihilation Radiation Robert Beringer and C. G. Montgomery Phys. Rev. 61, 222 – Published 1 March 1942] and became an established technique with the work of DeBenedetti [DeBenedetti S, Cowan CE, Konneker WR, Primakoff H. On the angular distribution of two-photon annihilation radiation Physical Review. 77: 205-212. DOI: 10.1103/Physrev.77.205 (1950)] and Stewart [164]. Later work by Stewart proved that one can use this method to measure features of positron ACAR distributions that indicate positron cooling to cryogenic temperatures [114].

Fig. 6.4 (a) illustrates the positioning of the scintillators with respect to the PMT anodes. Each LYSO scintillator is centered over a group of four PMT anodes electrically connected together to yield one channel (Other geometries were considered including those with scintillators centered between channels as well as directly over channels, however, it was observed that signal from various forms of cross-talk impaired the time resolution). Fig. 6.4 (b) shows the layout of the anode connections for a single LYSO channel's output, with the accompanying electrical schematic illustrated in Fig. 6.4 (c). Each channel has a 53.6 Ohm back termination resistor and a pair of back-to-back Si diodes that provide over-voltage protection for the digital oscilloscopes. An RC filter is built into the high voltage (HV) input and is represented in Fig. 6.4 (d).

6.5 Cross-talk Characterization

Within each modular detector, unwanted signals from adjacent scintillator channels (*i.e.*, "cross-talk") can result from: absorption of Compton scattered γs, reflection and or refraction of scintillation light at the PMT window, and capacitive pickup. Light leakage between nearby channels is exacerbated by refraction on entering the PMT's borosilicate glass face ($n \sim 1.53$). Light from LYSO, with a refractive index of $\sim$1.82, can be expected

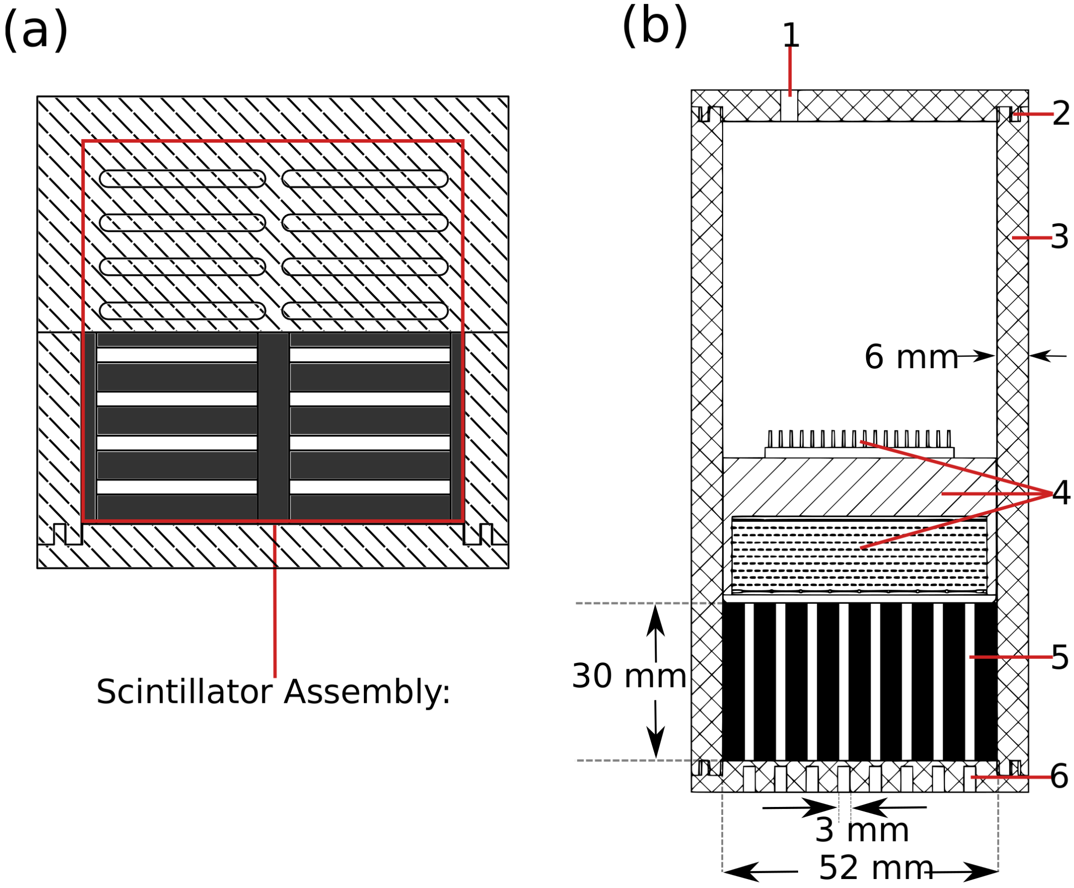

Figure 6.3: (a) Anterior view of detector assembly with the plastic casing half-cut away to show the details of the scintillator assembly: 2 mm thick LYSO scintillators (white) with faces covered with ESR film (not shown) and separated by 4 mm Tungsten (black). The isolators are painted flat black on the faces in contact with the phototube window to reduce light scattering. (b) Cutaway lateral view of the multi-channel scintillator-PMT detector assembly. (1) Feedthrough holes aligned diagonally along back for connections. Holes are sealed after assembly with black PDMS caulk. (2) Light-Tight tongue and groove connections. (3) ABS plastic (cross hatched). (4) Hamamatsu H12700B PMT. (5) Scintillator assembly complete with LYSO scintillators (white) and black painted Tungsten isolators (black). (6) Plastic (ABS) face with 3 mm pockets cut out to eliminate a 5% scattering loss and to indicate the location of LYSO channels.

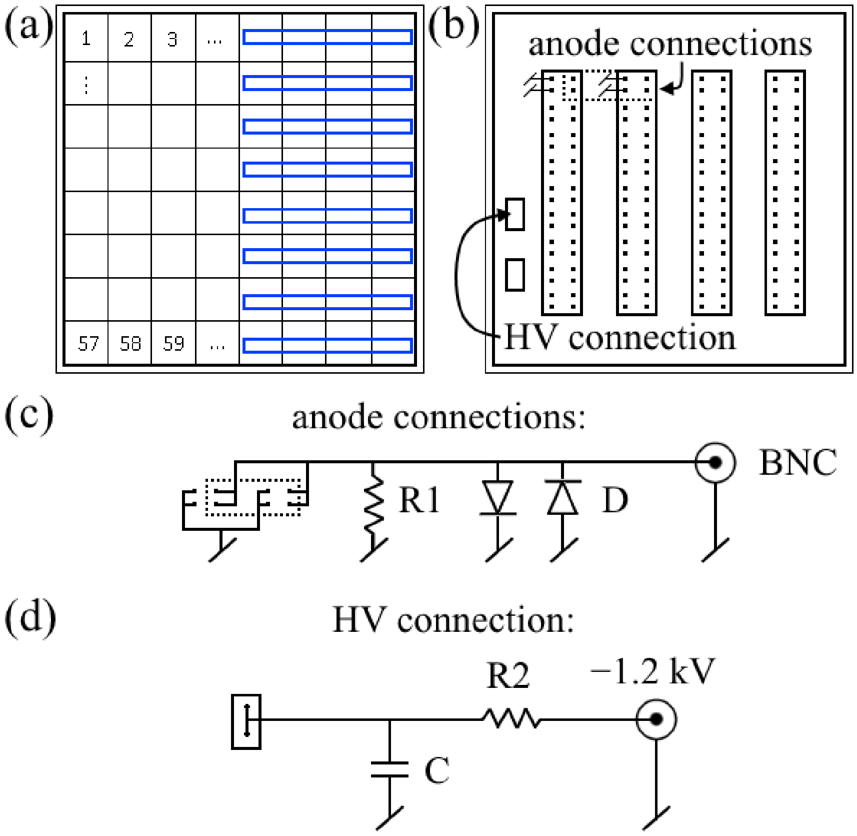

Figure 6.4: (a) and (b) Scintillators (blue) centered over 4 anodes (numbered squares) constituting one channel. (c) PMT/output plug. (e) Connections at PMT output for impedance matching and scope protection. R1=53.6 Ω, D=1N4151 Si diode. (d) High voltage supply circuit with low pass filter R2=100 kΩ, C=0.01 μF.

to refract into a neighboring channel whenever its incident angle at the glass window is $\gtrsim 50^\circ$.

We detected scattered light cross-talk occurring as far as two channels away from the source scintillator. Figure 6.5 provides a summary of data resulting from signals observed in neighboring channels when only 1 photopeak event was recorded on the PMT. From this data, it is evident that cross-talk due to scattered light will not pose a significant problem since the average pulse area detected in the nearest neighboring channel represents only $\sim 2.5\%$ of the original signal.

We have simulated γ-rays depositing energy within the scintillator assembly with scintillators measuring 2×30 mm^2 separated by an isolator (air, lead, or tungsten) measuring 4×30 mm^2. In the simulation, 10^6 511 keV γ's are uniformly distributed with trajectories normal to the 2 mm face, representative of a positron source placed far away and comparable to the geometry of the expected experiment. Attenuation coefficients extracted from NIST data are interpolated to describe a continuous energy spectrum [92]. Upon entering a material (either scintillator or isolator) a γ-ray has a chance of being absorbed with a probability dependent on its energy and the length traversed. Based on data obtained with a 16 channel LYSO-PMT detector, we find that ~ 45 % of γ-ray interactions are full energy "photopeak" events resulting from full absorption of an incident γ's energy. The differential cross section of γ-rays scattered from a single free electron and the ratio of the energy before and after scattering is determined from the Klein-Nishina [109] formula. From this, we create a probability distribution function (PDF) for the energy deposited that is in agreement with the experimental observations shown in Fig. 6.2, but without the low

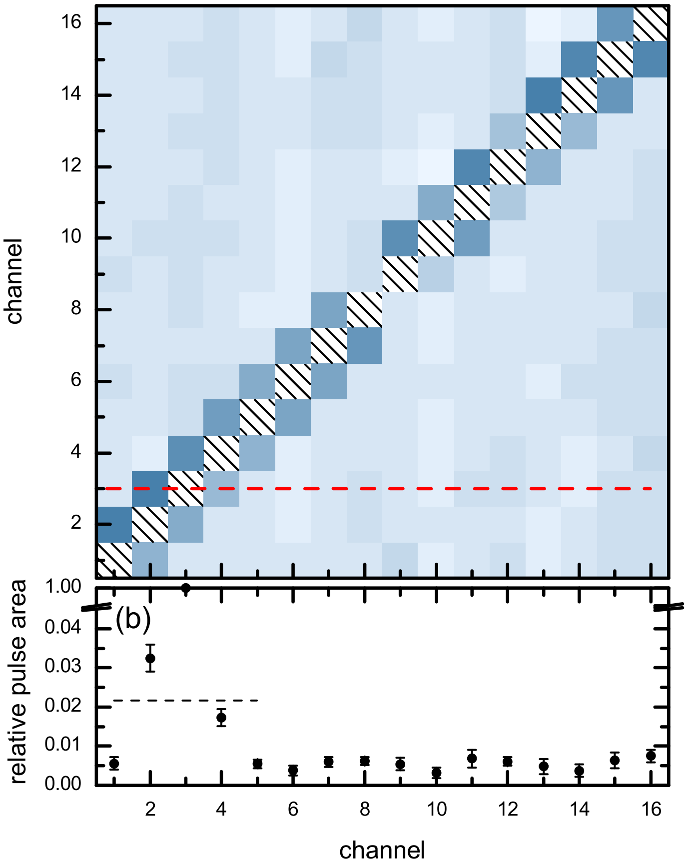

Figure 6.5: (a) Typical cross-talk matrix. The Y-axis is the channel that was directly above a ^{22}Na source. The X-axis is the channel in which a Compton scattered γ or scattered light was observed. The Z-axis is the average pulse area in a channel relative to the average pulse area detected by the scintillator exposed to the Na^{22} source. This defines the cross-hatched diagonal as unity. The remaining data is plotted on gray-scale. (b) Sample data along the dashed line in (a) showing the average signal observed in the nearest neighboring channel is $\sim$ 2.5%

Table 6.3: Percentage of time that a neighboring channel absorbed specified energy in keV (E) after Compton scattering (Simulation results).

isolator	$51 < E$	$51 < E \leq 170$	$170 < E \leq 340$	$340 < E$
air	29.8	10.4	12.2	7.2
lead	5.7	1.9	2.2	1.6
tungsten	3.7	1.3	1.5	0.9

energy peak due to scattered light cross-talk. Results are summarized in Table 6.3.

Simulation results expect more energy to be deposited in a neighboring channel than in the primary channel where the Compton event occurred 2.3% and 1.2% of the time for lead and tungsten isolators respectively. Simulation results predict $\sim$ 2% of incident $\gamma's$ will deposit at least 170 keV (1/2 E_c) into one of the nearest neighboring channels, in close agreement with observation. Using tungsten isolators, the simulation indicates a reduction to 1.4%. Short timescales and large energy distributions make it difficult to correct for Compton events beyond rejecting suspect results. Lead isolators were used in preliminary testing, but are substituted with tungsten isolators in the final design to minimize Compton scattering.

6.6 Data Analysis

During an experiment to measure the momentum distribution of Ps formed in the sample, and following each burst of positrons, the annihilation photon scintillation signals from each channel will be recorded on a set of 96 Teledyne LeCroy WaveAce 2024 4-channel 8-bit digital storage oscilloscopes (DSOs). The 96 DSOs will be arranged in 2 banks with each bank recording data from 12 modular detectors. One computer will download data for each array of 48 DSOs every 10 seconds. To accomplish this, software has been developed that will allow 192 channels consisting of 1024 data points each to be acquired in $\sim$ 830 ms. The raw data collected by each computer occupies 200 KB per shot. At a shot rate of 1 Hz this would consume $\sim$ 16 GB/day. To reduce the storage requirements, the data is compressed before storage as follows.

Immediately after downloading data from a DSO, each channel is adjusted for the measured cross-talk and relative gain. Each recorded waveform is then fitted to the function

$$V(t) = \sum_{i=0}^{i_{\max}} \frac{A_i}{2} \left[1 + \mathrm{erfc}\left(\frac{\Delta t_i}{\sqrt{2}\sigma}\right)\right] \left[\exp\left(\frac{-\Delta t_i}{\tau}\right)\right] \tag{6.1}$$

using a least square trust-region-reflective algorithm [146]. The fit parameters, A_i and t_i represent the amplitudes and times of the prompt pulse ($i = 0$) and up to 3 delayed pulses while σ and τ are obtained from the fits in Fig. 6.1 (b). To avoid fitting an excessive number of peaks, bounds are set such that $A_i \geq A_{\min}$ and $|t_i - t_{i-1}| \equiv \Delta t_i \geq \Delta t_{\min}$ where $A_{\min}$ corresponds to a pulse area equivalent to 1/4 $\mathrm{E_p}$ (see Fig. 6.2) and $\Delta t_{\min} = 5$ ns. The minimum pulse amplitude $A_{\min}$ is selected to reject events likely caused by Compton scattering into neighboring channels. In order to determine the number of peaks $i_{\max}$, we require that the χ^2 of the fit for each $i \leq i_{\max}$ must reduce χ^2 by at least a factor η, such that

$$\eta\chi^2_{i+1} \leq \chi^2_i \tag{6.2}$$

Neighboring points in the waveform record are strongly correlated due to the inability to resolve individual photocathode events. As such, we assign the uncertainty in the individual voltage readings to be

$$\delta V_i = \delta V_0 + \alpha\sqrt{|V_i|}. \tag{6.3}$$

where δV_0 is intrinsic to the DSO ($\geq$ 1 bit, corresponding to 1/256 of the full voltage scale) and the term proportional to the square root of the signal accounts for the expected contribution from the Poisson statistics associated with the collection of individual photoelectrons, scaled by a factor α, where α is tuned such that a fit to a typical 511 keV pulse has a reduced $\chi^2 = 1$.

We systematically adjusted η such that the fitting algorithm remained both reliable and efficient. In Fig. 6.6, the probability of a successful fit for a selection of values of η is plotted as a function of (a) the amplitude of the first delayed pulse (A_1) and (b) the time delay Δt_1. The value chosen for η noticeably affected the fitting routine's success against both A_i and t_i, and the minimum η is chosen to eliminate the anomalies represented within Fig. 6.6 (a) for $\eta = 1.1$. Increasing numbers of fitted pulses must have at least a 25% better χ^2 to be deemed a better fit. In Fig. 6.7 (a) contour lines (and a color gradient) illustrate the fit success as a function of both time delay and pulse amplitude for $\eta = 1.3$. Figure 6.7 (b) illustrates the impact of a more stringent fit condition, $\eta = 2.1$, which has a dramatic effect on small pulses occurring shortly after to the prompt signal. Even in this case, the fitting routine is at least 50% effective for Compton scattered γ's for $\Delta t \geq 50$ ns. The best results are found with $\eta = 1.3$, for which the efficiency is 70% for Compton scattered gammas, and well above 90% for most delayed photopeak events. An overall efficiency of detecting a 511 keV γ is calculated using results from the 2D simulation described in section 6.5 along with the pulse area dependent efficiencies illustrated in Fig. 6.6 (a). For

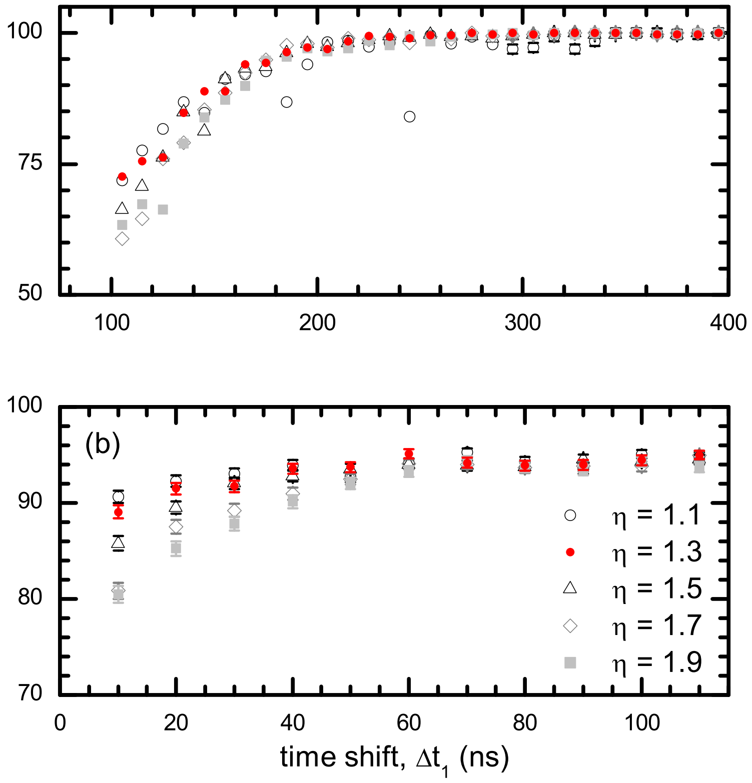

Figure 6.6: (a) Fit success as a function of the first delayed pulse's amplitude (A_1). Average photopeak pulse height: 345 mV. Compton edge: 230 mV (b) Fit success as a function of the time delay Δt_1 between the prompt and the first delayed pulse. The fitting routine was the most successful for $\eta = 1.3$ (red filled circles).

γs depositing between 100 and 511 keV arriving 3 to 120 ns after a prompt signal consisting of 1-3 simultaneous prompt γs, our algorithm correctly detects the arrival time of up to 3 subsequent pulses to within 1.2 ns FWHM with an efficiency of $\sim$ 90%.

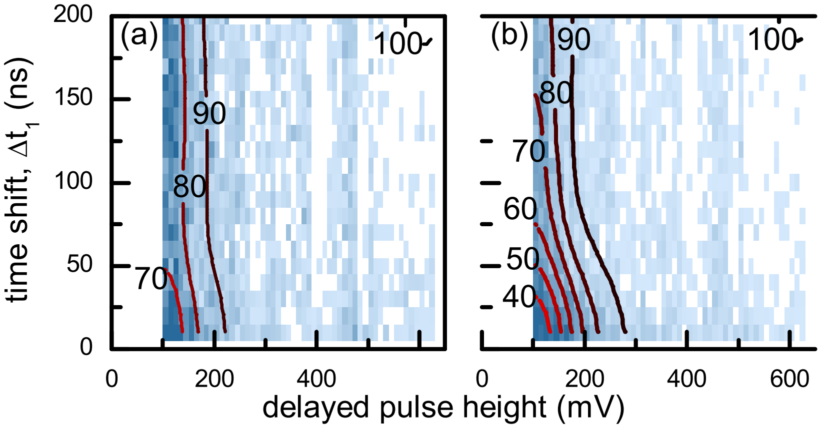

Figure 6.7: Success efficiency for $\eta = 1.3$ (a) and $\eta = 2.1$ (b). Assuming the pulse height scales linearly with the energy deposited by a γ-ray (see footnote 1), the average photopeak pulse and the Compton edge correspond to a peak amplitude of 345 mV and 230 mV respectively.

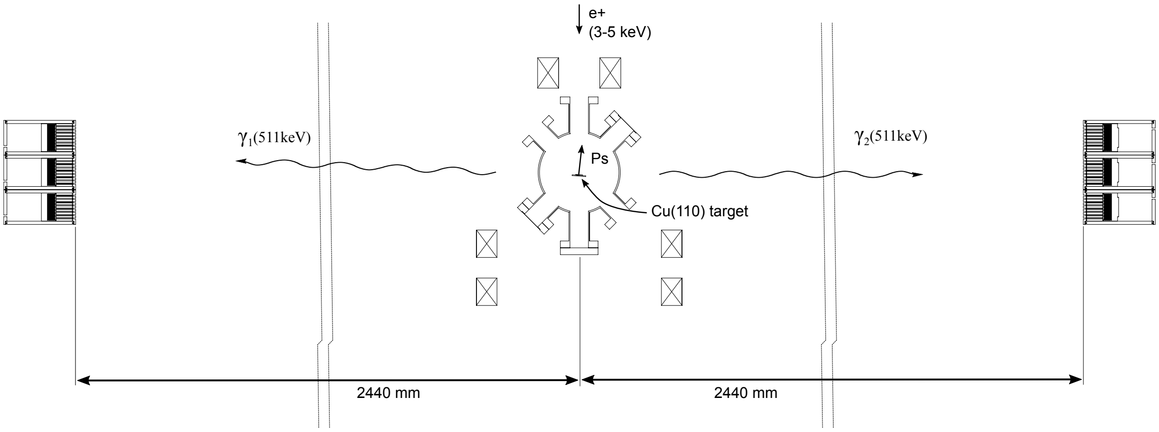

Figure 6.8: Setup for a preliminary experiment having one-quarter of the detectors described in Figure 6.3 placed 4 times closer than the 10 m that will be used in the intended experiment. One bank of multi-element detectors (right) is placed on a translation stage to explore the full spectrum detailed in Figure 6.9. The 2 mm wide scintillating channels subtend 0.8 mrad and are separated by 2.4 mrad.

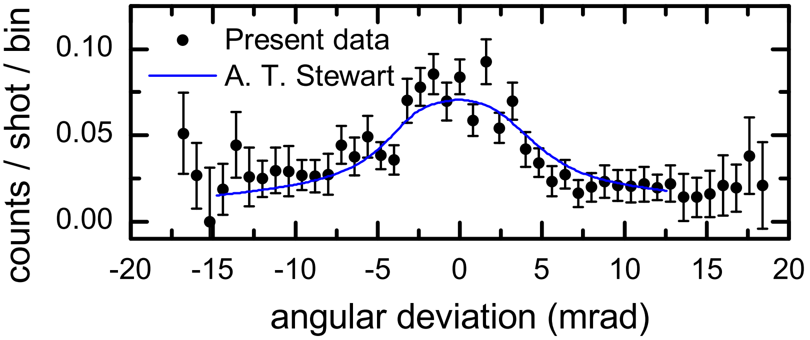

Figure 6.9: Results from preliminary ACAR experiment on Cu(110) (detailed in Figure 6.8) using 6 of the modular detectors discussed in Section II. Data is compared with the results of Stewart [164](solid line) with a uniform background of 0.007 added.

6.7 Preliminary Results

We conducted a preliminary experiment to test the performance of our detectors, and data collection and analysis routines. The experiments made use of three pairs of modular detectors as described above, situated on either side of a Cu(110) target heated to 860 K in our pulsed positron beam [101], at distances of ~ 2440 mm indicated in Fig. 6.8. To eliminate the small asymmetry in the angular correlation due to a few percent γ absorption in the Cu sample, the target is tilted at 10° with respect to a line joining the detectors. With the 2×2 mm^2 face of the LYSO crystals facing the target and LYSO crystals separated by interleaved Tungsten plates, each scintillator channel subtended an angular range of 0.8 mrad with 2.4 mrad between each channel.

Bursts of $\sim 10^5$ positrons every 4 seconds were implanted with kinetic energies of 3-5 keV, ensuring that more than half of the positrons annihilate within the target [144]. Data were collected over the course of 72 hours resulting in ~ 30,000 coincident events. To cover the full angular range, one bank of detectors was set on a translational stage and scanned from 0 to 4 mm by hand in 2 mm (0.8 mrad) steps. The resulting measurement of the angular correlation of the annihilation gammas is plotted in Fig. 6.9.

Our preliminary results (filled circles with error bars) are compared with a previous measurement of the ACAR spectrum of Cu (solid line) [164]. To directly compare our measurement with that of Stewart's, the curve from Ref [164] is rescaled and a flat background added to fit our data. With 31 degrees of freedom, the reduced chi-squared of the fit is 1.07, indicating a statistically reasonable fit. ACAR measurements on simple metals [58] are explained as arising from annihilations with conduction and core electrons, yielding spectra comprised of two major components. For Cu, the component resulting from positron annihilation with core electrons produces a broad Gaussian background distribution with a FWHM of $\sim$ 15 mrad, while annihilations with conduction electrons produce a narrow spread ($\sim$ 8 mrad FWHM) [164]. Both distributions are centered about an angular deviation of zero radians, corresponding to back-to-back gamma-rays. In a 1D ACAR measurement, which the present geometry approximates, the narrow component approximates the shape of an inverted parabola.

6.8 Concluding Remarks

We selected our detector configuration from the arrangements considered herein by comparing various scintillator and PMT attributes. LYSO's short rise time ($\sim$ 3 ns), along with its good light output ($\sim$ 32 photons/ keV), and short attenuation length of $\sim$1.16 cm, resulting in $\sim$ 95% of all incident 511 keV γs producing a signal from the photomultiplier tube, make it the best choice for the planned experiment. The presence of

$\sim 2.5\%$ percent light cross-talk between neighboring PMT channels is easily accounted for given its consistency. Compton scattering of γs causing simultaneous signals in neighboring scintillators is greatly reduced by using 4 mm tungsten shielding plates between scintillators. A subset of 6 modular detectors has been fully tested and the entire set of 24 modular detectors has been assembled and is ready for the first experiments. The final apparatus will consist of a total of 386 channels covering $\sim 1.7 \times 10^{-4}$ steradians with 1 mm wide slits in a 2-inch lead collimator placed in front of each detector and detectors placed 10 m away from a target to yield an angular resolution of 0.1 mrad. The detection efficiency is $\sim 47\%$ for a single pair of back-to-back annihilation γ's depositing 100 to 511 keV after considering the efficiencies associated with a single LYSO channel and the analysis routine. We have avoided providing an estimate of the expected count rate in the final experiment, as there are a number of factors that would need to be addressed (*e.g.*, the size of the prompt pulse, the background rate as a function of time, *etc.*), that would necessitate a comprehensive simulation.

Chapter 7

A Resistive-Anode based Position-Sensitive Rydberg Atom Detector

7.1 Introduction

Many technologies have been developed for the position-sensitive detection of charged particles. For experiments with low signal rates, or those where single particle detection is necessary, most schemes employ microchannel plate detectors (MCPs). In our experiments, which require detection of individual events with accurate timing ($\leq$ 10 ns) [101], high-resolution position-sensitive detection schemes, such as phosphor screens [171] or backthinned CCDs [11], are of limited use due to their relatively long readout times ($\sim$ ms), although this is not an insurmountable problem. Another common position-sensitive detection scheme suitable for single event detection and typically used in conjunction with MCPs are delay-line anodes [117]. In these detectors, with time discrimination of a few ps, it is possible to achieve a spatial resolution of ≤ 100 μm [96], however such systems can be prohibitively expensive.

The position sensitivity taken from a resistive anode on the back of the detector is determined from the relative magnitude of signals measured at each of the four corners. Distortion-free resistive anodes were first proposed in 1969, however these required careful shaping of the anode and edge termination to effectively reduce the distortion of the x, y mapping. Application of this anode design was realized a decade later [116], with good linearity and sub-mm resolution. The practical limitations of this design were later studied in detail [75]. The earliest designs used resistive anodes with large persquare resistances ($R_\square \sim 1$ MΩ) [8, 118], that have the drawback of substantially time-broadening incident pulses, which would limit the energy resolution in our TOF experiments; good time resolution may be achieved with a capacitive pickup behind the resistive anode, but this arrangement does not permit accurate spatial determination of pulses occurring within a few μs of one another.

Recently, a more sophisticated multianode structure with an intermediate resistance ($R_\square \sim 10$ - 100 kΩ) was demonstrated, achieving single-event time discrimination on the order of 20 ns and resolution as low as 100 μm [104]. The resistive anode used in our detector is a square glass plate coated with indium tin oxide (ITO). The ITO coating has a low per-square resistance, $R_\square \sim 15$ - 20Ω at 300 K. This allows for the observation of fast pulses and thus the detection of multiple counts, with individual counts discernible with good spatial resolution to within $\sim$ 10 ns of one another. Unfortunately, the simplicity of the square anode design is offset by a pincushion shaped distortion of the x, y mapping. The distortion is most prominent in the vicinity of the anode corners, with a dependency on both x and y relative to the center of the square [74]. In exploring the various ways of correcting the remaining distortion, the following will: 1) describe the design and construction of the detector and associated electronics; 2) present results of a simulation of the anode, comparing several schemes for correcting the x, y distortion; 3) characterize the performance of chevron and Z-stack versions of the detector; and 4) present Monte Carlo simulations of event detection which accurately model the process of field ionization.

7.2 The Detector

We describe here the components and design of position-sensitive detectors for detecting Rydberg atoms, using two and three MCPs operated in series, in the chevron and Z-stack configurations, respectively.

7.2.1 Design

The detector design is composed of three distinct sections: 1) A region of strong electric field ($\sim 10^6$ V/m) to ionize incident Rydberg atoms, created by a grounded grid situated in front of 2) a two or three-stack MCP, followed by 3) a square resistive anode, with signals recorded at each of the four corners. A second, capacitively-coupled anode, is positioned behind the resistive anode, providing an independent pulse signal for triggering.

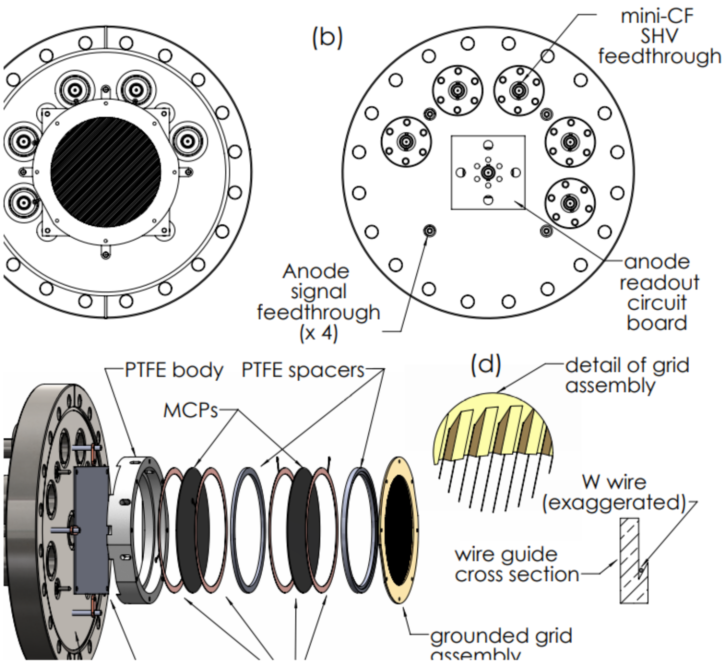

Figure 7.1: Schematic illustration of position-sensitive Rydberg atom detector.

The chevron configuration detector, pictured in Fig. 7.1, employs a pair of Photonis channel plates (model 75/12/10/8 I 60:1 NR) with ∼ 75 mm diameter active areas, positioned inside of a polytetrafluoroethylene (PTFE, "teflon") body. The entire detector assembly is mounted on a 20 cm conflat (8" CF) flange, that has multiple feedthroughs for the application of potentials and readout of signal from the anode. The flange mounting ensures a short path from the anode to the amplifiers, which are mounted close to the outside of the flange, an important measure to maintain a low noise signal. As can be seen in Fig. 7.1 (c) the spacing is maintained between the MCPs, and the grid, by PTFE inserts which form part of a rigid stack of elements. Channel plate potentials are applied to beryllium copper rings, each with a single lollipop extrusion that rests outside of the body of the detector. Each electrode has an electrical connection to a neighboring mini-CF SHV feedthrough on the 20 cm base flange. In the detector configuration illustrated in Fig. 7.1, each microchannel plate has two supply electrodes, defining the front and back potentials for each plate. In the Z-stack configuration, there are just two electrodes, one each at the top and bottom of the MCP stack. This arrangement is discussed in further detail in the following section.

Mounted 3.2 mm above the surface of the front channel plate, a grounded beryllium copper ring supports an array of 25 μm tungsten wires with 1 mm spacing resulting in a geometric transmission coefficient of 97.5%. The potential difference between the grounded ring and the accelerating potential of the top MCP creates a region of approximately uniform electric field of $\sim$ 1 MV/m.

The resistive anode is a square plate of glass measuring $\sim$ 90 mm across and is coated with indium tin-oxide (ITO) to yield an approximately uniform $R_\square$ across the surface and were purchased from a commercial supplier. The anode is mounted directly to the back of the PTFE block that forms the body of the assembly. This design ensures that the MCP signal is only deposited within $\sim$ 6 mm of any of the anode's edges, and about 25 mm from each corner. This arrangement avoids the regions of the anode that display the largest pincushion distortion. The typical sheet resistance of the anodes used in our detectors was measured via the van der Pauw method [149], and was found to be $\sim$ 16.5 Ω. Signal readout connections are made at each of the four corners with feedthrough pins doubling as a mounting structure. Electrical contact to the resistive anode was established using silver epoxy. On the air-facing side of the 8 in flange, the signal feedthroughs are connected directly to a circuit board with four identical amplifier circuits, designed to produce low-noise pulses of large amplitude (> 10 mV) and short time duration (< 10 ns) for precise time of flight measurements.

7.2.2 Electrical setup

1. Voltage supply

As we are detecting the positive ionization product in our experiments only negative potentials are required to operate our detectors. Potentials in both designs are applied via voltage divider circuits and require just one HV power supply. For the chevron detector, the supply circuit, illustrated in Fig. 7.2 (a) has four outputs which are connected via SHV feedthroughs to copper rings positioned on both sides of each MCP. The HV supply circuit for the Z-stack detector, illustrated in Fig. 7.2 (b), is similar, however the resistive chain makes use of only the ~ 28 MΩ resistance across the MCPs.

Under typical operation, the supply is set to -3 kV, which produces a potential across each plate of $\sim$ 1- 1.2 kV and a ~ 500 V extraction bias between the rear plate and the anode to guide electrons directly to the anode. The 3 kV potential difference between the grounded grid and the front of the MCP stack, which is positioned ~ 3.2 mm away, produces a region of nearly uniform ionizing electric field of 9.4×10^5 V/m, sufficient to rapidly ionize any Rydberg Ps [90] atoms of principal quantum level n ≥ 5. Leakage of the field through the grounded grid is considered in detail in Section 7.3.2B. following.

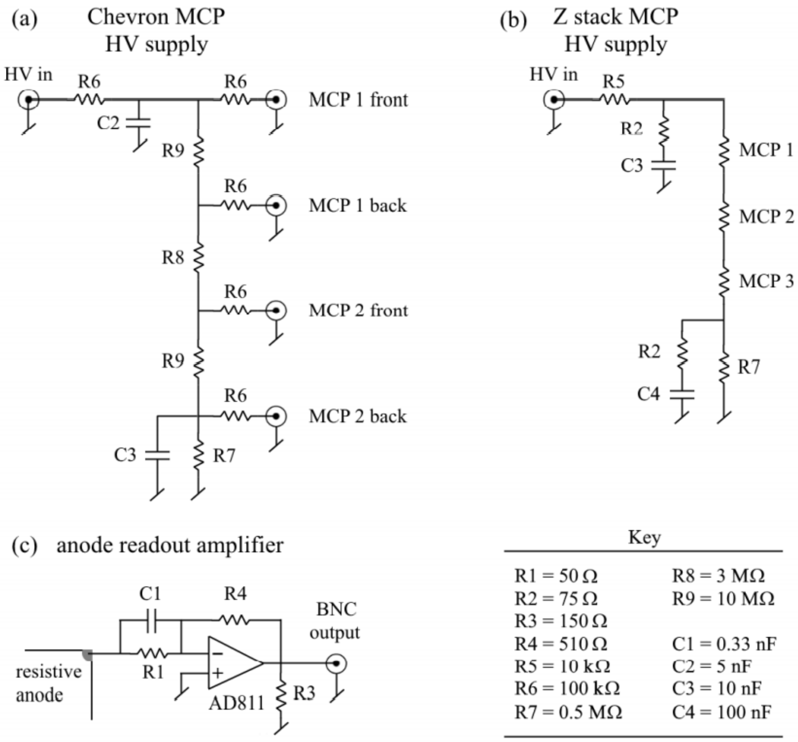

Figure 7.2: Circuit diagram of voltage supply and dividing circuit for position-sensitive Rydberg atom detector.

2. Amplifier

Two distinct amplifier circuits were employed in our detector. The first circuit is a preamplifier, illustrated in Fig. 7.2 (c), and was assembled on a circuit board attached directly to the same flange as the detector in close proximity to the anode. Leads $\sim$ 5 cm long are connected through feedthroughs from each of the four corners of the anode, as indicated in Fig. 7.1. The signals are terminated through 50 Ω input resistors. A parallel 'peaking' capacitor increases the high frequency gain. The transmitted signal is amplified by a factor of $\sim$ 3.4. The use of 50 Ω input resistors was based on the assumption that it would match the impedance of the anodes. In later testing we found a mean sheet resistance of 16.44 ± 0.23 Ω at 297 K (with a temperature dependence of 18.6 ± 0.3 mΩ/K). Following this measurement, the anode readout amplifiers were tested for signals applied directly to bare anodes. In these experiments, it was found that a lower value of R1 has a significant impact on both pulse area (up to 75% larger) and resolution (as much as 5.5x better), with the best results found for R1 of 1 to 5 Ω. In the characterization tests described following, R1 = 50 Ω.

7.2.3 Testing of resistive anode schemes

In order to model some of the expected discrepancies in position mapping resulting from the non-ideal properties of the physical anodes, we simulated the anode as a network of between 4 *times* 4 to 8×8 50 Ω resistors using the SPICE package. The simulation model is used to estimate the expected quality of the correction. We also use the simulation to model the distortion of the measured positions resulting from small variations in the

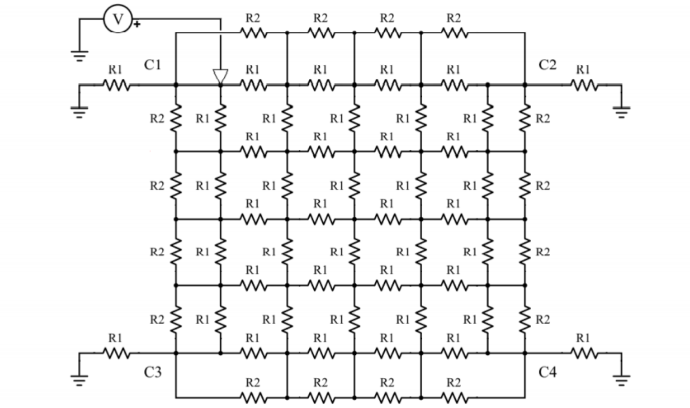

Figure 7.3: Example electrical schematic model of resistive anode

amplifier outputs. A schematic of the simulated circuit is illustrated in Fig. 7.3, illustrating the 4 × 4 array configuration with edge resistors. Most of the simulation results presented here are performed with edge resistors R2 removed. Position data are calculated from the measured voltage magnitudes at each corner junction C1-C4, for a fixed DC voltage applied at each of the grid points defined by the array of resistors R1. The applied voltage is input via a triangular symbol, denoting a probe, which is shown connected to the upper left corner in the figure.

Simulation results are shown in Fig. 7.4 (a) contrasting the output of a 6×6 array of resistors (filled shape and black points) that was corrected by connecting 2 Ω resistors along each edge of the anode (red open circles), in a configuration similar to that illustrated in Fig. 7.3. The distortion resulting from the effect of charge accumulation along the boundaries of the anode is seen to be largely eliminated with edge terminating resistors. The distortion is further improved with ever smaller values of edge resistance, however this

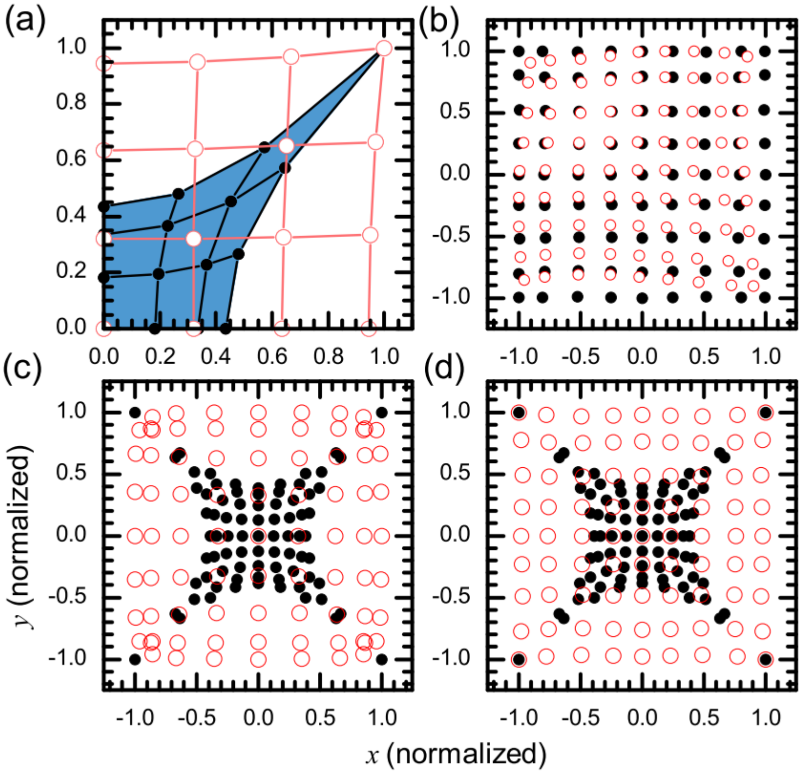

Figure 7.4: Resistive anode simulation with pic-cushion effect and correction for the simple resistive network model in Fig. 7.3

also results in the amplitudes of pulses observed at the four corners converging on uniform magnitude. This makes the practical application of such a corrective scheme sensitive to electrical noise. Experiments were also performed using 50 mm anodes and connecting the corners with lines of 2 Ω surface mount resistors with similar results observed. This was dismissed as a solution due to the difficulty in preparing the resistors for vacuum use, the excess silver epoxy required and the need to correct for the residual distortion.

The lack of systematic effects and other experimental uncertainties makes the anode simulations ideal for precisely testing the mathematical transform required to correct the measured positions. Using an 8×8 array of resistors we produce a coarse grid of measurements by applying a uniform potential at each node of the network and measuring the voltage at each corner. As illustrated in Fig. 7.4 (c), we find that the first order correction can transform the measurements such that points align along lines of approximately constant x and y, as the array of inputs do. However, it does not reproduce a uniform grid, as the gaps between adjacent points decrease with distance from the origin.

To perform a more accurate transformation, we empirically derived a correction formula with additional terms in x^2 and y^2 as follows,

$$\begin{aligned} x' &= \frac{x}{1+\alpha y^2 - \beta x^2} \\ x' &= \frac{x}{1+\alpha y^2 - \beta x^2} \end{aligned} \tag{7.1}$$

The best results are found with $\alpha \approx 7.9$ and $\beta \approx 5.7$ and are plotted in Fig. 7.4 (d). Although there is clearly some residual distortion, the RMS radial deviation is just 0.34% which corresponds to a deviation of about 0.3 mm in our apparatus.

In Fig. 7.4 (b), the effect of non-uniform amplification of the anode output are illustrated. In this example, the simulated data of the top left corner (*i.e.*, C1 of Fig. 7.3) is multiplied by a factor of 1.1, slightly larger than the observed variation in amplifier outputs in the assembled detectors ($\sim$ 5%) to exaggerate the effect. Black circles illustrate the corrected results of Fig. 7.4 (d), while overlaid red circles illustrate the distortion introduced by the non-uniformity. Here, the distortion is seen to be centered around a point at $\sim$ (-0.4, 0.35), though the exact location of overlap depends on the correction constants α and β. The largest deviations are seen to occur near corners C2 and C3, where the reconstructed x, y points are about 10% of the anode size from their correct locations (a positional error of $\sim$ 10 mm in our detectors). The maximum distortion is approximately twice the magnitude of the applied amplification error and results from the dependence of the correction on terms in x^2 and y^2. This study highlights the importance of careful calibration of the corner output amplifier circuits.

7.3 Chaacterization of Position-Sensitive MCP detector

7.3.1 Detector performance

1. Timing resolution

Typical measured pulse spectra, each recorded at one of the outputs of the anode readout amplifiers, are plotted in Fig. 7.5 for the Chevron and Z-stack detectors (plots (a) and (b), respectively). The two spectra have been time-shifted following fitting, such that the rising edge is centered about t = 0. As the two pulse shapes are distinct, the fit models are slightly different. The model used to fit the Chevron data is the product of an error

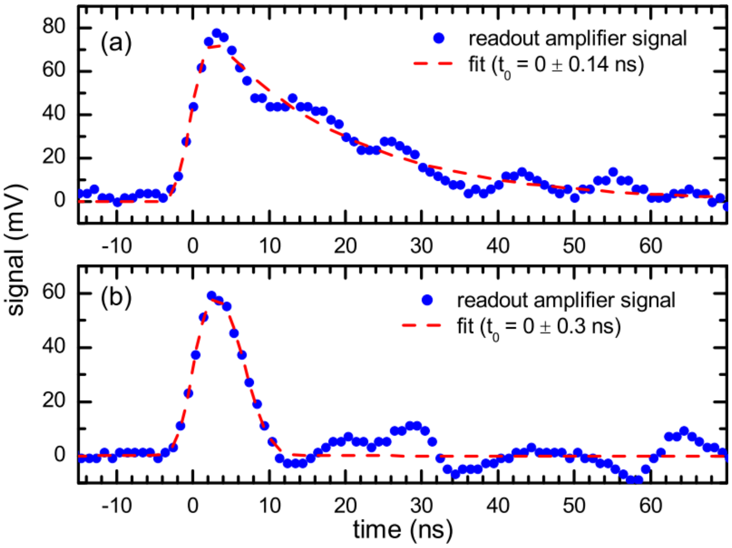

Figure 7.5: Voltages anode readouts from (a) chevron and (b) z-stack MCP detectors.

function about t = t0 and an exponential decay, while the Z-stack data is fitted to the product of an error function at t = t_0 and a complementary error function at t = t_f. Each fit yields a sub-ns time resolution, with the best precision found in the fit to the Chevron data. Here the uncertainty in t_0 is just ±140 ps.

Based on the pulse shape recorded from the Z-stack detector output, which has a FWHM resolution of $\sim$ 7 ns, pairs of individual events are discernible provided the time separation is $\geq$10 ns. Distinguishing individual counts from the Chevron detector require pulses to be separated by $\geq$20 ns due to the 30 ns exponential tail.

2. Spatial resolution

Amplified pulses from each of the anode's corners are recorded at a sampling rate of 1 GHz on a Lecroy WaveAce2024 oscilloscope. Pulses resemble skewed normal distributions,

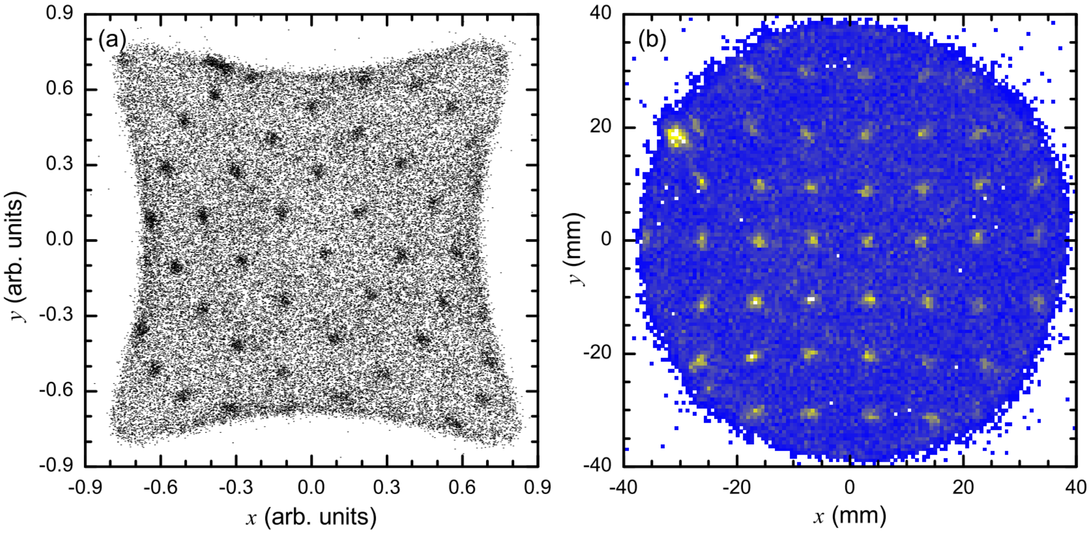

Figure 7.6: Collection of raw counts (a) on MCP detector using UV and mask combo and corrected transformation (b) expressed in Equation 7.2.3.

with an initial rise time of 2-3 ns followed by an exponential tail with a decay time of ~ 7 ns. The pulses must be corrected for the relative amplification of each circuit, typically on the order of a ±5% rescaling, by calibration against a measured response to uniform input. If signal amplitudes are left uncorrected there is a distortion in the recorded position data, as shown in the simulated results plotted in Fig. 7.4 (b).

In Fig. 7.6 (a) raw x, y detection events are plotted from UV induced signals, taking here only the detections with mean pulse areas in the uppermost 20% of the available data. Light from a low-intensity Ocean Optics CW mercury argon calibration source lamp (253-922 nm) placed ~ 1.4 m away illuminated the detector. A stainless steel mask with a uniform array of 1 mm holes spaced 10±0.5 mm apart was positioned immediately in front of the detector to produce a well-defined detection pattern for spatial calibration and the determination of signal resolution. Positions of individual detection events are determined from the recorded pulse traces collected at each of the four corners of the resistive anode. The gain of each channel is corrected here to recover a spatially symmetric distribution of counts. The x, y position of each event can be found by taking the appropriate ratios of the peak amplitudes or areas. For the data presented here, pulse areas are extracted from fits to the pulse traces, with individual pulses modeled as Gaussians with a tail with two exponential decay terms.

In Fig. 7.6 (b) the raw data of plot (a) are presented as a histogram of counts following transformation of the data as per equation 7.2.3. Values of $\alpha = 13.5$ and $\beta = 5.5$ are used here, and the corrected data is subsequently rotated through $\sim 43^\circ$ to align the pattern of peaks with the plot axes. In both figures there is a clearly defined mask pattern. Following transformation, the mask pattern is very nearly uniform along the x and y directions across the entire active area of the detector, though some distortion of the peak positions is evident near the edges. The scale of the data here is established from the same process used to determine the resolution.

To measure the resolution of the position sensitivity, we take vertical and horizontal slices through the center of the data and fit the peaks with a series of Gaussian peaks on top of a background that is typically treated as either uniform or linearly varying. One such fit is shown in Fig. 7.7 (a). To determine the resolution we first find the weighted average separation of peaks, in the natural units of the data (which tend to lie in the range of -1 to 1, but can be arbitrarily rescaled). Results of two such fits, one from a horizontal and one a vertical slice, are plotted in Fig. 7.7 plot (b). The weighted means of the fitted gaps are illustrated as dashed horizontal lines, with the range of $\pm 1\sigma$ represented by the filled

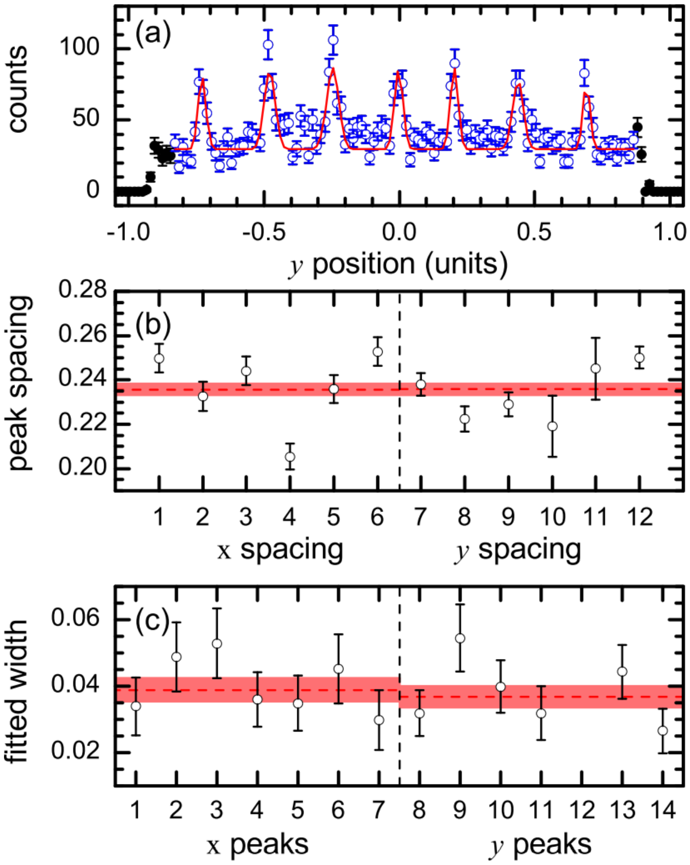

Figure 7.7: Spatial resolution of MCP detector from UV and mask combo data in Fig. 7.6

band. Encouragingly, the weighted means of the two sets of fits are found to be in excellent agreement (0.2357 ± 0.0026 units spacing in x compared with 0.2358 ± 0.0025 units in y). Finally, in plot (c) the fitted FWHM of the peaks are plotted, again for the horizontal and vertical slices. Here too, the weighted means of the fitted results are in excellent agreement (0.0389 ± 0.0035 units along x compared with 0.0368 ± 0.0031 units along y).

The fitted FWHM can be converted to mm by noting that the separation of peaks is 10 mm. The effective spatial resolution of the detector must then be unfolded from the measured widths, which is inflated due to the 1 mm diameter hole size and also affected by the binning of data prior to fitting. FWHM resolutions determined in this manner are plotted in Fig. 7.8, for data from both the chevron and Z-stack based detectors.

To find the dependence of the resolution on pulse size A, the chevron data has been divided into segments representing 20% increments of the pulse area distribution. Each data set is fit to a curve of form resolution = C/A^n, where C and n are the fitted parameters. For noise limited data, simulation suggests an inverse relationship to area (*i.e.*, n = 1), whereas if the statistics are Poisson limited, the resolution would be $\propto 1/\sqrt{A}$ (*i.e.*, n = 0.5). The Z-stack results, for which there was less UV mask data available has been divided into quarters. For the Z-stack data, the resolution is consistent with an inverse proportionality to the square root of the pulse area ($n = 0.484 \pm 0.084$) as might be expected for data limited by Poisson counting statistics. The chevron data however is found to improve more rapidly with pulse area, with the fit yielding $n = 0.857 \pm 0.057$. This may be due to a large, uniformly distributed, background of signal which underlies the observed peaks which is found to be particularly prominent for small pulse areas. If so, this is an effect of the measurement

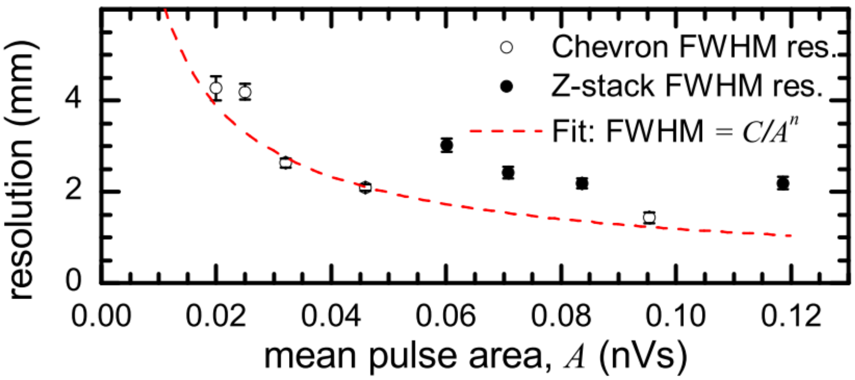

Figure 7.8: Spatial resolution vs average integrated signal

process and is not necessarily indicative of the trend in resolution extrapolated to larger pulse intensities. In fact, fitting only to the three data points of largest pulse area yields n = 0.577 ± 0.071.

It is not clear why the Z-stack detector, despite producing pulse of larger area, did not yield a better resolution than that achieved with the chevron detector. This might be attributed to imperfections in the resistance of the ITO anode, or excess noise in the MCP or gain electronics. However, the larger typical pulse areas and the observed trend in the resolution ($\propto 1/\sqrt{A}$) suggest that the signal resolution is limited by Poisson statistics, not noise. In both data sets, there was a transient 100 MHz signal apparent, which we attribute to a local FM radio frequency. Efforts to minimize this pickup led to the development of brass shielding for the detector electronics which may have been absent for the initial Z-stack experiments. A second possible explanation is some systematic error in the experimental arrangement used for the Z-stack calibration measurements. Here the distance between the lamp and detector was shorter, no optics were employed, and the mask was more distant from the MCP. It is conceivable that the signal observed at the detector could be additionally broadened due to scattering of the light between the source and mask.

In a previous work characterizing a similar field ionizing detector18, we found that when collecting Rydberg Ps directly, *i.e.*, allowing the Rydberg atoms to ionize in the field leaking through the MCP pores, where expected collision energies are $\leq$40 eV, the pulse area distribution was comparable to that seen here for the chevron configuration. If the incident atoms were instead ionized, and the freed positrons accelerated to 1-2 keV, the pulse area distribution was significantly broader (0.05-0.7 nVs), with a mean area $\sim 6\times$ larger. Extrapolating from the spatial resolution measured in the chevron detector and assuming a pulse area dependence of $1/\sqrt{A}$, we predict a typical resolution of 0.7 mm for pulses of 0.35 nVs area, and as good as 0.5 mm FWHM for the largest pulse areas expected.

7.3.2 Rydberg atom field ionization Monte Carlo simulation

Incident Rydberg Ps atoms are ionized in the $\sim 10^6$ V/m electric field created between the front of the first MCP and a fine wire array suspended $\sim$ 3 mm above it woven on a grounded plate. The wires are 25 μm in diameter, spaced $\sim$ 1 mm apart, and are aligned in a single direction, for a net coverage of $\sim$ 2% of the MCP area. In the following discussion, we consider effects related to the fine-scale structure of the electric field permeating through the grounded wire array.

Due to the disparity in the scale of the field outside of the detector and that in the vicinity of the grounded wires, these two problems have been treated separately here. To estimate the magnitude and extent of the field outside of the detector, the electric potential

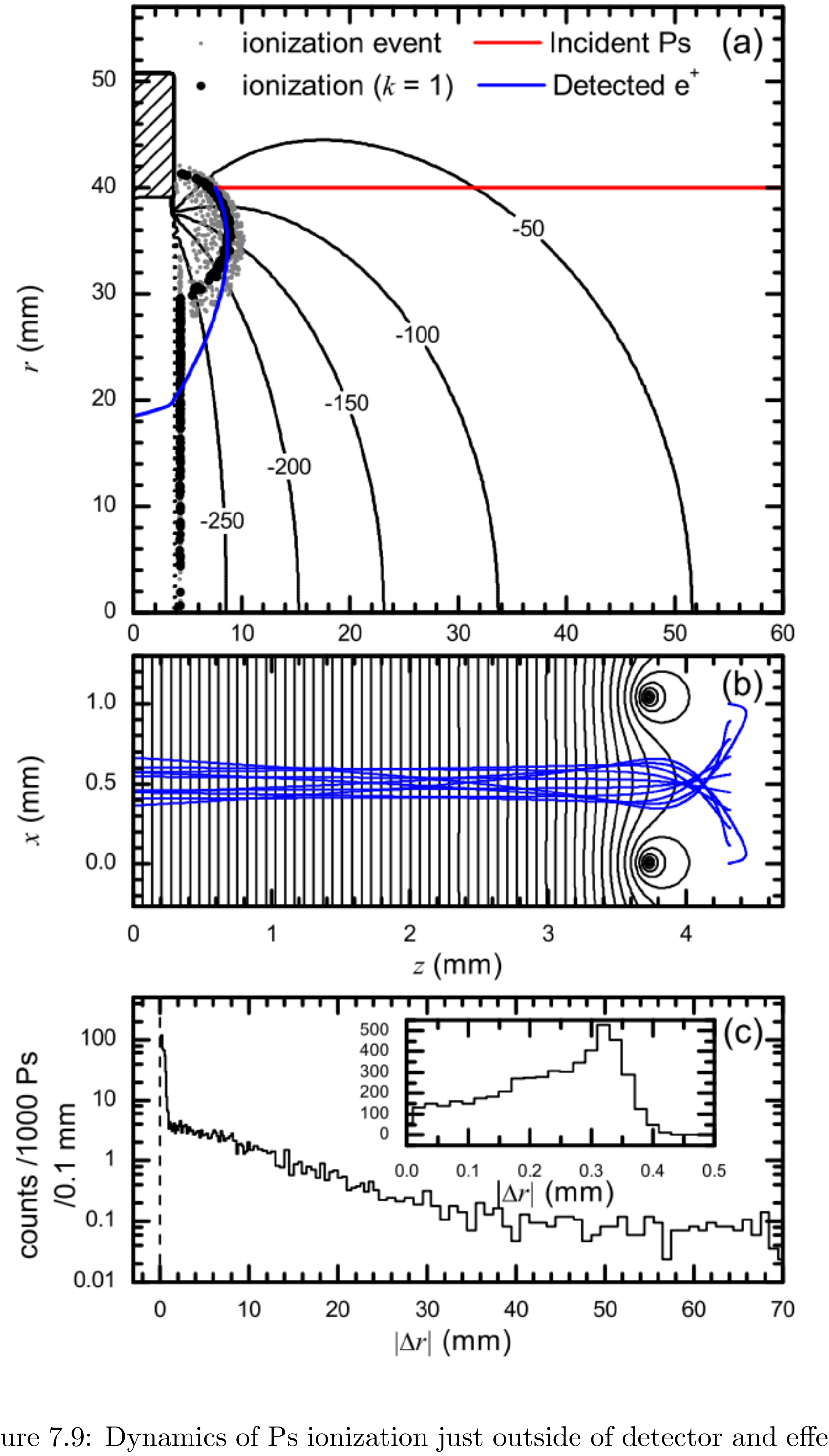

Figure 7.9: Dynamics of Ps ionization just outside of detector and effects on spatial resolution

is calculated in 2D using cylindrical symmetry in Matlab's PDE toolbox. In Fig. 7.9 (a), the potential outside of the detector is illustrated in a contour plot, with the potential inside the detector omitted for clarity. In this approach, the wire array is treated as a set of concentric circles, with diameters and spacing taken from the real device. Although this treats the array as a set of concentric circles, it should provide a reasonable approximation of the electric field around the detector.

The results of a simulation of Rydberg Ps ionization are plotted in Fig. 7.9 (a) for a thermal distribution of Rydberg Ps atoms of principal quantum state n = 32. The simulation assumes a uniform distribution of incident trajectories in x, y (*i.e.*, using a linearly increasing radial distribution) and a uniform population of Stark states (magnetic quantum number m = 0 and k = -31, -29, -27, ..., 29, 31, where k is the difference between the parabolic quantum numbers n1 and n2 [17]). Grey points indicate the positions upon field ionization of the simulated atoms, for all states k. The narrow band of black points illustrate the end points of k = 1 Ps. The outward bulge of ionization observed at the edge of the detector results from the potential difference between the PTFE body (represented by the shaded rectangle) and the front MCP situated at z = 0.

In the simulation, the insulator is assumed to support a linearly varying surface charge with a potential gradient between the -3 kV of the MCP and the grounded grid. While this approximation is not necessarily ideal [19, 153], it is found that there is virtually no difference in the magnitude and shape of the electric field outside of the detector when the insulator is instead modeled as a grounded surface. The simulation also provides an estimate of the positional accuracy of the detector. Freed positrons from the ionized Ps atoms are accelerated into the detector, providing a measure of the anticipated deviation in the radial position $|\Delta r|$ upon detection relative to the incident trajectory. The resulting distribution of radial deviations is plotted in Fig. 7.9 (c).

Those atoms that ionize immediately in front of the grid, constituting approximately half of the atoms detected, reach the detector within ± 0.35 mm of their incident radial positions, as illustrated in Fig. 7.9 (b). The remaining half of the detected atoms, which undergo ionization in the field at the edge of the detector, result in positrons being accelerated radially inward across the detector, as illustrated by the example positron trajectory plotted in Fig. 7.9 (a). These positrons can be accelerated across the entire face of the detector prior to detection, and produce the broad component of the distribution plotted in Fig. 7.9 (c), with a FWHM distribution of ~ 20 mm, and will create a halo ~ 10 mm thick on the outside edge of the detector.

This renders the outer portion of the detector useless for position-sensitive measurements, but can be readily overcome. The simplest solution involves selection of Rydberg states that can not be readily ionized in the field outside of the detector, however a decrease in ionization rate is typically accompanied by a decrease in the radiative lifetime of the state. A second, more robust solution is to use a grid with greater coverage, which better terminates the field, extended out past the MCP, and the placement of an aperture a few cm in front of the detector, to prevent trajectories that would encounter the edge-field of the detector assembly from reaching the detector.

Transport through the wire array is treated by a linear model of the electric field around the grounded wires, found via an iterative relaxation approach. The calculated potential is illustrated in Fig. 7.9 (b) as an equipotential contour plot. The trajectories plotted are purely illustrative, set at the mean z distance of ionization found in the preceding simulation at uniformly spaced x positions and clearly demonstrate the focusing that occurs on acceleration into the detector. The results of the complete simulation, which utilized the distribution of ionization events along z found in the simulation of Fig. 7.9 plot (a) excluding those occurring in peripheral field, are plotted as a subplot of Fig. 9 (c). These results are broadly consistent with the narrow distribution observed in the full scale simulation, and indicate a FWHM blurring of the detected position of ~ 0.6 mm.

This effect only results from the lens like field near the grid; if possible this blurring can be avoided by selecting a lower Rydberg level, to ensure ionization occurs within the region of uniform field. It should also be noted that the broadening observed here is confined to the direction perpendicular to the grid wires. For some experiments, such as in a measurement of the gravitational deflection of Rydberg Ps, this effect can be largely circumvented by aligning the detector such that the grid wires are vertically arrayed, thus ensuring the distortion only affects the horizontal component of the atom's positions.

7.4 MCP Detecor Conclusion

Described here is a position-sensitive detector for Rydberg atoms, designed principally for experiments involving Rydberg Ps TOF measurements. The detector couples a resistive anode having low sheet resistance with a chevron or Z-stack MCP detector. Our design deviates from existing resistive anode based designs through the use of a square, low-resistance anode. The low surface resistance permits the fast timing necessary in our experiments but, through increased thermal noise, restricts the achievable spatial resolution. The detector produces pulses with a 10 ns FWHM time resolution, allowing discrimination of individual events to at least $\sim$ 1 ns precision. The use of a square anode, rather than one of Gear's design [78] results in a pincushion distortion in the raw spatial data. Through experiment and with the aid of simulation, we find that a simple correction with two second order terms accurately reproduces the expected mapping, with a residual RMS deviation from uniformity of just 0.34% relative to the anode diameter, which equates to a deviation of $\sim$ 0.3 mm, comparable to the expected achievable resolution.

The measured spatial resolution is 1.4±0.1 mm FHWM for the largest UV induced pulses. The use of Rydberg atoms is known to produce pulses that are $\sim$ 6x larger [8] on average [100], which, using a conservative extrapolation, suggests a resolution of $\sim$ 0.5 mm for the largest pulses expected. Furthermore, if the amplifier readout circuits are adjusted for a lower resistance (cf. resistor R1 of 7.2 plot (c)), the recorded pulse amplitudes are expected to be 50 to 75% larger, yielding further improvement in the resolution. In tests of the anode readout circuits, the modest increase in pulse area was found to yield large improvements in the resolution, well in excess of the trends observed as a function of pulse area in the full detector tests, suggesting a drastic improvement in the signal to noise ratio. Based on pulse area alone and using a conservative extrapolation we thus anticipate a further 20-25% improvement in resolution associated with changing the readout resistor in the amplifier circuit. Assuming these gains are realized in the completed detector, the resolution achievable is likely to be at least 0.38 mm.

Finally, we note that the use of an electrostatic lens system, situated between the ionizing field region and the first MCP can provide further improvements in the resolution of the detector by expanding the image of a small collection area, or greatly increase the collection area via a focusing lens, the latter of which was demonstrated previously [100] in another Rydberg detector without position sensitive detection.

Chapter 8

Accumulator for Intense Instantaneous Current-Density Positron Plasma Bursts

8.1 Accumulator Design

The positron lab at UCR employs an ultra high vacuum positron trap called the accumulator. The accumulator works similar to the primary buffer gas trap described in Section 2.2 in that there is a strong axial magnetic field (600 Gauss), internal electrodes confine positrons along magnetic field lines, and a dense inert gas is introduced at low pressure. Conversely however, the accumulator captures bursts of $\sim 4 \times 10^5$ positrons at 2 Hz instead of a continuous flux of $\sim 1 \times 10^7$ s^{-1}, and the collected positrons are trapped via collisions with both CF_4 and other trapped positrons.

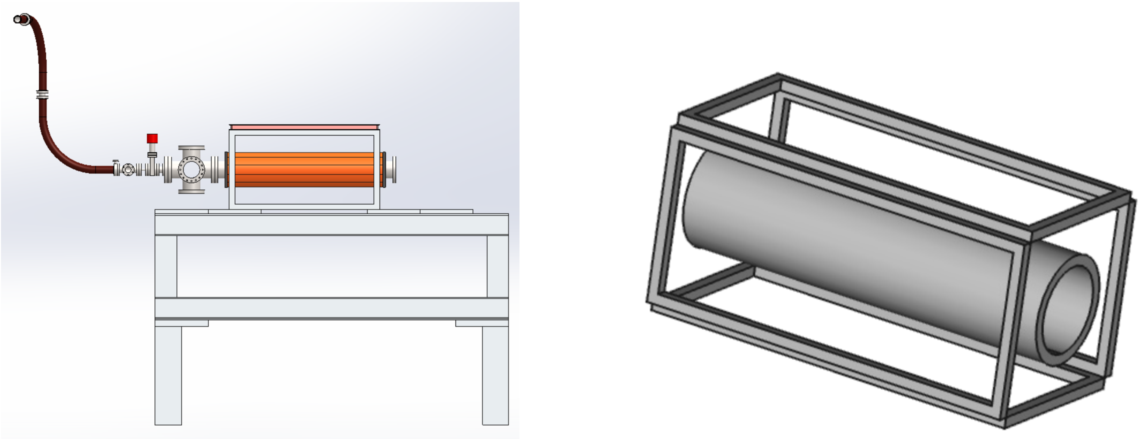

Figure 8.1: Accumulator model (left) and accumulator magnets (right)

Outside the main chamber of the accumulator is an inlet port for the CF_4 cooling gas attached to the 6-way cross in Fig. 8.1 (left). The cooling gas pressure is PID controlled and dynamically changed, a critical feature explained in Section 8.2. The 12-layer electromagnet solenoid for the accumulator is specifically made to increase the field homogeneity where positrons are collected. The electromagnet is wound using Polyesterimide enameled #10 copper wire, class 180, on a hollow water cooled hollow coil form made from 1/8" wall round brass tubing, with an outer tube 6" od and an inner tube 5.25" od, precision cut 36" long, with dimensions accurate to ±0.01". The outer tube was machined on a lathe with a symmetrical 90-degree spiral groove with 0.148" pitch, such that each layer lay inside the previous layer. The weight of the form is 50 lbs including two brass end plates that are helically cut such that subsequent winding layers lie totally within the grooves of the previous layer. The layers are hand wound, always starting from the same end, with the beginning and the end of each layer spaced out with 12-fold symmetry. The return connection from each layer to the next were made after the coil was completed by a set of 12 axial leads evenly spaced around the outside of the completed winding. The total number of turns is 2880 and the weight of the wire is 163 lbs. The approximate central magnetic induction is B $= \mu_0 \frac{NI}{L}$ = 792 gauss with I=20 A. Unfortunately the brass water-cooling manifold leaked at the very start and had to be operated at below atmospheric pressure. In about 2019, after many power failures and shorts to ground of one of the two winding leads of each winding due to corrosion from the leaks and from condensation, all of the 12 layers are presently individually powered by a set of 12 floating power supplies. Each winding is protected from arcing by a high current reverse biased diode across its leads. Large transverse electromagnets are placed around the accumulator and tuned to cancel stray magnetic fields as depicted in Fig. 8.1 (right). Meticulous care was taken to reduce magnetic asymmetries as much as feasibly possible in and near the region positrons are trapped to improve the performance of the trap as will be shown in Section 8.3.1.

The accumulator electrode structure is composed of 30 electrodes as shown in Fig. 8.2 (left), each of length 9.61 m and with 22.2 mm ID, and with the central electrode (hereinafter referred to as the "ring") azimuthally divided into 4 equal segments. Mechanical electrical connections (*i.e.*, not soldered) shown in Fig. 8.2 (left) reduces out-gassing within the vacuum chamber and the electrical connections to the outside of the vacuum system are made via standard UHV feed-throughs which are connected to a modular power supply nearby. The electrode supply contains 5 distinct boards: (1) a main board with fast acting MOSFET switches for each electrode, connections for the five main sections of the trap, and a resistor chain to produce a DC harmonic well; (2) a quadrature phase RF oscillator generated by an AD9959 4-channel direct digital sine wave synthesize IC which

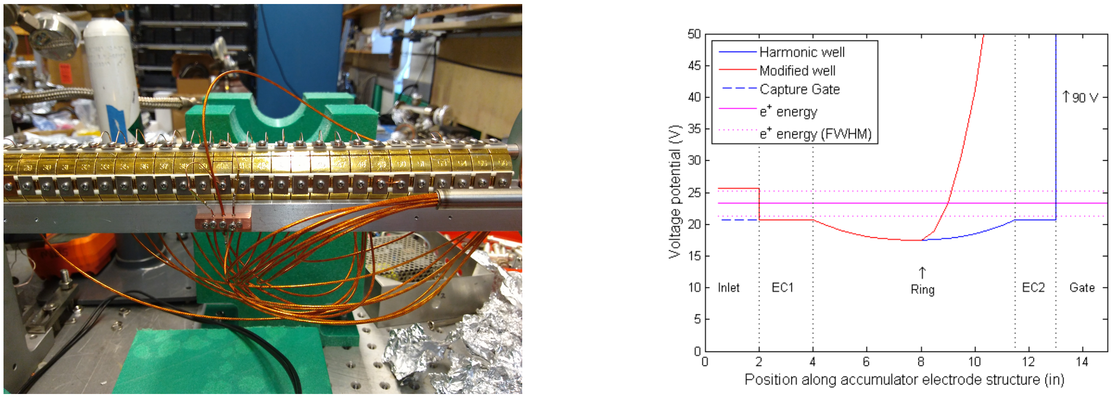

Figure 8.2: Accumulator trapping electrodes (left) and electrostatics (right)

is amplified and AC-coupled to the ring electrode to make a rotating electric field ("rotating wall"or R.W.); (3) electrode dependent ps-precision micro-control delay lines; (4) electrode-dependent computer-controlled high-voltage supplies for ejecting positrons from the accumulator; and (5) a USB interfacing control board. The RW technique is common in single-component plasmas trapped in Penning-Malmberg traps and uses an azimuthally rotating electric field to counter the radial electric field of the plasma, thus driving particles inward and increasing the density. If the quality of the magnetic component of the trap is good, and if there is little asymmetry induced by the transport electrodes, then the "strong-drive" regime can be accessed, whereby the plasma spins synchronously with the RW frequency, and the plasma density increases in proportional to the RW frequency [55, 56].

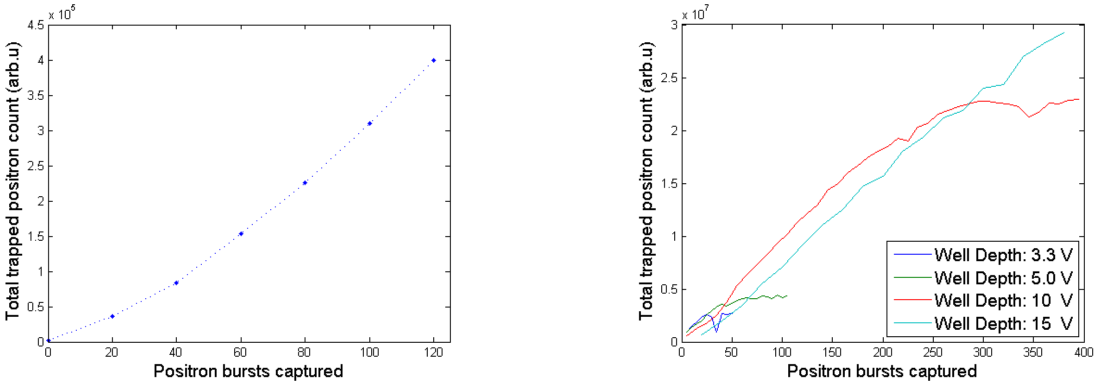

Figure 8.3: Performance of accumulator trap performace qualitatively shown. (left) positron-positron interactions become a viable trapping mechanism. (right) Accumulated positrons fill well sufficiently to inhibit further trapping.

8.2 Accumulator Operation

8.2.1 Accumulator fill phase

Before positrons are accumulated, all the electrodes are grounded, the RW is initialized, the diagnostic digital storage oscilloscopes are armed, and the piezo valve for the CF_4 trapping gas is set to regulate to a base pressure of $\sim 9 \times 10^{-8}$. This gas pressure is sufficient to trap nearly all the incoming positrons. The mean positron lifetime in the trap is $\gtrsim 1000$ s, determined by collecting a set number of positron bursts and measuring the number of positrons remaining after storing for several different times. The trap electrodes are biased to create an electrostatic potential well for confining the positrons. The bias voltage for each electrode is applied using vacuum compatible coaxial cables introduced into the chamber through a multipin UHV feedthrough. The modified quadratic potential well shown in Fig. 8.2 (right) is produced using a resistor divider chain with endcap 2 (EC2) increased to the gate voltage of 90 V.

The best initial trapping efficiency was found for a shallow well, but the accumulation of positrons, and thus space charge, leads to a sharp drop in trapping efficiency as shown in Fig. 8.3 (left). A large space charge, or rather a large trapped positron density, has the benefit of facilitating trapping as positron-positron interactions become a viable trapping mechanism, as shown in the upward inflection of Fig. 8.3 (right). A larger well depth permits a larger total number of positrons to be trapped, but with reduced trapping efficiency. It is preferable to vary the well depth as needed, making it shallow initially to maximize the trapping efficiency of an empty well, and then increasing its depth as positrons are accumulated.

8.2.2 Accumulator store phase

After storing a certain number of positron bursts, limited only by the $\gtrsim$1000 s lifetime, the accumulator switches to the store phase, during which the positron plasma is compressed in proportion to the RW frequency [84]. In order to balance the critical torques resulting from the applied RW and a background drag torque [55, 56], the piezo valve creates a short burst of CF_4. While the CF4 pressure is increasing, the electrostatic potentials of the trap are set to produce a 40 V deep harmonic well using a ring positively biased at 55 V. With enough CF_4 to cool the plasma, one may step the RW frequency and amplitude at known fixed stable points to a final operating point.

8.2.3 Accumulator dump phase

Just before the positrons can be ejected, a series of guiding and correcting magnets are pulsed on, a process described later in Section 9.1. Ejection of positrons from the trap is achieved by a transient potential profile generated by MOSFET pulsers capacitively coupled to each electrode. The amplitude of each pulser is computer controlled so that arbitrary potential profiles can be studied. The profile is defined using 3 parameters: (1) a DC offset 'C'; (2) a linear factor 'B'; and (3) a quadratic term 'A' to provide curvature for temporal bunching. In addition to this, the well depth and shape are adjusted as needed. After a thorough and careful search of the parameter space, two working operating points are saved: (1) a steep ramp given by (A=270 V, B=125 V, C=50 V) resulting in 400 eV positrons in ≤ 4 ns FWHM; and (2) a relatively shallow ramp (A=-80 V, B=200 V, C=60 V) resulting in 150 eV positrons in ~ 8 ns.

After a positron burst is ejected from the accumulator, its behaviour with the rest of the system is measured with destructive diagnostics, that is, the positrons are stopped by certain electrodes and detected by their annihilation photons using a series of gamma-ray detectors placed at critical points, and/or observed on a phosphor screen with a camera (Atik-420 CCD camera). Total positrons numbers were measured using either of the following scintillation detectors: (1) one NaI(Tl) coupled to a photomultiplier tube (PMT); and/or (2) two $PbWO_4$ crystals coupled to a R1924A Hamamatsu MCP-PMT. Positron pulse widths were measured with Lead Fluoride coupled to a single MCP. Gamma-ray detector anode voltages as a function of time were recorded using either of the following digital storage oscilloscopes: (1) LeCroy Waveace 2024; and (2) LeCroy HD4096.

8.3 Accumulator Performance

Surko *et. al.* [23, 168, 83] have done considerable work in defining the operation of high vacuum penning traps and performance of the R.W. technique up to $\sim$ 10MHz with asymmetries of the apparatus being the main cause of R.W. decoupling. Here, a procedure is given to increase coupling of the R.W. to higher frequencies above 100 MHz, with empirical data given to support two separate conditions required for robust operation of the R.W. technique up to and above 100 MHz, with the only apparent limit to this frequency being the Brillouin limit,

$$\omega_B = \frac{\omega_c}{2} = \frac{eB}{2m} \tag{8.1}$$

8.3.1 Plasma stability and rotating wall coupling

Magnetic field homogeneity

The sensitivity of the magnetic field homogeneity on the accumulator R.W. performance warranted the careful production of the main magnet, and it was still necessary to add correction coils about the trap as shown in Fig. 8.1 (right). The quality of field homogeneity is tested by ramping up the RW frequency until RW coupling is lost (gamma-ray or CCD signal), and alignment is varied by adjusting the current through the transverse coils in Fig. 8.1 (right). The working range of transverse coil currents becomes more sensitive for higher RW frequencies as shown in Fig. 8.4 implying that the magnetic field alignment is critical for RW coupling. This 'shrinking island' in parameter space is repeatedly explored as the RW frequency is pushed higher as shown in Fig. 8.5, which shows the density of

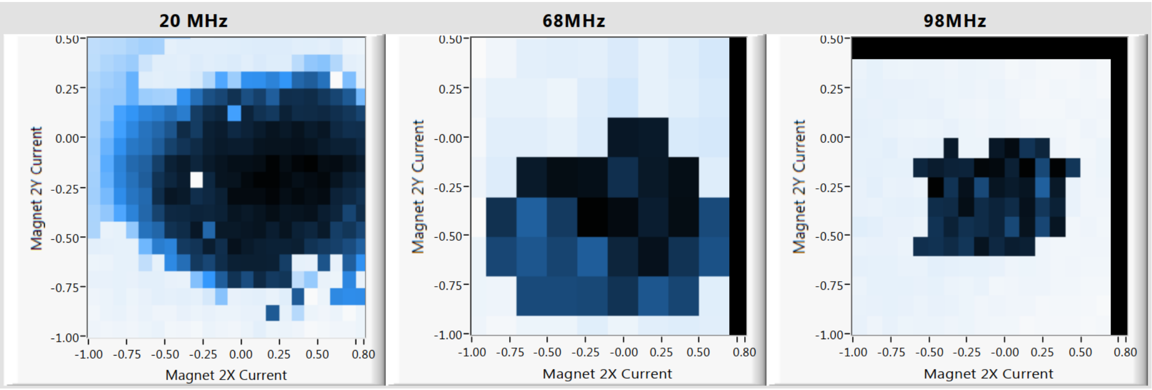

Figure 8.4: Iterative accumulator transverse magnetic field scans showing RW frequency sensitivity (see Fig. 8.5 for frequency scans)

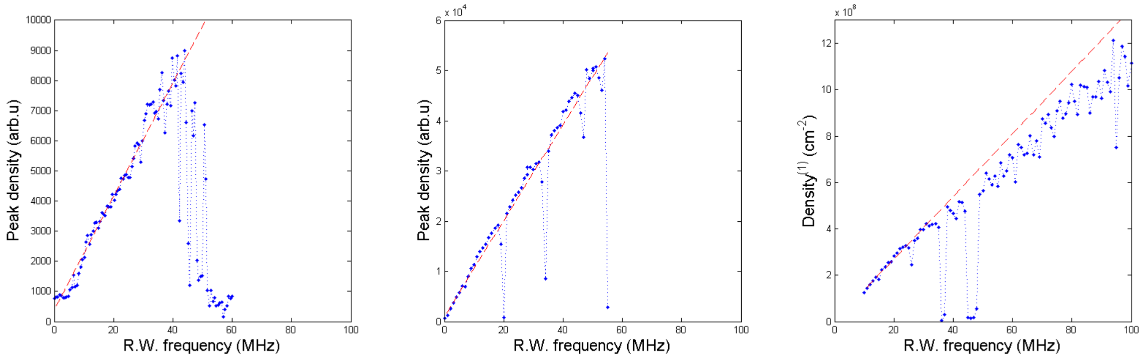

Figure 8.5: RW frequency scans after transverse accumulator magnetic field scan (see Fig. 8.4 for magnetic field scans)

compressed positrons is a function of the RW frequency, with sharp drops caused by the excitation of “zero frequency modes” (ZFM). It was found that the width of the ZFM’s decreases as the magnetic alignment is improved, which implies that the ZFMs have their origin in the asymmetries of the trap, and that they would be nonexistent in a perfect geometry.

Parameters for RW coupling

The de-coupling of the RW at high frequencies has the following critical parameters:

- Magnetic field alignment
- Rotating wall amplitude
- Number of positrons in trap
- Cooling gas pressure

The relationship between the RW amplitude and the number of positrons within the trap (see Fig. 8.6) has been investigated at higher frequencies where the is a more restrictive parameter space for optimal RW coupling. The linear increase in the number of positrons counted with number of positrons captured is totally expected, but the increase in the positron density needs an explanation. We model this effect by saying that as positrons fill the harmonic well, additional positrons not only build up radially, but also longitudinally and this fact leads to the increased 2D density of positrons impinging the phosphor screen. This is especially true when the well is initially loaded. RW coupling performance is defined using by both the total number of positrons compressed and the density of the compressed positrons transmitted. The three cross-over regions are: (1) RW coupling upon increasing number of positrons; (2) RW coupling upon increasing the RW amplitude; and (3) the RW de-coupling as the number of positrons and RW amplitude are increased. The first two show slightly increased positron density, thus increased RW coupling, as the number of positrons or the RW amplitude is increased until there is a sudden change, likely a transition to

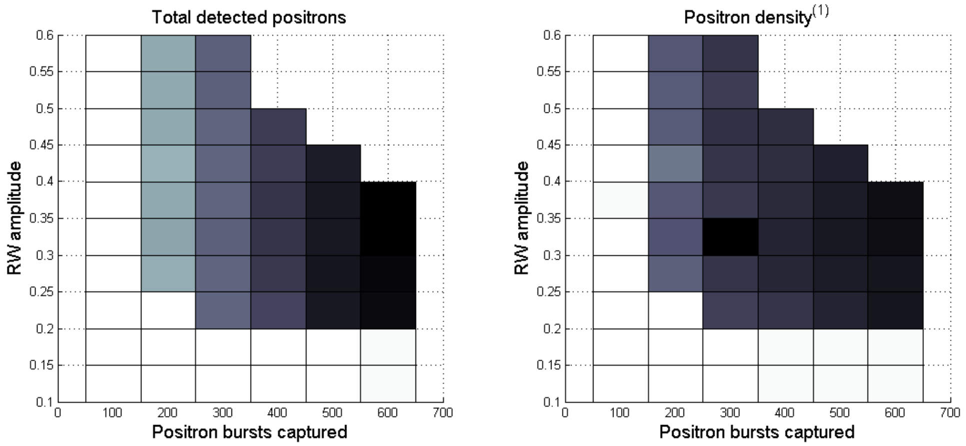

Figure 8.6: Rotating wall performance measured by total detected positrons (left) and ejected positron plasma density (right) for different RW amplitude/plasma size varied by (1) changing the number of positrons captured; and (2) directly changing the RW amplitude.

the 'strong-drive' regime [55]. Studying the first two cross-over regions revealed a relation between plasma size determined by the RW frequency and number of positrons collected, and the RW amplitude meaning that the potential across the plasma diameter is one of the key critical parameters. Therefore, the magnitude of the magnetic field containing the plasma is of importance too and should be carefully examined.

One might think that to achieve much higher densities, one simply needs to greatly increase the rotating wall amplitude and increase the number of charged particles in the trap, but the third cross-over region shows otherwise, and is peculiar in that beyond it, the density of transmitted positron bursts is roughly constant. Of particular note is the shape of this, and a possible explanation is overheating of the plasma by the RW. Overheating of plasma is mitigated by the introduction of more cooling gas as previously described and this warrants a repeat measurement of the RW coupling with different cooling gas pressures. Both shapes of regions one and two, and region 3 should be carefully resolved by the interested researcher for a relationship between RW amplitude and plasma size as previously mentioned.

8.4 Conclusion: Record Rotating Wall Operation

The aforementioned procedure for optimizing RW performance for a high vacuum Penning-Malmberg trap for the confinement and compression of a single-component positron plasma was followed at the time of writing this to recover high RW frequency coupling with a record RW frequency of 106 MHz ($\sim 12.5\%$ of the Brillouin limit) to compress $\sim 8 \times 10^7$ positrons to ~ 2 mm FWHM measured just after magnetic field extraction. See Chapter 9 for details following ejection of accumulated positrons.

Chapter 9

High Instantaneous Positron Current Density Experiments

A device to accumulate, compress and bunch large numbers of positrons from a positron trap for producing a high density, short duration positron pulse is described in Chapter 8. Following ejection of positrons, a pulsed positron buncher-accelerator (see Chapter 4) is used with magnetic field termination for creating a magnetic field-free positron burst focused by an optical column resulting in a high instantaneous positron current density suitable for exploring positron-positron or positronium-positronium physics. Applications include the creation of Bose-Einstein condensates of positronium atoms and the production and spectroscopy of positive positronium ions.

9.1 Transport to Target Chamber

The system shown in Fig. 9.1 is designed to magnetically transport positrons ejected from the accumulator to a buncher-accelerator, where they are extracted from a magnetic field, and subsequently focused in a target chamber. Recently, the following addition immediately after E(right) acts as a useful diagnostic stage: a 2.75” Conflat rounded 6-way cube where the diagnostic phosphor screen mounted on a 2” linear motion translator is viewed by a CCD via a mirror. There are two more phosphor screens, installed within the target chamber on target slides discussed later in Section 9.3.2. The system is pumped on by two 1000 l/s cryopumps, one on either end of the system pictured in Fig. 9.1. Six sets of transverse magnets used to correct for stay magnetic fields are numbered and located at the following locations: (1) before the cross located at ‘A’ to center positron trajectories on the positron plasma within the accumulator; (2) around the main magnet of the accumulator at location ‘C’ (also depicted in Fig. 8.1 (right)); (3) affixed to a short electromagnet before the buncher-accelerator located at ‘D’ and ‘E’ to center positrons within the inlet of the buncher-accelerator; (4) contained within the mu-metal shield of the buncher-accelerator at ‘D’ and ‘E’ to center positrons on the terminating plate for magnetic field extraction; (5) about the 6-way cube attached immediately after the buncher-accelerator to center positrons on the center of the target; and (6) large magnets about the target chamber to eliminate Earth’s magnetic field within the target chamber.

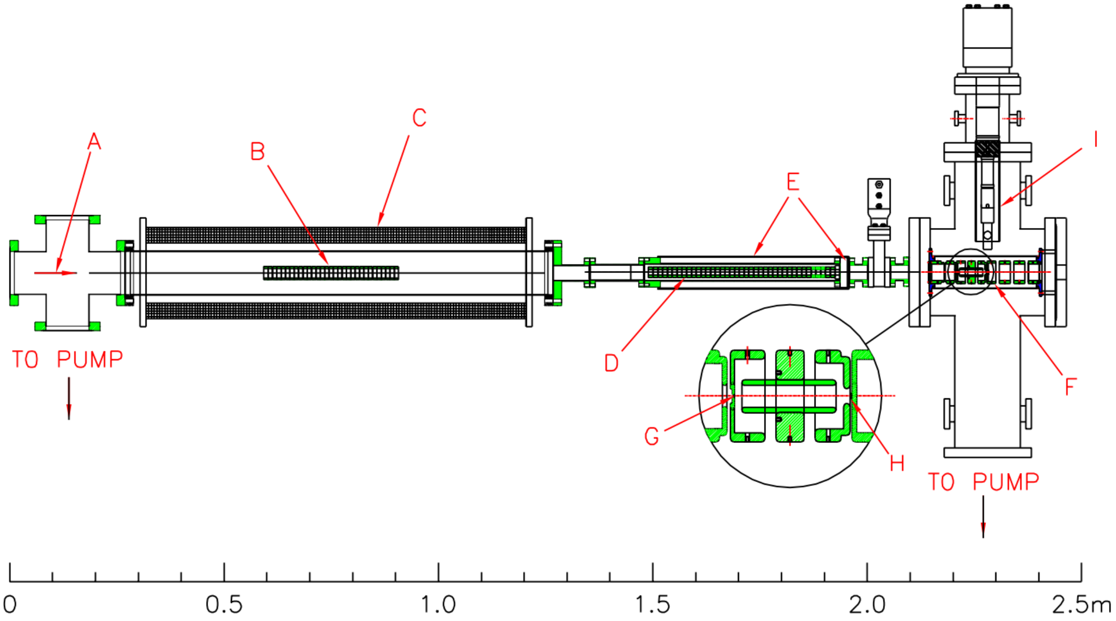

Figure 9.1: Preliminary schematic of experiments involving dense positron bursts.

9.2 Magnetic Field Extraction

Positrons ejected from the accumulator are centered on the inlet of the buncher-accelerator using a similar routine discussed in Section 3.3, and then the timing for the bunching-accelerator is set to fire just as all positrons have entered the bunching section described in Section 4. Positrons are accelerated, ejected through a 'spider' in the terminating plate, and can be imaged in the diagnostic screen. The spider should subdivide the extraction holes to those with smaller characteristic size thus reducing the non-adiabatic impulse effects imparted on positrons passing to a field free environment leading to an observed relative increase in beam brightness of about a factor of 3 as described by Hurst [93]. Hurst goes on to explain that performance is increased when charged particles are removed from a lower magnetic field and smaller radii. This trend is observed here and is displayed

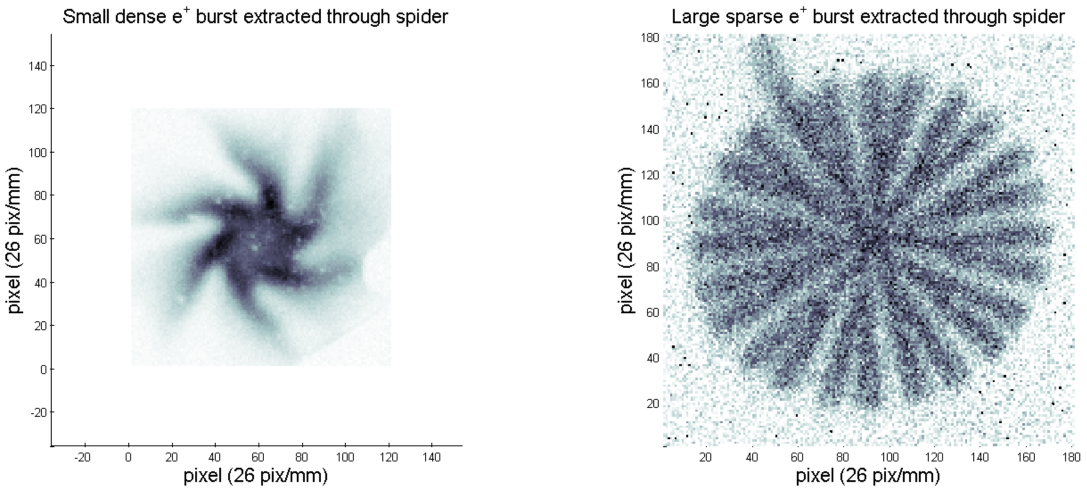

Figure 9.2: Positron burst imaged on a diagnostic phosphor screen immediately after magnet field extraction.

in Fig. 9.2 for a dense collection of positrons extracted when the terminated field measures $\sim$ 150 Gauss (left) and a sparse collection of positrons extracted when the magnetic field terminated is $\sim$ 20 Gauss (right). The notch in the top left of the latter is from the wire cutting tool used to machine the tines of the spider within the 2 mm thick mu-metal and after cutting, the spider was annealed in a hydrogen furnace.

9.3 Focusing of Dense 5 keV Field Free Positrons

9.3.1 Magnetic dipole

Following magnetic field extraction, positrons pass through a magnetic dipole lens held concentric with the vacuum system via spacers. Originally, the magnetic lens was scatter wound on a large 4.5” form and was later upgraded to a compact $\sim$ 2” coil encased in a mu-metal yoke. The high permeability mu-metal makes the extending field terminate

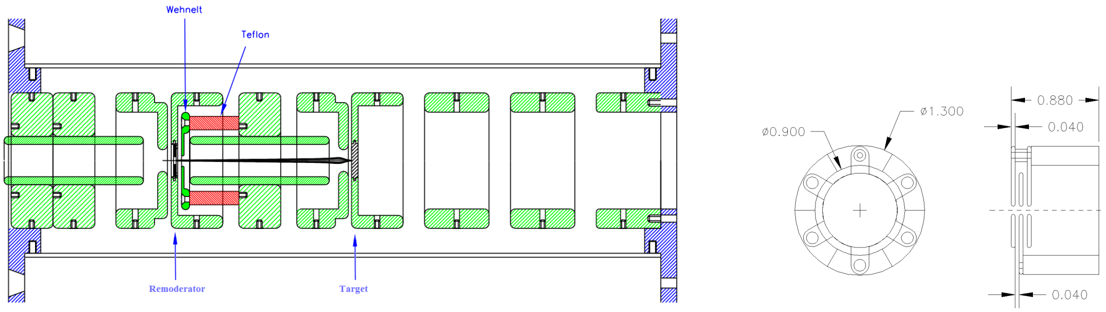

Figure 9.3: Electrostatic optical column (left). Wehnelt lens upgrades to compact Einzel lens mounted on Macor form shown at right.

rapidly and thus negative effects such as movement of the focused beam were greatly reduced. The magnetic lens focused the roughly 4 mm FWHM positron burst down to ≤1 mm at a phosphor screen located at the remoderator location, ∼ 10" away, shown in Fig. 9.1 (G).

9.3.2 Electrostatic column

The final focus is performed with the electrostatic column schematically shown in and Fig. 9.3; Fig. 9.1 depicts the original design. The most advanced configuration includes and Einzel lens mounted on a Macor support (Fig. 9.3 (right)) placed ∼ 1 mm from the remoderator replacing the Wehnelt extraction lens (Fig. 9.3 (left)). The Macor support is machined to just fit within the remoderator electrode holder and Einzel elements concentrically positioned precisely with a rod. The optical column electrodes are held fixed in place with eight insulating alumina rods and assembled with removable precision (±0.0005") aluminum spacers. When fully assembled, the optical column is mounted on the back flange of the target chamber (right side of Fig. 9.1), and then slides onto alignment pins as the flange is attached to the target chamber.

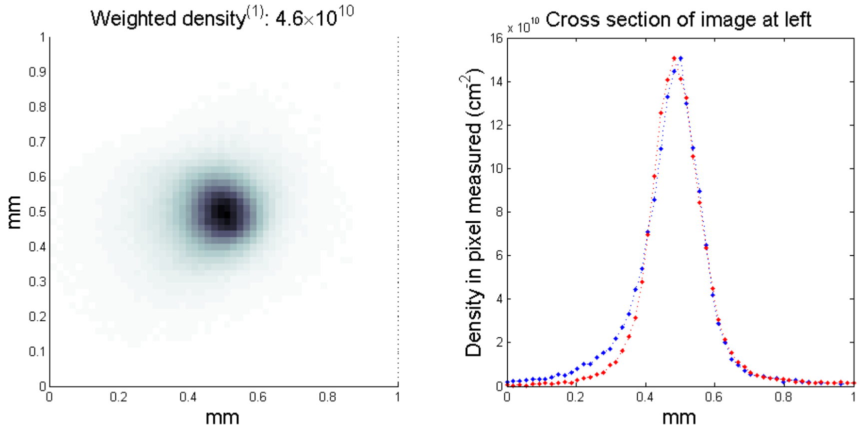

Figure 9.4: $\sim 5 \times 10^7$ positrons focused at the magnetic field free remoderator location to a peak density of $\sim 1.5 \times 10^{11}$ cm^{-2}

9.4 High Current Density experiments

5 keV positrons extracted from a magnetic field are focused slightly by a magnetic dipole lens such that the optimally filled electrostatic lens focuses the 4 ns burst of $\sim 5 \times 10^7$ positrons to a peak density of $\sim 1.5 \times 10^{11}$ cm^{-2} (see Fig. 9.4) onto a phosphor screen approximately located where a Ni foil will be placed. Not only is this a new record, but this is also achieved in a field free environment, and the corresponding instantaneous current density is ~ 6.25 A cm^{-2}. The profile is nearly gaussian, and is slightly skewed. This could be reduced by more careful alignment of the positron burst on the electrostatic lens.

9.4.1 Positron number from ACAR detector

The following section, Section 9.4.1, is the result from a private communication with Professor Allen Mills Jr.

One method of measuring the number of positrons contained in a large burst is to first implant the positrons onto a clean metal, such as stainless steel to make the production of triplet positronium negligible, and detect the following gamma rays -or rather the lack thereof. The distribution of the number of gamma rays detected follows Poisson statistics and the number of positrons can be measured from the zero counts frequency if the detector is placed sufficiently far away. Most gamma ray counting detectors require careful calibration, but the benefit of this method is the minimal calibration needed. Estimates of the detection efficiency (ε_γ), positronium production (ε_{Ps}), effective solid angle of collected annihilation gamma rays ($\Delta\Omega/2\pi$), where the 2π takes into account the two co-linear gamma rays resulting from singlet Ps annihilation, and attenuation of annihilation gamma rays (ε_μ) is needed.

Poisson statistics states that the probability of getting 'k' counts from a pulse yielding a mean number of counts λ is

$$P(k) = \frac{\lambda^k e^{-\lambda}}{k!} \tag{9.1}$$

The probability of getting zero counts detected (null counts) in a burst from 9.1 is $P_\lambda(0) = e^{-\lambda}$ and thus the mean counts detected by the gamma ray detector in that configurations is $\lambda = -ln[P_\lambda(0)]$, and the number of positrons (N_p) contained within the full burst is

$$N_p = \frac{2\pi}{\Delta\Omega(\Pi\varepsilon_i)}\lambda = \frac{2\pi}{\Delta\Omega(\Pi\varepsilon_i)}\{-ln[P_\lambda(0)]\} \tag{9.2}$$

The error in the measurement $\Delta\lambda/\lambda$ is found by considering the number of null counts in a series of 'N' bursts, a binomial distribution resulting in the chance of getting 'k' null counts ($p_0 = P_\lambda(0)$) in N is:

$$P_k^N = \frac{N!}{(N-k)!k!} p_0^k (1-p_0)^{N-k} \tag{9.3}$$

The binomial distribution defines the expected value of k, ($\langle k \rangle = Np_0$), and thus $\frac{\partial \langle k \rangle}{\partial \lambda} = -\langle k \rangle$. Since $\Delta k = \sqrt{Np_0(1-p_0)}$,

$$\Delta\lambda = \frac{\Delta k}{\partial k/\partial\lambda} = \frac{\sqrt{(1-p_0)/p_0}}{\sqrt{N}} \tag{9.4}$$

$$\frac{\Delta\lambda}{\lambda} = \frac{\sqrt{(1-p_0)/p_0}}{ln(p_0)\sqrt{N}} \tag{9.5}$$

with a minimum uncertainty for $p_0 = P_\lambda(0) \approx 0.20$, $\lambda = -ln[P_\lambda(0)] \approx 1.59$ of $\frac{\Delta\lambda}{\lambda} = \frac{1.24}{\sqrt{N}}$ which for the ACAR detector described in Section 6 results in a minimum relative uncertainty $\frac{\Delta\lambda}{\lambda} \approx 6\%$ for every positron burst measured.

9.4.2 Spin polarization measurement

To measure, and thereby test the focusing performance of the apparatus described herein, the spin polarization of the positrons resulting from a Ta-backed ^{22}Na source, the delayed fraction, a metric estimating the relative amount of triplet Ps produces as described by Cassidy *et. al.* [29], is recorded as the density of positrons implanted into a porous Ps producing target as previously done by Cassidy *et. al.* [39]. Here (see Fig. 9.5), the density is varied by adjusting the focusing voltage of the electrode just before the remoderator electrode as shown in Fig. 9.3. The Ps producing target was a Pd capped silica composite made by sputtering a SiO_2 on a Si wafer with diameter measuring $\sim$ 1/2". The results were a low density delayed fraction measurement of $16.6 \pm 1.9\%$ and a spin-polarization of $27.6 \pm 2.3\%$, in agreement with that of Cassidy's [39] of $28 \pm 1\%$. This measurement was

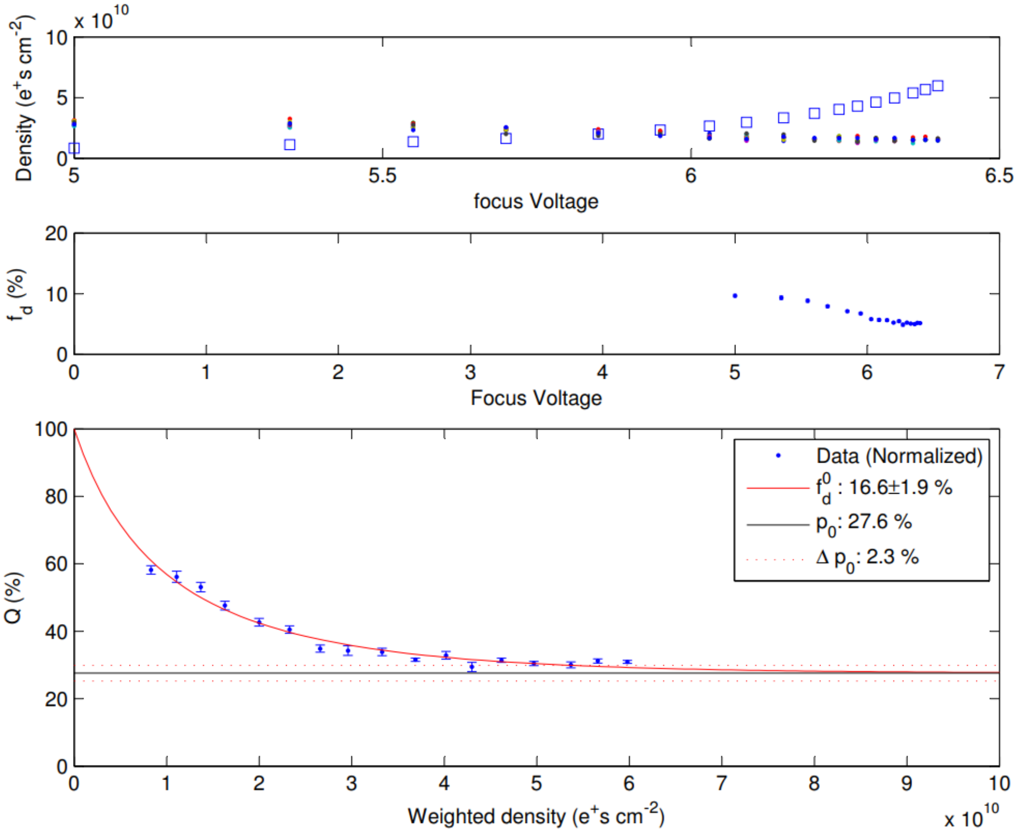

Figure 9.5: Spin-polarization measurement performed in a field free region

repeated by fixing the density using the RW technique as done previously [39] with similar results again.

9.4.3 Positron remoderation

The penultimate goal of high density positron experiments is the production of a Ps BEC, however the current state of the apparatus will not yield to Ps condensing. The next stage, as schematically shown in Fig. 9.3, is used to extract and refocus positrons onto a second target, a process known as brightness enhancement [134]. The first target is replaced with a Ni(100) foil 100 nm thick held in place by a 12 mm Ni retainer produced by Aarhus University. The model for preparing the Ni foil is described by Krupyshev [112].

Ni foil preparation makes use of cylindrical ceramic furnace heated with resistive wire. This style heater is used in the target chamber *in situ* and in an annealing chamber. The annealing chamber is a clean ultra-high-vacuum chamber with a high-purity Hydrogen inlet, and throttled pumps permitting H_2 flow rates of $\gtrsim$ 10 SCCM. Before using the ceramic heaters, it is critical to treat the ceramic heater as a reaction of SiO_2 in H_2 at high temperatures has been shown [125]. The annealing procedure described by Krupushev is as follows:

- The cylindrical ceramic oven is heated to 600 C over 15 min.
- The temperature is held constant for 15 min.
- The temperature is slowly reduced to 200 over an hour.
- the H_2 is pumped out and the Ni is allowed to cool while the target chamber is prepared.

Once the target chamber is prepared for installation of the remoderator, the Ni remoderator is quickly installed in a sample slide and held in place with a retaining spring. The remoderator efficiency is $\lessapprox$2%. The foil requires conditioning to increase remoderation efficiency. First the cylindrical heater is conditioned by heating to temperatures above the Ni conditioning temperature of 350 C or 550 C with the Ni foil inserted into the optical column. The Ni foil is inserted into the cylindrical oven for *in situ* conditioning at 350 C resulting in a peak effective remoderation efficiency of $\lessapprox$10%. Efficiency measured is the ratio of total intensity on a phosphor screen located at the target location (see Fig. 9.3) for the incoming 5 keV positron beam and for the remoderated beam. As of August 13^{th}, 2021, this was $(2.124 \pm 0.008) \times 10^6$ and $(191.3 \pm 2.4) \times 10^3$ respectively, or 9%.

The accumulated pulses of $\sim 1.5 \times 10^7$ positrons are compressed with a RW frequency of 40 MHz, accelerated and removed from the guiding magnetic field, brightness enhanced with 9% efficiency, and finally focused to an areal density of $\sim 8{\times}10^9$ e^+ cm^{-2} on a target. With improvements to electrostatic focusing and improvements to remoderator preparation, densities over 5×10^{11} cm^{-2} should be attainable. When the incoming density has been increased by $\sim$ 5x, an option shown in Chapter 8, the final positron densities should be sufficient to produce a Ps BEC at $T \leq 50$ K,

Chapter 10

Conclusions

The pulsed positron beam-line described herein moderates positrons from a sealed ^{22}Na source using solid Ne [142] slowly deposited onto a cold ~ 8 K Cu cone with 0.4% effective efficiency. Then $\sim 5 \times 10^5$ positrons collected in a Penning-Surko style two-stage buffer gas trap [169, 82] are ejected at a rep rate of 2 Hz. Several positron beam manipulation devices were thus developed. An achromatic Rydberg positronium (Ps) mirror [102, 103] with $\sim$ 7:1 signal enhancement focused Ps atoms to ~ 32 mm Full-Width Half-Max (FWHM) 6 m away onto another recently developed device, a resistive-anode based position sensitive Rydberg atom detector with 1.4 ± 0.1 mm FWHM positional resolution and ~ 1 ns temporal discrimination of events. A focusing lens was developed to focus positron bursts to $\lessapprox$0.3 mm a distance in a field free region showed great linearity in deflecting the positron burst up to ~ 1 mm without broadening of the focused positron spot size.

Development of a magnetic switch-yard to route positrons to one of three experimental stages resulted in alignment and temporal bunching procedures developed to transport bursts of 5×10^5 positrons spatio-temporally bunched such that $\sim 100\%$ of the particles were recaptured and trapped in a high vacuum positron accumulator. It was found that electromagnetic field alignment and uniformity, along with the cooling gas pressure and balancing of the rotating wall (R.W.) amplitude with the stored plasma size, was critical for high performance coupling of the RW in compressing the stored positron plasma in the "strong drive" regime [55, 56]. The result being a new record in RW driving frequencies $\gtrsim$100 MHz.

The compressed positron plasma ejected from the accumulator has a temporal width of $\sim$ 4 ns FWHM before entering a high voltage buncher accelerator designed to further spatio-temporally bunch the positrons before accelerating to $\sim$ 5 keV and extracting the charged particles from a low $\sim$ 25 gauss central magnetic field through a high permeability mu-metal spider [93]. In this way, magnetic field extraction reduced the negative effects from non-adiabatic impulses from magnetic field extraction and resulted in a brightness increase of slightly less than a factor of two. The dense field free positron plasma is electrostatically focused to a record peak density of $\sim 1.5 \times 10^{11}$ cm^{-2} and a record instantaneous current density of $\sim$ 6.25 A cm^{-2} in a target chamber centered between a detector for positronium temperature measurements via angular correlation of annihilation [43]. At such densities positron-positron and Ps-Ps interaction mechanisms are observed and after remoderation, or brightness enhancement [134], the subsequent positron density will be sufficient to: (1) produce detectable positronium-plus ions; and (2) deposit enough positrons into a target capable of rapidly cooling and Bose-Einstein condensing Ps.

Bibliography

[1] 3M Optical Systems. *Vikuiti$^{\circledR}$ Enhanced Specular Reflector (ESR)*, 2017.

[2] Gregory S. Adkins, Richard N. Fell, and Plamen M. Mitrikov. Calculation of the positronium hyperfine interval using the bethe-salpeter formalism. *Physical Review A*, 65(4):042103, mar 2002.

[3] F. Anderegg, E. M. Hollmann, and C. F. Driscoll. Rotating field confinement of pure electron plasmas using trivelpiece-gould modes. *Phys. Rev. Lett.*, 81:4875–4878, Nov 1998.

[4] Carl D. Anderson. The positive electron. *Physical Review*, 43(6):491, 1933.

[5] Carl D. Anderson and Seth H. Neddermeyer. Positrons from gamma-rays. *Physical Review*, 43(12):1034–1034, 1933.

[6] M. H. Anderson, J. R. Ensher, M. R. Matthews, C. E. Wieman, and E. A. Cornell. Observation of Bose-Einstein condensation in a dilute atomic vapor. *Science*, 269(5221):198, Jul 14 1995.

[7] A.A Annenkov, M.V Korzhik, and P Lecoq. Lead tungstate scintillation material. *Nucl. Instrum. Meth. A*, 490(1–2):30 – 50, 2002.

[8] W. M. Augustyniak, W. L. Brown, and H. P. Lie. A hybrid approach to two dimensional charged particle position sensing preserving energy resolution. *IEEE Transactions on Nuclear Science*, 19(3):196–200, 1972.

[9] H. K. Avetissian, A. K. Avetissian, and G. F. Mkrtchian. Gamma-ray laser based on the collective decay of positronium atoms in a bose-einstein condensate. *Phys. Rev. A*, 92(2):023820, August 2015.

[10] Vanderlei Bagnato and Daniel Kleppner. Bose-Einstein condensation in low-dimensional traps. *Phys. Rev. A*, 44:7439–7441, Dec 1991.

[11] J. Baudot, W. Dulinski, M. Winter, R. Barbier, E. Chabanat, P. Depasse, and N. Estre. Photon detection with CMOS sensors for fast imaging. *Nuclear Instruments and Methods in Physics Research Section A: Accelerators, Spectrometers, Detectors and Associated Equipment*, 604(1-2):111–114, jun 2009.

[12] R. E. Bell and R. L. Graham. Time distribution of positron annihilation in liquids and solids. *Phys. Rev.*, 90(4):644–654, May 1953.

[13] Robert Beringer and C. G. Montgomery. The angular distribution of positron annihilation radiation. *Phys. Rev*, 61(5):222–224, 1942.

[14] S Berko, M Haghgooie, and JJ Mader. Momentum density measurements with a new multicounter two-dimensional angular correlation of annihilation radiation apparatus. *Phys. Lett. A*, 63:335–338, 1977.

[15] S. Berko and J. Mader. Momentum density measurements by positron annihilation in metals and alloys recent experiments with a multicounter two-dimensional angular correlation apparatus. *Applied Physics*, 5(4):287–306, jan 1975.

[16] I. I. Beterov, D. B. Tretyakov, I. I. Ryabtsev, V. M. Entin, A. Ekers, and N. N. Bezuglov. Ionization of rydberg atoms by blackbody radiation. *New J. Phys.*, 11:013052, 2009.

[17] Hans A Bethe and Edwin E Salpeter. *Quantum mechanics of one-and two-electron atoms.* Springer Science & Business Media, 2012.

[18] John B Birks. The theory and practice of scintillation counting vol. 27, international series of monographs on electronics and instrumentation, 1964.

[19] H Boersch, H Hamisch, and W Ehrlich. Surface discharge through an insulator in a vacuum. In *International Electromicroscopy Conference*, 1985.

[20] George R. Brandes, K. Canter, A. Krupyshev, R. Xie, and Allen P. Mills. *Diamond Field-Assisted Moderator.* PhD thesis, Brandeis University, 2000.

[21] Werner Brandt, Gérard Coussot, and Robert Paulin. Positron annihilation and electronic lattice structure in insulator crystals. *Physical Review Letters*, 23(10):522–524, sep 1969.

[22] Thomas Breeden and Harold Metcalf. Stark acceleration of rydberg atoms in inhomogeneous electric fields. *Phys. Rev. Lett*, 47(24):1726–1729, December 1981.

[23] M. Leventhal C. M. Surko and A. Passner. Positron plasma in the laboratory. *Phys. Rev. Lett*, 62(8):901–904, 1989.

[24] K. F. Canter, A. P. Mills, Jr., and S. Berko. Efficient positronium formation by slow positrons incident on solid targets. *33*, 33(1):7–10, 1974.

[25] K. F. Canter, A. P. Mills, Jr., and S. Berko. Observations of positronium Lyman-α radiation. *Phys. Rev. Lett.*, 34(4):177–180, 1974.

[26] KF Canter, PG Coleman, TC Griffith, and GR Heyland. Measurement of total cross sections for low energy positron-helium collisions.(positron backscattering from metal surface). *Journal of Physics B: Atomic and Molecular Physics*, 5(8):L167, 1972.

[27] J. P. Carbotte and H. L. Arora. Thermalization time of positrons in metals. *Can. J. Phys.*, 45(2):387–402, 1967.

[28] J. D. Carter and J. D. D. Martin. Energy shifts of rydberg atoms due to patch fields near metal surfaces. *Physical Review A*, 83(3):032902, mar 2011.

[29] D. B. Cassidy, S. H. M. Deng, R. G. Greaves, T. Maruo, N. Nishiyama, J. B. Snyder, H. K. M. Tanaka, and A. P. Mills, Jr. Experiments with a high-density positronium gas. *Phys. Rev. Lett.*, 95:195006, Nov 2005.

[30] D. B. Cassidy, S. H. M. Deng, R. G. Greaves, and A. P. Mills, Jr. Accumulator for the production of intense positron pulses. *Review of Scientific Instruments*, 77:073106, 2006.

[31] D. B. Cassidy, S. H. M. Deng, R. G. Greaves, and A. P. Mills, Jr. Accumulator for the production of intense positron pulses. *Review of Scientific Instruments*, 77(7), 2006.

[32] D. B. Cassidy, T. H. Hisakado, V. E. Meligne, H. W. K. Tom, and A. P. Mills, Jr. Delayed emission of cold positronium from mesoporous materials. *Phys. Rev. A*, 82:052511, 2010.

[33] D. B. Cassidy, T. H. Hisakado, H. W. K. Tom, and A. P. Mills. Efficient production of rydberg positronium. *Physical Review Letters*, 108(4):043401, jan 2012.

[34] D. B. Cassidy, T. H. Hisakado, H. W. K. Tom, and A. P. Mills, Jr. Laser excitation of positronium in the Paschen-Back regime. *Phys. Rev. Lett.*, 106:173401, Apr 2011.

[35] D. B. Cassidy, T. H. Hisakado, H. W. K. Tom, and A. P. Mills, Jr. New mechanism for positronium formation on a silicon surface. *Phys. Rev. Lett.*, 106:133401, 2011.

[36] D. B. Cassidy, T. H. Hisakado, H. W. K. Tom, and A. P. Mills, Jr. Positronium formation via excitonlike states on si and ge surfaces. *Phys. Rev. B*, 84:195312, 2011.

[37] D. B. Cassidy, T. H. Hisakado, H. W. K. Tom, and A. P. Mills, Jr. Efficient production of rydberg positronium. *Phys. Rev. Lett.*, 108:043401, 2012.

[38] D. B. Cassidy, T. H. Hisakado, H. W. K. Tom, and A. P. Mills, Jr. Excitonic positronium emission from n-si(111). *Phys. Rev. B*, 86:155303, 2012.

[39] D. B. Cassidy, V. E. Meligne, and A. P. Mills, Jr. Production of a fully spin-polarized ensemble of positronium atoms. *Phys. Rev. Lett.*, 104:173401, Apr 2010.

[40] D. B. Cassidy and A. P. Mills, Jr. The production of molecular positronium. *Nature*, 449:195–197, 2007.

[41] F. Castelli. The positronium atom as a benchmark for rydberg excitation experiments in atomic physics. *Eur. Phys. J. Special Topics*, 203:137–150, 2012.

[42] F. Castelli, I. Boscolo, S. Cialdi, M. G. Giammarchi, and D. Comparat. Efficient positronium laser excitation for antihydrogen production in a magnetic field. *Phys. Rev. A*, 78(5):052512, 2008.

[43] G. G. Cecchini, A. C. L. Jones, M. Fuentes-Garcia, D. J. Adams, M. Austin, E. Membreno, and A. P. Mills. Detector for positronium temperature measurements by two-photon angular correlation. *Review of Scientific Instruments*, 89(5):053106, may 2018.

[44] S. D. Chao, M. Hayashi, S. H. Lin, and E. W. Schlag. On the electric field effect on the dynamics of high rydberg states of hydrogen atom and the model of zeke spectroscopy. *J. Chin. Chem. Soc.*, 45(4):491–501, 1998.

[45] G. Chardin. Graviation, c, p and t symmetries and the second law. *AIP Conf. Proc.*, 643:385–390, 2002.

[46] M. Charlton. Antihydrogen production in collisions of antiprotons with excited states of positronium. *Phys. Lett. A*, 143(3):143–146, 1990.

[47] D. M. Chen, S. Berko, K. F. Canter, K. G. Lynn, A. P. Mills, L. O. Roellig, P. Sferlazzo, M. Weinert, and R. N. West. Angle-resolved positronium emission spectroscopy. *Physical Review Letters*, 58(9):921–924, mar 1987.

[48] William H Cherry. *Secondary Electron Emission Produced from Surfaces by Positron Bombardment.* PhD thesis, Princeton University, 1958.

[49] Steven Chu, Allen P. Mills, and John L. Hall. Measurement of the positronium1s13-2s13interval by doppler-free two-photon spectroscopy. *Physical Review Letters*, 52(19):1689–1692, may 1984.

[50] ML Citron, HR Gray, C Wi Gabel, and CR Stroud Jr. Experimental study of power broadening in a two-level atom. *Phys. Rev. A*, 16(4):1507, 1977.

[51] DG Costello, DE Groce, DF Herring, and J Wm McGowan. Evidence for the negative work function associated with positrons in gold. *Physical Review B*, 5(4):1433, 1972.

[52] S. M. Curry. Combined zeeman and motional stark effects in the first excited state of positronium. *Phys. Rev. A*, 7(2):447–450, 1973.

[53] Andrzej Czarnecki, Kirill Melnikov, and Alexander Yelkhovsky. Positronium hyperfine splitting: Analytical value atO(m6). *Physical Review Letters*, 82(2):311–314, jan 1999.

[54] Andrzej Czarnecki, Kirill Melnikov, and Alexander Yelkhovsky. PositroniumS-state spectrum: Analytic results atO(m6). *Physical Review A*, 59(6):4316–4330, jun 1999.

[55] J. R. Danielson and C. M. Surko. Torque-balanced high-density steady states of single-component plasmas. *Phys. Rev. Lett*, 94(3):035001, January 2005.

[56] J. R. Danielson, C. M. Surko, and T. M. O'Neil. High-density fixed point for radially compressed single-component plasmas. *Phys. Rev. Lett*, 99(13):135005, September 2007.

[57] D. J. Day, M. Charlton, and G. Laricchia. On the formation of excited state positronium in vacuum by positron impact on untreated surfaces. *J. Phys. B*, 34(18):3617–3628, 2001.

[58] S. DeBenedetti, C. E. Cowan, W. R. Konneker, and H. Primakoff. On the angular distribution of two-photon annihilation radiation. *Phys. Rev.*, 77:205–212, Jan 1950.

[59] A. Deller, A. M. Alonso, B. S. Cooper, S. D. Hogan, and D. B. Cassidy. Measurement of rydberg positronium fluorescence lifetimes. *Physical Review A*, 93(6):062513, jun 2016.

[60] Martin Deutsch. Evidence for the formation of positronium in gases. *Physical Review*, 82(82):455–456, May 1951.

[61] Martin Deutsch. Three-quantum decay of positronium. *Physical Review*, 83(83):866–867, May 1951.

[62] Martin Deutsch and Sanborn C. Brown. Zeeman effect and hyperfine splitting of positronium. *Physical Review*, 85(6):1047–1048, mar 1952.

[63] Martin Deutsch and Everett Dulit. Short range interaction of electrons and fine structure of positronium. *Phys. Rev.*, 84(3):601–602, November 1951.

[64] R. H. Dicke. The effect of collisions upon the Doppler width of spectral lines. *Phys. Rev.*, 89:472–473, Jan 1953.

[65] P. A. M. Dirac. On the annihilation of electrons and protons. In *Mathematical Proceedings of the Cambridge Philosophical Society*, volume 26, pages 361–375, 1930.

[66] Dow Corning Corporation. *Sylgard® 184 Silicone Elastomer*, 2007.

[67] J. W. M. Dumond, D. A. Lind, and B. B. Watson. Precision measurement of the wavelength and spectral profile of the annihilation radiation from cu^{64} with the two-meter focusing curved crystal spectrometer. *Phys. Rev.*, 75(8):1226–1239, 1949.

[68] Dhanadeep Dutta, Jeremy I. Feldblyum, David W. Gidley, James Imirzian, Ming Liu, Adam J. Matzger, Richard S. Vallery, and Antek G. Wong-Foy. Evidence of positronium bloch states in porous crystals ofZn4o-coordination polymers. *Physical Review Letters*, 110(19):197403, may 2013.

[69] P. O. Egan, W. E. Frieze, V. W. Hughes, and M. H. Yam. Positronium: Precision determination of the ground-state fine-structure interval δv, and measurement of the density shifts in the noble gases. *Phys. Lett.*, 54A(5):412–414, 1975.

[70] Eljen Technology. *Fast Timing Plastic Scintillator EJ-228, EJ-230*, 2016.

[71] John W. Farley and William H. Wing. Accurate calculation of dynamic stark shifts and depopulation rates of rydberg energy levels induced by blackbody radiation. hydrogen, helium, and alkali-metal atoms. *Physical Review A*, 23(5):2397–2424, may 1981.

[72] R Ferragut, A Dupasquier, A Calloni, G Consolati, F Quasso, M P Petkov, S M Jones, A Galarneau, and F Di Renzo. Homogeneous porous silica for positronium production in AEGIS. *J. Phys. Conf. Ser.*, 262(1):012020, 2011.

[73] Richard A Ferrell. The positronium fine structure constant. *Physical Review*, 84(4):858, 1951.

[74] G.W. Fraser and E. Mathieson. Signal location by uniform resistive anodes. *Nuclear Instruments and Methods*, 179(3):591–604, feb 1981.

[75] GW Fraser and E Mathieson. Signal location using resistive anodes of gear's design. *Nuclear Instruments and Methods*, 180(2-3):597–601, 1981.

[76] W. E. Frieze, D. W. Gidley, and K. G. Lynn. Positron-beam-brightness enhancement: Low-energy positron diffraction and other applications. *Phys. Rev. B*, 31:5628–5633, May 1985.

[77] G. G. Cecchini et al. Interaction of positron beams with surfaces, thin films, and interfaces. *Review of Scientific Instruments, submitted 2017*, 2017.

[78] CW Gear. Graphcs ins a time sharing environment. In *Proc. for the Skytop Conf. on Computer System in Experimental Nuclear Phys., 1969*, 1969.

[79] D. Gerola, W. B. Waeber, M. Shi, and S. J. Wang. Quasidivergency-free extraction of a slow positron beam from high magnetic fields. *Rev. Sci. Instrum.*, 66(7):3819–3825, 1995.

[80] David W. Gidley, Hua-Gen Peng, and Richard S. Vallery. POSITRON ANNIHILATION AS a METHOD TO CHARACTERIZE POROUS MATERIALS. *Annual Review of Materials Research*, 36(1):49–79, aug 2006.

[81] Umberto De Giovannini, Hannes Hübener, and Angel Rubio. A first-principles time-dependent density functional theory framework for spin and time-resolved angular-resolved photoelectron spectroscopy in periodic systems. *Journal of Chemical Theory and Computation*, 13:265–273, 2017.

[82] R. G. Greaves and J. Moxom. In T. Mitchell M. Schauer and R. Nebel, editors, *Non-Neutral Plasma Physics V*, number 692, page 140, 2003.

[83] R. G. Greaves and J. M. Moxom. Compression of trapped positrons in a single particle regime by a rotating electric field. *Physics of Plasmas*, 15:072304, 2008.

[84] R. G. Greaves and C. M. Surko. Inward transport and compression of a positron plasma by a rotating electric field. *Phys. Rev. Lett.*, 85:1883–1886, Aug 2000.

[85] A. Greenberger, A.P. Mills, A. Thompson, and S. Berko. Evidence for positronium-like bloch states in quartz single crystals. *Physics Letters A*, 32(2):72–73, jun 1970.

[86] L. Gurung, T. J. Babij, S. D. Hogan, and D. B. Cassidy. Precision microwave spectroscopy of the positronium n=2 fine structure. *Physical Review Letters*, 125(7):073002, aug 2020.

[87] Hamamtsu Photonics K.K. Electron Tube Division. *Flat Panel Type Multianode PMT Assembly, H12700 Series*, Aug 2014.

[88] E. A. Hessels, D. M. Homan, and M. J. Cavagnero. Two-state rydberg charge exchange: An efficient method for production of antihydrogen. *Phys. Rev. A*, 57(3):1668–1671, 1998.

[89] R. J. Hill. *Phys. Rev. Lett.*, 86(15):3280–3283, 2001.

[90] S. D. Hogan. Calculated photoexcitation spectra of positronium rydberg states. *Physical Review A*, 87(6):063423, jun 2013.

[91] S. D. Hogan. Calculated photoexcitation spectra of positronium rydberg states. *Phys. Rev. A*, 87:063423, 2013.

[92] J.H. Hubbell and S.M. Seltzer. Tables of x-ray mass attenuation coefficients and mass energy-absorption coefficients, 2004.

[93] N. C. Hurst, J. R. Danielson, and C. M. Surko. Magnetic field extraction of trap-based electron beams using a high-permeability grid. *Physics of Plasmas*, 22(7):073503, jul 2015.

[94] A. B. McDonald I. K. MacKenzie, T. L. Khoo and B. T. A. McKee. Temperature dependence of positron mean lives in metals. *Phys. rev. Lett*, 19(17):946, 1967.

[95] J. D. Jackson, S. B. Treiman, and H. W. Wyld. Proposed experiment to determine the direction of-meson polarization in pion decay. *Physical Review*, 107(1):327–328, jul 1957.

[96] O Jagutzki, V Mergel, K Ullmann-Pfleger, L Spielberger, U Spillmann, R Dörner, and H Schmidt-Böcking. A broad-application microchannel-plate detector system for advanced particle or photon detection tasks: large area imaging, precise multi-hit timing information and high detection rate. *Nuclear Instruments and Methods in Physics Research Section A: Accelerators, Spectrometers, Detectors and Associated Equipment*, 477(1-3):244–249, jan 2002.

[97] M. F. Joliot and I. Curie. Un nouveau type de radioactivite. *J. Phys*, 5(153):254, 1934.

[98] A C L Jones, T H Hisakado, H J Goldman, H W K Tom, and A P Mills. Polarization dependence ofn= 2 positronium transition rates to stark-splitn= 30 levels via crossed-beam spectroscopy. *Journal of Physics B: Atomic, Molecular and Optical Physics*, 49(6):064006, mar 2016.

[99] A. C. L. Jones, T. H. Hisakado, H. J. Goldman, H. W. K. Tom, A. P. Mills Jr., and D. B. Cassidy. Doppler-corrected balmer spectroscopy of rydberg positronium. *Phys. Rev. A*, 90:012503, 2014.

[100] A. C. L. Jones, A. M. Piñeiro, E. E. Roeder, H. J. Rutbeck-Goldman, H. W. K. Tom, and A. P. Mills. Large-area field-ionization detector for the study of rydberg atoms. *Review of Scientific Instruments*, 87(11):113307, nov 2016.

[101] A. C. L. Jones, H. J. Rutbeck-Goldman, T. H. Hisakado, A. M. Piñeiro, H. W. K. Tom, A. P. Mills, Jr., B. Barbiellini, and J. Kuriplach. Angle-resolved spectroscopy of positronium emission from a Cu(110) surface. *Phys. Rev. Lett.*, 117:216402, Nov 2016.

[102] A.C.L. Jones, J. Moxom, H.J. Rutbeck-Goldman, K.A. Osorno, G.G. Cecchini, M. Fuentes-Garcia, R.G. Greaves, D.J. Adams, H.W.K. Tom, A.P. Mills, and M. Leventhal. Focusing of a rydberg positronium beam with an ellipsoidal electrostatic mirror. *Physical Review Letters*, 119(5):053201, 2017.

[103] Adric C. L. Jones, Gabriel G. Cecchini, Jeremy Moxom, Kevin Osorno, Harris J. Rutbeck-Goldman, Melina Fuentes-Garcia, Rod G. Greaves, Daniel J. Adams, Harry W. K. Tom, and Allen P. Mills. A study on the performance of an electrostatic focusing mirror for rydberg positronium. *European Physical Journal D*, 72(1):1–8, 2018.

[104] Xu-Dong Ju, Ming-Yi Dong, Yi-Chen Zhao, Chuan-Xing Zhou, and Ou-Yang Qun. Design and optimization of resistive anode for a two-dimensional imaging gem detector. *Chinese Physics C*, 40(8), 2016.

[105] K Kanaya, H Kawakatsu, H Yamazaki, and S Sibata. Electron optical properties of three-electrode electron lenses. *Journal of Scientific Instruments*, 43(7):416–429, jul 1966.

[106] S. G. Karshenboim. Precision physics of simple atoms: Qed tests, nuclear structure and fundamental constants. *Phys. Rep.*, 422:1–63, 2005.

[107] Savely G Karshenboim. Precision study of positronium: Testing bound state qed theory. *International Journal of Modern Physics A*, 19(23):3879–3896, 2004.

[108] A. Kellerbauer et al. Proposed antimatter gravity measurement with an antihydrogen beam. *Nucl. Instrum. and Meth. B*, 266(3):351–356, 2008.

[109] O. Klein and Y. Nishina. Über die streuung von strahlung durch freie elektronen nach der neuen relativistischen quantendynamik von dirac. *Z. Phys.*, 52(11-12):853–868, 1929.

[110] B. A. Kniehl and A. A. Penin. Order $\alpha^7\ln(1/\alpha)$ contribution to positronium hyperfine splitting. *Phys. Rev. Lett.*, 85(24):5094–5097, 2000.

[111] Peter Krüger, Zoran Hadzibabic, and Jean Dalibard. Critical point of an interacting two-dimensional atomic Bose gas. *Phys. Rev. Lett.*, 99:040402, Jul 2007.

[112] Alexander Germanovich Krupyshev. *Diamond and silicon (100)(1 x 1)-2H surface structure determination by low-energy positron diffraction.* Brandeis University, 2000.

[113] P. Kubica and A. T. Stewart. Thermalization of positrons and positronium. *Phys. Rev. Lett.*, 34:852–855, Apr 1975.

[114] P. Kubica and A. T. Stewart. Positron motion in metals. *Canadian Journal of Physics*, 61(7):971–978, jul 1983.

[115] Willis E. Lamb and Robert C. Retherford. Fine structure of the hydrogen atom. part i. *Physical Review*, 79(4):549–572, aug 1950.

[116] M. Lampton and C. W. Carlson. Low-distortion resistive anodes for two-dimensional position-sensitive MCP systems. *Review of Scientific Instruments*, 50(9):1093–1097, sep 1979.

[117] M Lampton, O Siegmund, and R Raffanti. Delay line anodes for microchannel-plate spectrometers. *Review of Scientific Instruments*, 58(12):2298–2305, 1987.

[118] Michael Lampton and Francesco Paresce. The ranicon: A resistive anode image converter. *Review of Scientific Instruments*, 45(9):1098–1105, sep 1974.

[119] G. E. Lee-Whiting. Thermalization of positrons in metals. *Phys. Rev.*, 97:1557–1558, Mar 1955.

[120] R. Ley, K. D. Niebling, G. Werth, C. Hahn, H. Schneider, and I. Tobehn. Energy dependence of excited positronium formation at a molybdenum surface. *J. Phys. B*, 23(19):3437–3442, 1990.

[121] W. Liu, M. G. Boshier, S. Dhawan, O. van Dyck, P. Egan, X. Fei, M. Grosse Perdekamp, V. W. Hughes, M. Janousch, K. Jungmann, D. Kawall, F. G. Mariam, C. Pillai, R. Prigl, G. zu Putlitz, I. Reinhard, W. Schwarz, P. A. Thompson, and K. A. Woodle. High precision measurements of the ground state hyperfine structure interval of muonium and of the muon magnetic moment. *Phys. Rev. Lett.*, 82(4):711–714, 1999.

[122] K. G. Lynn. Observation of surface traps and vacancy trapping with slow positrons. *Phys. Rev. Lett*, 43(5):391–394, 1979.

[123] Leon Madansky and Franco Rasetti. An attempt to detect thermal energy positrons. *Phys. Rev.*, 79(2):397, 1950.

[124] JP Marler and CM Surko. Positron-impact ionization, positronium formation, and electronic excitation cross sections for diatomic molecules. *Physical Review A*, 72(6):062713, 2005.

[125] Masanori Mayusumi, Masato Imai, Shinji Nakahara, Kazutoshi Inoue, and Hitoshi Habuka. Morphology of silicon oxide film on silicon wafer surface during its removal process in a hydrogen ambient. *Japanese Journal of Applied Physics*, 40(Part 1, No. 11):6556–6560, nov 2001.

[126] K. Melnikov and A. Yelkhovsky. O($\alpha^3 \ln\alpha$) corrections to muonium and positronium hyperfine splitting. *Phys. Rev. Lett.*, 86(8):1498–1501, 2001.

[127] DONALD H. MENZEL. Oscillator strengths for high-level transitions in hydrogen. *Nature*, 218(5143):756–757, may 1968.

[128] A. P. Mills, S. Berko, and K. F. Canter. Fine-structure measurement in the first excited state of positronium. *Physical Review Letters*, 34(25):1541–1544, jun 1975.

[129] A. P. Mills and Loren Pfeiffer. Desorption of surface positrons: A source of free positronium at thermal velocities. *Physical Review Letters*, 43(26):1961–1964, dec 1979.

[130] A. P. Mills, Loren Pfeiffer, and P. M. Platzman. Positronium velocity spectroscopy of the electronic density of states at a metal surface. *Physical Review Letters*, 51(12):1085–1088, sep 1983.

[131] Allen P. Mills. Remembering martin deutsch. *Materials Science Forum*, 445-446:5–8, jan 2004.

[132] Allen P. Mills. Possible experiments with high density positronium. In *AIP Conference Proceedings*, volume 2182, page 030001. AIP Publishing, 2019.

[133] A. P. Mills, Jr. Positronium formation at surfaces. *Phys. Rev. Lett.*, 41(26):1828–1831, 1978.

[134] A. P. Mills, Jr. Brightness enhancement of slow positron beams. *Applied physics*, 23(2):189–191, Oct 1980.

[135] A. P. Mills, Jr. Time bunching of slow positrons for annihilation lifetime and pulsed laser photon absorption experiments. *Applied physics*, 22(3):273–276, Jul 1980.

[136] A. P. Mills, Jr. Line-shape effects in the measurement of the positronium hyperfine interval. *Phys. Rev. A*, 27(1):262–267, 1983.

[137] A. P. Mills, Jr. Possibilities for measuring the passive gravitational mass of electrons and positrons in free horizontal flight. *Hadronic Journal*, 19:77–86, 1996.

[138] A. P. Mills, Jr. Positronium molecule formation, Bose-Einstein condensation and stimulated annihilation. *Nuclear Instruments and Methods in Physics Research Section B: Beam Interactions with Materials and Atoms*, 192(1):107–116, 2002.

[139] A. P. Mills, Jr. and G. H. Bearman. New measurement of the positronium hyperfine interval. *Phys. Rev. Lett.*, 34(5), 1975.

[140] A. P. Mills, Jr. and M. Leventhal. Can we measure the gravitational free fall of cold rydberg state positronium? *Nucl. Instrum. and Meth. B*, 192:102–106, 2002.

[141] A. P. Mills, Jr., E. D. Shaw, R. J. Chichester, and D. M. Zuckerman. Positronium thermalization in SiO_2 powder. *Phys. Rev. B*, 40:2045–2052, Aug 1989.

[142] A Po Mills Jr and EM Gullikson. Solid neon moderator for producing slow positrons. *Applied Physics Letters*, 49(17):1121–1123, 1986.

[143] Allen P. Mills Jr. Observation of the positronium negative ion. *Physical Review Letters*, 46(11):717, 1981.

[144] Allen P. Mills, Jr. and Robert J. Wilson. Transmission of 1 - 6-kev positrons through thin metal films. *Phys. Rev. A*, 26:490–500, Jul 1982.

[145] Stjepan Mohorovicic. Möglichkeit neuer elemente und ihre bedeutung für die astrophysik. *Astronomische Nachrichten*, 253:93, 1934.

[146] Jorge J Moré and Danny C Sorensen. Computing a trust region step. *SIAM Journal on Scientific and Statistical Computing*, 4(3):553–572, 1983.

[147] T. J. Murphy and C. M. Surko. Positron trapping in an electrostatic well by inelastic collisions with nitrogen molecules. *Physical Review A*, 46(9):5696–5705, nov 1992.

[148] Krzysztof Pachucki and Savely G. Karshenboim. Complete results for positronium energy levels at orderm6. *Physical Review Letters*, 80(10):2101–2104, mar 1998.

[149] Van Der Pauw. A method of measuring specific resistivity and hall effect of discs of arbitrary shape. *Philips Research reports*, 13(1):1–9, 1958.

[150] Catherine Michelle Pepin, Philippe Bérard, A-L Perrot, Claude Pépin, Daniel Houde, Roger Lecomte, Charles L Melcher, and Henri Dautet. Properties of lyso and recent lso scintillators for phoswich pet detectors. *IEEE Transactions on Nuclear Science*, 51(3):789–795, 2004.

[151] A. Perkins and J. P. Carbotte. Effect of the positron-phonon interaction on positron motion. *Phys. Rev. B*, 1:101–107, Jan 1970.

[152] P. M. Platzman and A. P. Mills, Jr. Possibilities for Bose condensation of positronium. *Phys. Rev. B*, 49:454–458, Jan 1994.

[153] CA Rezende, RF Gouveia, MA Da Silva, and F Galembeck. Detection of charge distributions in insulator surfaces. *Journal of Physics: Condensed Matter*, 21(26):263002, 2009.

[154] A. Rich and H. R. Crane. Direct measurement of the g factor of the free positron. *Physical Review Letters*, 17(5):271, 1966.

[155] M. W. Ritter, P. O. Egan, V. W. Hughes, and K. A. Woodle. *Phys. Rev. A*, 30(3):1331–1338, 1984.

[156] Saint-Gobain Ceramics and Plastics Inc. *Scintillation Materials and Assemblies*, 2014.

[157] D. C. Schoepf, S. Berko, K. F. Canter, and P. Sferlazzo. Observation of ps($n = 2$) from well-characterized metal surfaces in ultrahigh vacuum. *Phys. Rev. A*, 45(3):1407–1411, 1992.

[158] P. J. Schultz, E. M. Gullikson, and A. P. Mills, Jr. Transmitted positron reemission from a thin single-crystal Ni(100) foil. *Phys. Rev. B*, 34:442–444, Jul 1986.

[159] P. J. Schultz and K. G. Lynn. Interaction of positron beams with surfaces, thin films, and interfaces. *Rev. Mod. Phys.*, 60:701–779, Jul 1988.

[160] PB Schwinberg, RS Van Dyck Jr, and HG Dehmelt. Trapping and thermalization of positrons for geonium spectroscopy. *Physical Letters A*, 81(2):119–120, 1981.

[161] A. Speck, C. H. Storry, E. A. Hessels, and G. Gabrielse. Laser-controlled production of rydberg positronium via charge exchange collision. *Phys. Lett. B*, 597:257–262, 2004.

[162] T. D. Steiger and R. S. Conti. Formation of $n = 2$ positronium from untreated metal surfaces. *Phys. Rev. A*, 45(5):2744–2752, 1992.

[163] A. T. Stewart. Angular correlation of photons from positron annihilation in solids. *Phys. Rev.*, 99(2):594, July 1955.

[164] A. T. Stewart. Momentum distribution of metallic electrons by positron annihilation. *Can. J. Phys.*, 35(2):168–183, 1957.

[165] A. T. Stewart, C. V. Briscoe, and J. J. Steinbacher. Positron annihilation in simple condensed gases. *Canadian Journal of Physics*, 68(12):1362–1376, 1990.

[166] W. Stoeffl, P. Asoka-Kumar, and R. Howell. The positron microprobe at LLNL. *Appl. Surf. Sci.*, 149(1):1–6, 1999.

[167] C. H. Storry, A. Speck, D. Le Sage, N. Guise, G. Gabrielse, D. Grzonka, W. Oelert, G. Schepers, T. Sefzick, H. Pittner, M. Herrmann, J. Walz, T. W. H änsch, D. Comeau, and E. A. Hessels. First laser-controlled antihydrogen production. *Phys. Rev. Lett.*, 93(26):263401, 2004.

[168] C. M. Surko and R. G. Greaves. Emerging science and technology of antimatter plasmas and trap-based beams. *Phys. Plas.*, 11(5):2333–2348, 2004.

[169] C. M. Surko, M. Leventhal, WS Crane, and A. P. Mills, Jr. The positron trap-a new tool for plasma physics. In W. S. Crane A. P. Mills and K. F. Canter, editors, *Positron Studies of Solids, Surfaces, and Atoms; a Symposium to Celebrate Stephan Berko's 60th Birthday*, pages 222–223. World Scientific, 1986.

[170] C. B. Tarter. Coefficients connecting the Stark and field-free wavefunctions for hydrogen. *J. Math. Phys.*, 11(11):3192–3195, 1970.

[171] Xavier Urbain, D Bech, J-P Van Roy, M Géléoc, Sébastien J Weber, A Huetz, and YJ Picard. A zero dead-time multi-particle time and position sensitive detector based on correlation between brightness and amplitude. *Review of Scientific Instruments*, 86(2):023305, 2015.

[172] R. S. Vallery, P. W. Zitzewitz, and D. W. Gidley. Resolution of the orthopositronium-lifetime puzzle. *Physical Review Letters*, 90(20):203402, may 2003.

[173] Carel WE Van Eijk. Inorganic scintillators in positron emission tomography. In *Radiation Detectors for Medical Applications*, pages 259–274. Springer, 2006.

[174] A Vehanen, KG Lynn, Peter J Schultz, and M Eldrup. Improved slow-positron yield using a single crystal tungsten moderator. *Applied Physics A*, 32(3):163–167, 1983.

[175] M. Villata. Cpt symmetry and antimatter gravity in general relativity. *Eur. Phys. Lett.*, 94:20001, 2011.

[176] E. Vliegen and F. Merkt. Normal-incidence electrostatic rydberg atom mirror. *Phys. Rev. Lett.*, 97(3):033002, July 2006.

[177] T. E. Wall, A. M. Alonso, B. S. Cooper, A. Deller, S. D. Hogan, and D. B. Cassidy. Selective production of rydberg-stark states of positronium. *Physical Review Letters*, 114(17):173001, apr 2015.

[178] Howard Weisberg and Stephan Berko. Positron lifetimes in metals. *Phys. Rev.*, 154(2):249–257, 1967.

[179] John Wheatley and David Halliday. The quenching of ortho-positronium decay by a magnetic field. *Phys. Rev.*, 88:424–424, Oct 1952.

[180] John Archibald Wheeler. Polyelectrons. *Annals of the New York Academy of Sciences*, 48(1):219–238, 1946.

[181] William H. Wing. Electrostatic trapping of neutral atomic particles. *Phys. Rev. Lett.*, 45(8):631–634, August 1980.

[182] Don M. Yost, L. N. Ridenour, and K. Shinohara. Chemical identification of the radioelements produced from carbon and boron by deuteron bombardment. *The Journal of Chemical Physics*, 3(3):133–136, mar 1935.

[183] Jacek Zatorski. O(m6)corrections to energy levels of positronium with nonvanishing orbital angular momentum. *Physical Review A*, 78(3):032103, sep 2008.

[184] K. P. Ziock, R. H. Howell, F. Magnotta, R. A. Failor, and K. M. Jones. First observation of resonant excitation of high-n states of positronium. *Phys. Rev. Lett.*, 64(20):2366–2369, 1990.